Progress in Materials Science 131 (2023) 101019

Contents lists available at ScienceDirect

Progress in Materials Science

journal homepage: www.elsevier.com/locate/pmatsci

Heterostructured materials

Yuntian Zhu [a,*], Xiaolei Wu [b,*]

[a] Department of Materials Science and Engineering, City University of Hong Kong, Hong Kong, China
[b] State Key Laboratory of Nonlinear Mechanics, Institute of Mechanics, Chinese Academy of Sciences, Beijing, China

ABSTRACT

Heterostructured (HS) materials are a new class of materials that are composed of heterogeneous zones with dramatically different (>100 %) mechanical or physical properties. The interactive coupling between these heterogeneous zones produces a synergistic effect in which the integrated property exceeds the prediction by the rule-of-mixtures. HS materials possess superior mechanical or physical properties that are not achievable by their conventional homogenous counterparts. This review focuses primarily on structural HS materials, whose superior mechanical properties are enabled by a new scientific principle: hetero-deformation induced (HDI) strengthening and HDI work hardening. Geometrically necessary dislocations (GNDs) in the soft zones pile up and accumulate near the zone boundaries, producing back stress in the soft zones and forward stress in the hard zones, which collectively produces the HDI stress. HS materials have a unique deformation behavior: formation of dispersive microscopic strain bands, which helps to distribute plastic strain over the whole gauge length, increasing uniform elongation. They can be readily produced using conventional industrial technologies and facilities at large scale and low cost. The superior properties, new materials science and great application potentials are driving the fast development of the HS materials field. This review is meant to introduce students and researchers to this emerging field, and to serve as an authoritative reference on HS materials.

1. Introduction

Heterostructured (HS) materials exist ubiquitously in the nature and have been used in many types of man-made structures and components, although HS materials as a category of materials was not well defined or systematically studied by scientists until recently [1]. HS materials exhibit superior functional and mechanical properties over homogeneous materials, which is why they have been selected by natural evolution and often explored by mankind. In this review paper we will focus largely on the mechanical properties of structural HS materials, although some functional properties will also be briefly discussed.

HS materials are quickly emerging as a major research field because of their superior properties and great application potentials. For example, heterogeneous lamellae Ti has been reported to have the high strength of nanostructured Ti and the good ductility of coarse-grained Ti, a property combination that is impossible according to our conventional textbook and literature knowledge [2]. More importantly, such a heterostructure can be fabricated using current industrial facilities at low costs, which makes their commercialization much easier than other advanced materials.

It appears that our conventional understanding of materials science is often not sufficient to explain the mechanical behaviour of HS materials, and there are many scientific issues that need to be solved before we can design HS materials for superior properties. For example, the heterostructured Ti was processed by cold deformation followed by partial-recrystallization annealing. The cold

---

Abbreviations: HS, Heterostructured; GND, geometrically necessary dislocation; HDI, Hetero-deformation induced; HBAR, hetero boundary affected region; UFG, ultrafine grained; CG, coarse grained.

[*] Corresponding authors at: Department of Materials Science and Engineering, City University of Hong Kong, Hong Kong, China (Y. Zhu). State Key Laboratory of Nonlinear Mechanics, Institute of Mechanics, Chinese Academy of Sciences, Beijing, China (X. Wu).

E-mail addresses: y.zhu@cityu.edu.hk (Y. Zhu), xlwu@imech.ac.cn (X. Wu).

https://doi.org/10.1016/j.pmatsci.2022.101019
Received 2 April 2022; Received in revised form 20 May 2022; Accepted 4 September 2022

deformation produced a nanostructure with high strength but low ductility. The annealing reduced the overall dislocation density and produced some large micrometer-sized grains, both of which should have decreased the strength according to our conventional teaching. However, the heterostructured Ti maintained the high strength after annealing, defying the conventional materials science.

It will take collaborative efforts of researchers from the communities including materials science, mechanics and computational modelling to solve some of the fundamental issues of HS materials. In other words, the field of HS materials represents a new frontier for scientists to explore with very promising potential for real world applications. This is why it has quickly attracted many renowned research groups worldwide to join this research field.

The objective of this review paper is to introduce HS materials to the materials research community, particularly the definition of heterostructured structural materials, their fundamental principle, processing technologies, microstructures, properties and potential applications. The targeted readers of this paper are graduate students who are working in this area, researchers who are entering this emerging research field, as well as scientists and engineers who are already working on heterostructured materials.

In this section, we will discuss the historical perspective, scope and definition of heterostructured materials.

1.1. Natural heterostructures

Heterostructured (HS) materials exist in most botanical and biological systems [3–5]. These HS materials have been evolved for millions of years through natural evolution. For a natural system such as plants to survive the severe natural environment such as wind and storms, they need to be strong and resilient while minimizing the material cost [6]. One example is the stems of bamboos, which are so strong, tough and lightweight that they are still being used for scaffolding for constructing and renovating tall buildings in Hong Kong (see Fig. 1) and South East Asia [7]. Fig. 2 reveals the heterostructure in the cross-section of a bamboo, which shows strong fibrils embedded in a softer matrix. In addition, the distribution of the fibrils is not uniform in the cross-section, with gradient distribution of higher number-density toward the outer surface. Such a distribution helps with enhancing the bending strength of the bamboo, which makes them strong and tough during storms.

Another class of examples of natural heterostructures is molluscs shells (Fig. 3a), which has evolved for over 545 million years [8]. Shown in Fig. 3b is an abalone shell, which is a species of molluscs [8]. Fig. 3c is the SEM image of the cross-section of an abalone shell [8] As shown, the shell consists of an outer layer of hard calcite ($CaCO_3$) crystals and an inner layer of tough nacre. The outer layer is hard but brittle, which is supported by the tough nacre layer to maintain the integrity of shell in the event of external impact. This is the same principle used in body armor [8]. The nacre layer has a brick and mortar structure, with each brick as polygonal tablets of 5–8 μm in diameter and ~ 0.5 μm in thickness, as shown in Fig. 3d [9] and Fig. 3e. These tablets are bound together by organic layers of 20–30 nm in thickness [8]. As shown in Fig. 3f, each tablet consists of the aragonite ($CaCO_3$) nanocrystallite embedded in continuous organic matrix. Therefore, the nacre structure is often also called a hierarchical structure [8,9].

Fig. 1. Strong, tough and lightweight bamboos are used for scaffolding in building renovation on the campus of City University of Hong Kong.

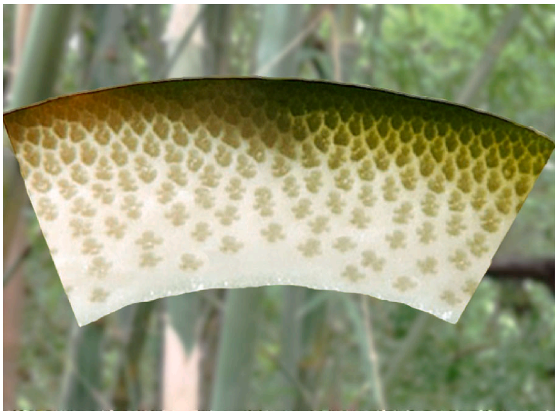

Fig. 2. Heterostructured bamboo with gradient distribution of strong fibrils in the cross-section.

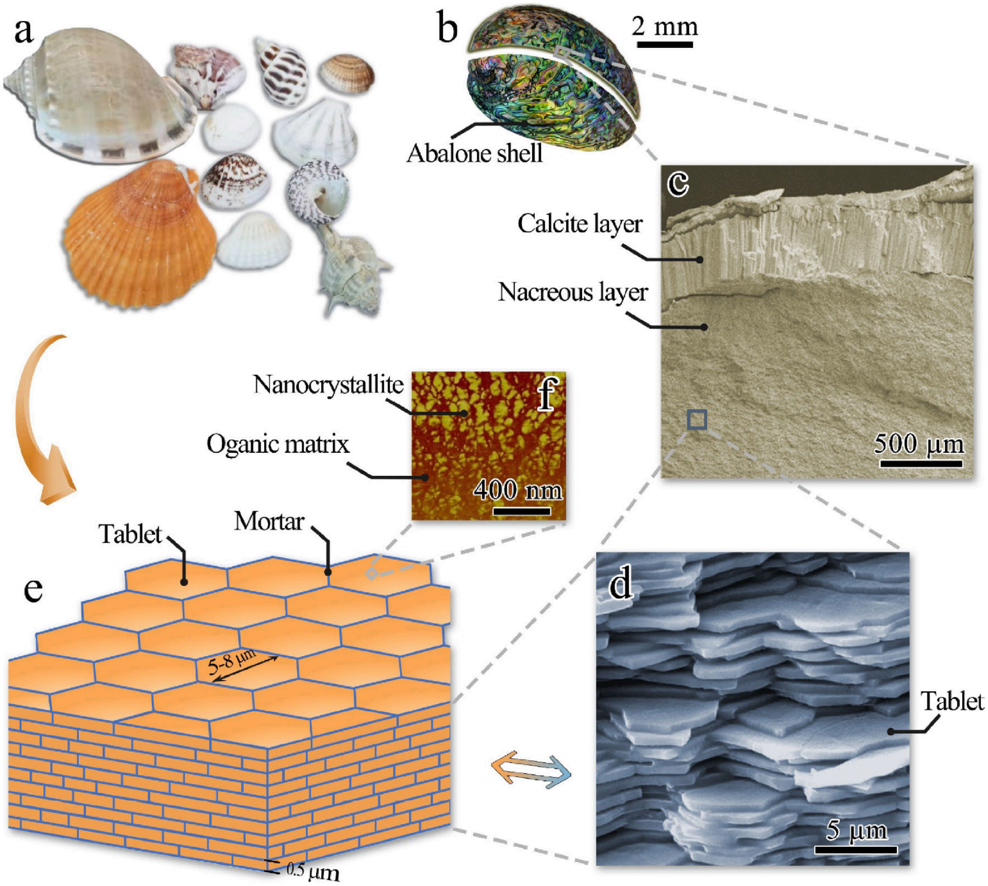

Fig. 3. The structure of Molluscs shell. (a) Molluscs shells. (b) An abalone shell. (c) The cross-section of an abalone shell showing hard outer calcite layer and nacre inside layer [8]. (d) The fracture surface of an abalone nacre showing pulled-out tablets [9]. (e) Schematics of the brick-and-mortar structure of the nacre layer with tablets bound together by an organic phase. (f) The tablets composing of aragonite ($CaCO_3$) nanocrystals embedded in an organic matrix.

The heterostructure of nacre consists of an optimal assembly of hard, brittle zones (tablets) and soft, ductile zones, which makes it strong and tough [8–12]. Calcite and aragonite tablets in the nacre are brittle $CaCO_3$ phases, and they provide the stiffness [8]. The organic phase has very high toughness but very low stiffness [8]. The stiffness and toughness of engineering materials usually follows a banana curve, i.e. high stiffness is accompanied with low toughness, and vice versa. However, the heterostructured (hierarchical) nacre defies the banana curve by showing both high stiffness and high toughness [8]. It was reported that the high toughness of the nacre comes from three effects [10]: inter-tablet friction due to asperities, organic binder between the tablets and the fracture of the tablets.

These are only two examples of natural heterostructures. In fact, heterostructures can be found in almost all living natural systems, including bones, tree trunks, etc [8].

1.2. History of man-made heterostructured materials

Heterostructured (HS) materials have been used by mankind since prehistoric times as construction materials. For example, straw and mud building, named cob in English term, can be considered made of HS materials consisting of two different material components (https://en.wikipedia.org/wiki/Cob_(material)). Shown in Fig. 4 is an example of straw and mud walls. The mixture of straw with the mud (clay-based subsoil) makes the wall much stronger and tougher because the straws can bridge cracks and hold the dried mud matrix together. Such types of houses can still be found in Africa, the Middle East, China, and southwestern United States (also called adobe in this region). Modern buildings and structures are also mostly made of HS materials, which consist of different constituent materials such as cement, gravel and steel re-bars.

For engineering materials such as metals, mankind learned to make heterostructures with high density of interfaces to produce strong and tough tools and weapons almost two thousand years ago [13,14]. For example, by repeated forging and folding, blacksmiths in China made Beilian steel swords that are both strong and tough in the 2nd century [14]. The word "Beilian" literally means forging and folding for 100 times. A new internal folding interface is formed every time the steel piece is folded, which also reduces the spacings of interfaces between different phases in the steel workpiece. The repetitive folding eventually produces a heterostructure with high density of interfaces, including phase interfaces and folding interfaces, which makes the sword strong and tough. Later examples include Damasco steel, Sumara sward, Viking axes, etc. These materials and tools are mostly made by skilled blacksmiths with techniques refined for generations by trial and error. There is no fundamental understanding on the origin of the superior properties.

1.3. Definition of heterostructured materials

In a broad sense, materials with non-uniform microstructures can be literally regarded as heterostructured (HS) materials, including composite materials, steels and alloys with second-phase particles and multiple phases, construction materials for buildings and bridges, etc. These materials are very diverse and span many academic fields. Many of these materials have been studied and used for decades and have been regarded as conventional materials. As discussed below, here we will focus on heterostructured materials that develop significant hetero-deformation induced (HDI) stress during deformation. This effectively limits the scope of HS materials to metallic systems in which dislocation slip and twinning are the primary deformation mechanisms.

Heterostructured (HS) materials are defined as materials consisting of heterogeneous zones with a dramatic (>100 %) difference in mechanical and/or physical properties. The interactions between these hetero-zones produce a synergistic effect where the integrated property exceeds the prediction by the rule-of-mixtures [15,16]. For structural heterostructured materials, the large difference in flow stress leads to high heterogeneous (non-uniform) deformation, which produces hetero-deformation induced (HDI) strengthening and strain hardening. The HDI strengthening leads to improvement in yield strength, while the HDI strain hardening helps to retain and even improve ductility [17,18]. The HDI strengthening can be quantified as the HDI stress at yielding, and the HDI strain hardening can be quantified as HDI stress increase rate with applied strain. These two stresses can be measured using a loading–unloading-reloading procedure [19]. The dislocation hardening is originated from dislocation hardening as described by the Taylor equation [20–22],

$$\sigma = \alpha M G b \sqrt{\rho} \tag{1}$$

Fig. 4. Dried straw and mud wall for building houses since prehistoric times.

where $\rho = \rho_s + \rho_G$ is the total dislocation density, ρ_s is the density of statistically stored dislocations, ρ_G is the density of geometrically necessary dislocations (GNDs), α is a constant, M is the Taylor factor, G is the shear modulus, b is the magnitude of Burgers vector.

Materials that satisfy the above definition of HS materials include, but are not limited to, 1) heterogeneous lamella structured (HLS) materials [2], gradient structured (GS) materials [6,23–26], layer-structured (LS) materials [13,27–32], harmonic structured (core–shell) materials [33–37], dual-phase alloys [38–44], metal matrix composites [45–48], bi-modal structured [49–51], multi-modal or hierarchical structured materials [52,53], etc. The microstructures of these materials appear very diverse, but they share a common thread in the physics of their superior mechanical properties. Some of these materials have been studied for years or decades, but have not been classified as HS materials in previous literature. However, they share the same physical mechanisms for their superior mechanical properties, i.e. HDI strengthening and hardening.

2. Mechanical behavior of coarse-grained metals

Most engineering metals and alloys in current industrial applications are coarse-grained, and their mechanical behaviors and properties have been extensively studied for over a century. Typical mechanical behaviors of coarse-grained metals can be readily found in college textbooks [22,54,55]. Here we will only briefly discuss some basic aspects that are to be used later in the discussion of the mechanical behaviors of heterostructured (HS) materials.

2.1. Tensile stress–strain curves

Shown in Fig. 5a is a schematic of typical engineering stress–strain curve of metals and alloys. As shown, with increasing applied tensile strain, the sample initially deforms linearly (elastically), and the slop of the linear section is called the Young's modulus. Plastic deformation sets in at the elastic limit. However, the transition from elastic to plastic deformation is often gradual, making it hard to determine the exact yield point, after which the sample is considered deforming plastically. To make it easy, a 0.2 % plastic strain is used to determine the yield point, as shown in Fig. 5a, which seems arbitrary, but has been accepted as a standard. The yield strength determined at 0.2 % plastic strain, $\sigma_{0.2}$, is a material property that is used for designing machine parts and structures.

Another strength value measured from the tensile testing is the ultimate strength, σ_{UTS}, which is the maximum engineering stress (see Fig. 5a). The ultimate strength is also called tensile strength in some papers and books. It should be noted that by definition the ultimate strength and tensile strength can only be measured from the engineering stress–strain curve. Gross overestimation may be resulted if they are mistakenly determined from the true stress–strain curve, especially for ductile metals, because $\sigma_T = \sigma_e(\varepsilon_e + 1)$, where σ_T is the true stress, σ_e is the engineering stress and ε_e is the engineering strain.

One of the most important material properties that can be measured from the tensile engineering stress–strain curve is ductility, which is usually measured as the elongation to failure, δ_f, when standard large samples are used. Note that ductility is a safety factor for structural applications, without which metallic materials cannot be used for most structural applications. Another parameter that is used to measure ductility is the uniform elongation, which is the applied strain at the maximum engineering stress [56] (Fig. 5a).

Fig. 5b is the true stress–strain curve, which is converted from the engineering stress–strain curve. The uniform elongation, δ_u, can be also determined from the true stress–strain curve (Fig. 5b). According to the Considère criterion [57], necking instability will occur when the strain hardening rate drops to the value of flow stress, i.e.

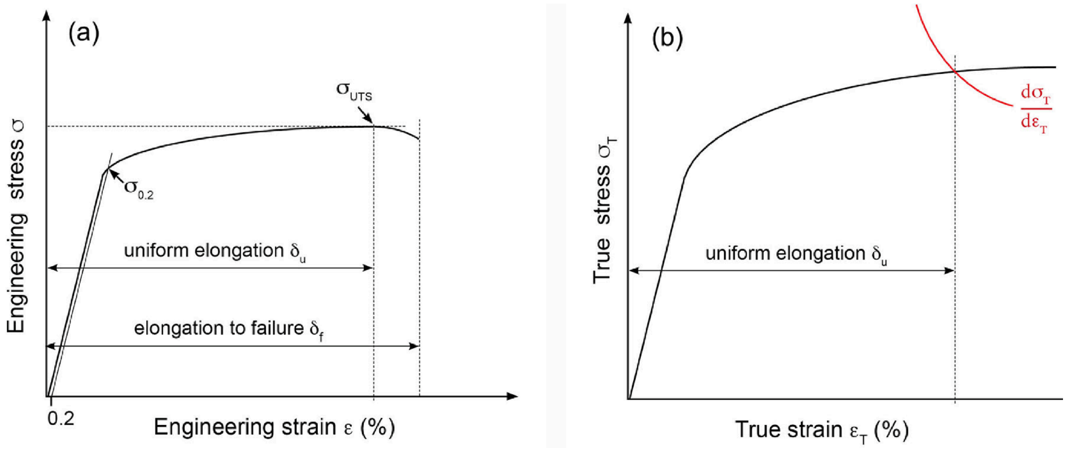

Fig. 5. Typical tensile stress–strain curves of metals and alloys. (a) Engineering stress–strain curve and the definitions of yield strength, ultimate strength (tensile strength), uniform elongation, elongation to failure. (b) True stress–strain curve calculated from the measured engineering stress–strain curve using the equations $\varepsilon_T = \ln(\varepsilon_e + 1)$ and $\sigma_T = \sigma_e(\varepsilon_e + 1)$. The true stress–strain curve is not accurate after necking. The strengths and ductility should be determined on the engineering stress–strain curve.

$$\frac{d\sigma_T}{d\varepsilon_T} = \sigma_T \tag{2}$$

where σ_T and ε_T are the true stress and true strain, respectively. As shown in Fig. 5b, the true uniform elongation strain $\delta_{T,u}$ can be determined by the intersection point of the σ_T - ε_T curve and the $d\sigma_T/\mathrm{d}\ \varepsilon_T$ - ε_T curve. The value of $\delta_{T,u}$ determined from the true stress–strain curve underestimates the uniform elongation. The correct uniform elongation value is a parameter that should be determine from the engineering stress–strain curve, and can be calculate from $\delta_{T,u}$ as.

$$\delta_u = e^{\delta_{T,u}} - 1 \tag{3}$$

It is obvious that the procedure to determine the uniform elongation from the true stress–strain curve is curbsome and complex. It is much simpler to determine the uniform elongation from the tensile engineering stress–strain curve.

When standard large tensile samples are used, the values of elongation to failure δ_f and the uniform elongation δ_u are very close, as shown in Fig. 5a. However, as discussed later, the measured δ_f value can be significantly affected by the dimensions of the gauge section of the tensile sample, especially when the gauge length is very small [56], while the measured δ_u is relatively stable and affected much less by the gage length. Therefore, for tensile testing with very small gage length, the uniform elongation, δ_u, is a better indicator of material ductility. It should be mentioned that if the gage length is extremely small, e.g. <5 mm, even the δ_u may be significantly affected if the stress state in the gage length becomes two dimensional or three dimensional [56,58,59].

It should be also noted that ductility is by definition measured by tensile testing, not any other types of testing. Ductility can also be regarded as the tensile plasticity. The difference between ductility and plasticity will be discussed later. In the literature, the term “tensile ductility” is some times used, which is problematic, because it hints at the existence of other types of ductility. One can use either “ductility” or “tensile plasticity”, but not “tensile ductility”.

2.2. *Strengthening mechanisms*

Making materials stronger has been one of the primary endeavours of materials scientists and engineers. Common strategies in the textbooks and literature include solid solution hardening, dislocation hardening, grain boundary strengthening, precipitation hardening, dispersion hardening, metal-matrix composite strengthening, etc. [54].

Solid solution strengthening comes from the interactions between alloy elements and the dislocations [54]. Alloy elements have a misfit strain field with dislocations. If the strain field of an alloy element is symmetric, e.g., in the case of substitutional solid solution, hydrostatic stress field will develop due to the size difference between the solute and solvent atoms. This hydrostatic stress field of solute atoms will interact with the hydrostatic stress field of edge dislocations, making it harder for edge dislocations to move, which produces solute hardening. Another example of hydrostatic stress field is interstitial carbon (C) atoms in the octahedral sites of face-centered cubic (fcc) iron (Fe). Since the octahedral sites are symmetric, the stress field generated by the C atoms are also symmetric. However, when C atoms are in the octahedral sites of body-centered cubic (bcc) Fe, the stress field is non-symmetrical, since it has larger distortion in the $\langle 1\,0\,0\rangle$ directions. This makes the C atoms interact with both edge and screw dislocations, which produces much stronger solution hardening. This effect is extensively used by the steel industry.

Dislocation hardening comes from the interactions of dislocations gliding on intersecting slip planes. When dislocations interact with each other and get entangled, it makes it more difficult for them to move, which produces strengthening. The flow stress of a metal can be described by the Taylor hardening equation (Eq. (1)). The dislocation hardening is also often called work hardening, because this phenomenon often occurs in cold-worked metals. During cold deformation such as cold rolling, forging and drawing, the strength of the metal increases, i.e., work hardens, so that it is often needed to carry out intermediate annealing to reduce dislocation density before it can be further cold deformed.

Grain boundary strengthening is caused by grain boundary blocking gliding dislocations. It is demonstrated by the grain size effect on strength, which is described by the Hall-Petch relationship [54,57,60]:

$$\sigma_{0.2} = \sigma_0 + \kappa d^{-1/2} \tag{4}$$

where σ_0 is a constant, κ is the Hall-Petch slope, d is the average grain size. This equation shows that strength becomes higher with decreasing grain size because of higher density of grain boundaries. It should be noted that when the grain size is below 100 nm, the Hall-Petch relationship may not be followed because of the change of deformation mechanism [57,61–65]. It should be also noted that twin boundaries can be treated as special grain boundaries and acts like grain boundaries in blocking dislocations [66]. One of the applications of this mechanism is the development of nanostructured metals and alloys, which has attracted extensive effort internationally in the last three decades [57,61,67,68].

Precipitation hardening and dispersion hardening come from the interaction of second-phase particles with moving dislocations. Their effect is largely determined by the interparticle spacing. The applied shear stress that is needed for a dislocation to loop around and pass two particles can be described as.

$$\tau = \frac{Gb}{l} \tag{5}$$

where G is the shear modulus, b is the magnitude of Burgers vector, and l is the inter-particle distance. Note that this is the same as the stress needed to operate a Frank-Read dislocation source.

The precipitates are formed from the oversaturated solid solution. Some of the precipitates can be coherent or semi-coherent with the matrix [69]. For coherent precipitates, it is also possible for the dislocations to cut through the precipitates. Readers are referred to some textbooks for more details [54,69]. The particles for dispersion hardening are usually added to the matrix by mechanical alloying. Examples are oxide-dispersion-strengthened (ODS) steels [54,70,71].

Metal-matrix composite strengthening comes from the reinforcement of such as fibers and whiskers [54,72]. The reinforcements are the stronger component that carries higher stress and there is a load transfer from the matrix to the reinforcement. This is beyond the scope of this paper and readers are referred to ref. [72] for more information. Note that the particle reinforced metal matrix composites can be treated the same way as the dispersion hardened materials, and dispersion hardening is the strengthening mechanism.

2.3. *Strain hardening*

As discussed earlier, strain hardening is critical for retaining the ductility of metals and alloys, especially those with high strength. Strain hardening literally means that as a metal is strained, it becomes stronger. In other words, as a metal is deformed, it makes it more difficult for dislocations to move to accommodate the applied strain. The strain hardening can be produced by the increase in crystalline defects such as dislocations, twins, stacking faults, grain boundaries, etc. In cases with limited plastic strain, such as tensile testing, the increase in dislocation density plays a dominant role in stain hardening, as expressed by the Taylor’s equation (Eq. (1)). The strain hardening can be derived from the Eq. (1) as.

$$\frac{d\sigma}{d\varepsilon} = \alpha MGb\frac{d\sqrt{\rho}}{d\varepsilon} \tag{6}$$

Eq. (6) indicates that the strain hardening rate is dependent on the accumulation of dislocations during the plastic deformation. It should be noted that the strain hardening depends in the dislocation density increase with increasing strain instead of the dislocation density itself. In other words, high dislocation density does not produce high strain hardening rate to help with ductility. In fact, as discussed below, initial high dislocation density before tensile testing is actually detrimental to strain hardening potential during the testing, and is thus not desired.

2.4. *Ductility and plasticity*

There is a significant confusion about the concepts of ductility and plasticity, even among many senior researchers, which have resulted in many problematic publications [56]. We need to clarify these concepts here because they will be used in the following sections.

Plasticity is the capability of a metal to deform plastically. It is the capability of a metal to activate dislocation slip systems to accommodate the externally exerted plastic strain. According to the von Mises condition [73], for the plastic deformation of polycrystalline metals, five independent slip systems are needed to operate. An independent system produces a deformation that cannot be produced by the combination of other systems. Metals with fcc and bcc crystal structures have more than five independent slip systems and therefore generally have high plasticity. However, hcp metals do not have five independent slip systems, which is why deformation twinning is usually activated during their deformation to accommodate the applied strain. However, twinning is usually more difficult to be activated than dislocation slip and it can only provide limited strain. Therefore, hcp metals usually have low plasticity. In other words, the plasticity of a metal is intrinsically controlled by its crystal structure. Of course, extrinsic factors such as microstructure, deformation temperature, deformation strain and deformation mode also affect the plasticity.

A material that has no plasticity is brittle. The brittleness of a material is measured by its plasticity. A brittle material cannot activate dislocation slip or other plastic deformation mechanisms, and therefore cannot be plastically deformed under any deformation mode. Example of brittle materials include ceramics and glasses, which will shatter under any common deformation mode because they cannot sustain any plastic deformation.

High plasticity is a critical requirement for shaping and forming metals and alloys to make metal products. Common deformation modes used in the industry include rolling, extrusion, bending, drawing, forging, and machining. Without good plasticity, industrial processing of metals and alloys using these common deformation modes will be difficult or even impossible. It should be noted that the deformation mode may significantly affect the plasticity. Metals with high plasticity under one deformation mode may not exhibit high plasticity under another deformation mode. For example, nanostructured metals often have high plasticity under compression and rolling, but low plasticity under drawing and tensile testing.

Ductility is the capability of a metal to deform under tension, and therefore can be also regarded as plasticity under the tensile mode, i.e. tensile plasticity [56]. A metal with low plasticity certainly will have low ductility. However, high plasticity does not guarantee high ductility. For example, nanostructured metals and alloys typically have high plasticity but low ductility.

As discussed earlier, if a metal has high plasticity, the ductility is determined by the strain hardening rate under tensile test. To obtain high ductility, the strain harden rate needs to be high enough to prevent localized deformation (necking) (see Eq. (2)). Necking is the beginning of sample failure during tensile testing. Therefore, to improve the ductility of a metal or alloy, one should find ways to improve the strain hardening rate during tensile testing.

Eq. (6) demonstrates that the key to improve strain hardening rate is to increase the rate for dislocation accumulation. Gliding dislocations can be stopped and forced to accumulate at barriers such as grain boundaries, twin boundaries, and phase boundaries [57,62,74]. Some dislocation barriers are more effective than others in accumulating dislocations. This means that we can engineer microstructures to improve the strain hardening rate and consequently enhance the ductility.

It needs to be stressed that it is the dislocation density increase, not the total dislocation density, that matters in improving the ductility. This is the reason why cold-worked metals often have low ductility although they have high dislocation density. Cold worked metals have high strength due to their high dislocation density. There exists a saturation dislocation density beyond which the dislocations can no longer accumulate. Therefore, the high dislocation density of cold-worked metal leaves little room for further dislocation accumulation during tensile testing, which leads to low strain hardening rate and low ductility. To solve this problem, the work-worked metals can be annealed to lower the dislocation density, but this often sacrifices the strength. Other strengthening mechanisms discussed in Section 2.2 either decrease the strain hardening capability or do not increase strain hardening enough to maintain the same ductility as the strength increases, leading to the strength-ductility trade-off, i.e. the so-called banana curve [1,75]. Compared with materials with low flow stress, high strength materials need higher strain hardening rate to maintain the same ductility according to the Considère criterion [57] (Eq. (2)).

Good ductility is a safety requirement for structural components. Metals and alloys with high strength but low ductility (5 %) are usually not acceptable for most structural applications under tensile load. In other words, reasonable ductility is required for a metal product to be safe, and therefore is often a required property during the design of metal components and structures.

3. Mechanical behavior of nanostructured metals

Making materials stronger is an enduring endeavour for materials scientists and engineers, especially under the current situation of energy crisis and global warming. Strong materials are desired to make energy efficient transportation vehicles such as electric cars, trucks and airplanes. As discussed in the last section, one of the major strengthening mechanisms are grain refinement. Basing on this principle, Gleiter proposed and reported that nanocrystalline metals will be many times stronger than conventional coarse-grained metals [67,76–78]. Gleiter's concept of nanocrystalline materials has inspired worldwide research on nanostructured metals and alloys for the past four decades [57,61,62,65,79–97]. Significant progresses have been made in the processing, microstructure and properties of nanomaterials as well as their deformation physics [57,61,62,79–81,83,98–100]. However, there are still some challenges in producing balanced and superior mechanical properties and in producing nanomaterials in large-scale production at low costs for wide industrial applications.

In this section, we focus on the strength and ductility issues of nanostructured metals and alloys, which will be compared with those of heterostructured materials later. The definitions of nanocrystalline and nanostructured materials are not completely consistent in the materials community. The most accepted definition for nanocrystalline materials is materials with average grain sizes below 100 nm; the most accepted definition of nanostructured materials are materials with structural features below 100 nm. Therefore, nanostructured materials cover a wider grain size range, and can have grains>100 nm as long as their sub-grain sizes or dislocation cell sizes are below 100 nm [57,62,81,100]. Another term that has been extensively used is ultrafine grained (UFG) materials, which are defined as materials with grain sizes below 1000 nm [81]. Therefore, it covers the grain size ranges of both nanocrystalline and nanostructured materials.

3.1. *Strength and ductility*

Both strength and ductility are required for structural applications. A strong material without sufficient ductility cannot be used in structures where tensile load is involved, because ductility is a safety factor to prevent catastrophic failure. However, strength and ductility are a property couple that often go against each other. They are both dependent on the microstructure, which gives materials scientist a play field to design microstructures for desired strength and ductility.

3.1.1. *Effect of processing methods*

The mechanical properties of nanostructured metals and alloys are significantly affected by processing/synthesis methods, because some processing methods inevitably introduce flaws and contaminations, especially those two-step methods involving the synthesis and consolidation of nano-powders. In early years of nanomaterials research, nanocrystalline metals were typically made using the inert gas condensation (IGC) method [101–108]. In this method, metals are evaporated by heating and then condensed on a cold finger cooled by liquid nitrogen to form nano-particles, which were scraped off and then compacted into bulk nanocrystalline samples. Extensive study on mechanical properties of such samples were performed by Weertman's group. It was found to nanocrystalline metals generally have *high strength but very low ductility of 2–3 %* [101–108]. The low ductility was caused by flaws introduced during the synthesis, including gas-filled pores, unconsolidated particle interfaces, etc. [108]. In fact, although ultrahigh vacuum was used during the IGC, the nano particles still attracted so much gases include CO, CO_2, H_2 and O_2 that the blisters formed in the consolidated sample upon annealing [108]. This is because the extremely high surface area per unit volume for nano particles. Therefore, these samples cannot demonstrate the intrinsic mechanical properties and deformation physics. In other words, the low ductility exhibited in these samples are not the intrinsic property of nanocrystalline metals and alloys.

Another method that has been extensively used to synthesize nanocrystalline metals is mechanical milling, also called ball milling [83,109–113]. It can deform coarse-grained metal powders into nanocrystalline powders with each particle agglomerate consisting of nanocrystalline grains. The as-milled powder usually needs to be consolidated into bulk forms under relatively high sintering temperatures for mechanical testing or applications. It has been a challenge to consolidate nanocrystalline powders while minimizing the grain growth during the consolidation. Lavernia's group milled Al powder in liquid nitrogen and consolidated the nanocrystalline powder using spark plasma sintering [114,115]. It is found that the oxygen and nitrogen contamination during the milling process helped with maintaining the nanostructure during consolidation. This allows the consolidation of relatively large bulk samples for mechanical testing. Koch's group was able to consolidate the nanostructured powders in-situ during ball milling to produce solid sample balls with diameters up to 10 mm, which were further compressed or rolled to make tensile samples [116–119]. Very high ductility (tensile plasticity) was found in the nanostructured Zn samples [116,117], partially due to their high-strain rate sensitivity ($m = 0.15$). Both high strength and high ductility were observed in nanostructured Cu processed in the in-situ ball-milling consolidation [119], which is very significant because its grain sizes were very small (about 20 nm). Dislocation accumulation was believed responsible for the observed high strain hardening. Similar results were also observed in a nanocrystalline Al-5 %Mg alloy processed by in-situ ball-milling consolidation [120]. In addition, nanocrystalline powders produced by ball milling were also used to study the deformation mechanisms of nanocrystalline materials such as partial dislocation emission from grain boundaries and deformation twins [121–127].

Nanostructured metals and alloys were synthesized by electro-deposition, which can produce bulk nanocrystalline metal films for studying mechanical properties [128–136] and deformation physics [126,137–142]. Nanocrystalline samples synthesized by electrodeposition are porosity free although there may be some impurities at grain boundaries. High strength and high ductility have been reported in some nanocrystalline metal films synthesized by electrodeposition [128,143].

Severe plastic deformation (SPD) is a technique that has been extensively used to produce ultrafine grained and nanostructured materials [79,81,100]. Its advantage is to be able to produce large, bulk ultrafine grained (UFG) and nanostructured metals that are porosity free, contamination free and large enough for practical structural applications as well as for studying the fundamental intrinsic properties and deformation mechanism. Because SPD process does not introduce contamination into samples, they can typically refine grains to a few hundred nanometers, depending on the melting temperature and purity of the starting sample. The final grain size is determined by the dynamic balance between dislocation accumulations to refine grains and the dynamic recovery and recrystallization [144]. One of the SPD techniques, high-pressure torsion (HPT), can refine grains of some metals and alloys to below 100 nm, making it ideal for studying deformation mechanisms [145,146].

3.1.2. General observations: High strength but low ductility

The synthesis of bulk nanostructured metals without porosity and flaws using SPD and electrodeposition approaches makes it possible to characterize the intrinsic mechanical properties of nanostructured materials. It is generally observed that nanostructured metals possess strengths that can be several times higher than their coarse-grained counterparts, but their ductilities are very low, which follows the so-called "banana curve" [1,2,57]. The high strength is resulted from the grain boundary strengthening and partially from dislocation hardening for SPD-processed metals with high dislocation density. The low ductility is also resulted from these two factors, with the primary factor being the small grain sizes. For SPD processed samples with relatively large grain size of a few hundred nanometers and high dislocation density, there is limited room for further dislocation accumulation since the dislocation density is already near its saturation level. Both small grain size and high dislocation density lead to low work hardening (strain hardening) and consequently low ductility.

Fig. 6 represents typical mechanical behavior of nanostructured materials under compression and tension [147]. As shown in Fig. 6a, the nano-structured Ti has much higher strength than coarse-grained Ti, but its work hardening rate is reduced to close to zero. The nanostructured Ti was processed using equal-channel angular pressing (ECAP) [82,148] followed by cold rolling [147]. Because compressive testing does not need work hardening to maintain stability, it is possible for the sample to sustain large compressive strain. In other words, the nanostructured sample has high compressive plasticity.

Fig. 6b shows the true stress–strain curves from tensile tests. The most salient tensile behavior of the nanostructured Ti sample is that the necking quickly occurred after yielding, i.e. it has very low ductility, which is defined as the uniform elongation before necking. This is due to its low work hardening capability. It is also seen from Fig. 6b that the necking strain between necking and final

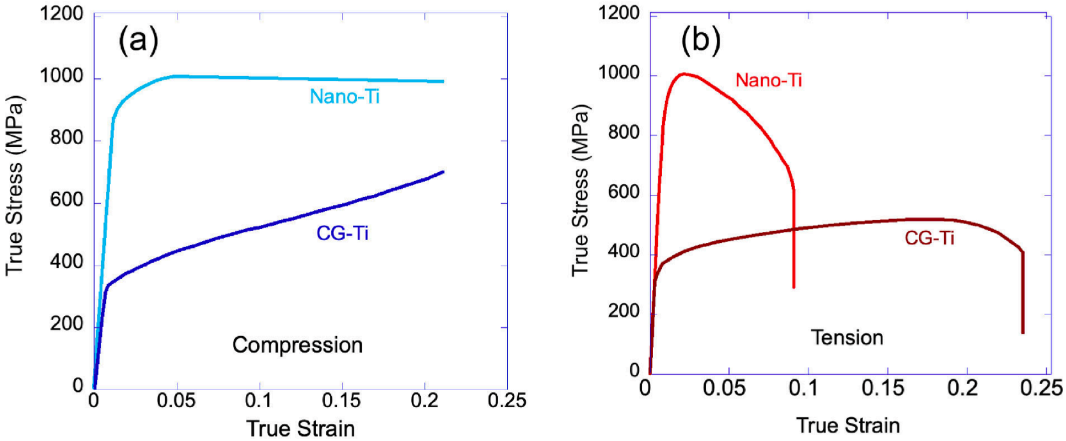

Fig. 6. The mechanical behavior of nanostructured Ti processed by an SPD technique, equal-channel angular pressing (ECAP) [82,148], followed by cold rolling [147]. (a) True stress–strain curves under compression at the strain rate of 2×10^{-4} s^{-1}, (b) True stress–strain curves under tension at the strain rate of 10^{-4} s^{-1}.

failure is very large, which is typically reported in the literature. In fact, most papers on nanostructured metals took the total elongation to failure as the ductility of nanostructured metals [18,57,75], which is problematic [58,59,75,119,149]. As shown, the necking strain is much larger than the uniform elongation. The necking strain is significantly affected by the sample dimension, especially the gage length. For the same displacement in the necking segment, shorter gage length leads to larger necking strain. For standard large samples, this is not an issue since the necking strain is typically very small. Unfortunately, due to the difficulty of making large samples, non-standard small tensile samples were typically used for testing nanostructured materials [58,59,75,119,149], which produced significantly exaggerated total elongation to failure (ductility). In addition, such non-standard samples make it not possible to compare the ductility data reported in the literature. Therefore, uniform elongation should be used as a measure of ductility, which is much less affected by the dimensions of tensile samples [18,58,59].

It should be noted that for nanostructured materials, the yield strength is also determined at 0.2 % plastic strain by most researchers. However, some researchers defined the yield strength at 0.7–1 % plastic strain. We prefer to define it at the 0.2 % plastic strain for easy comparison with literature data.

There are two major factors that affect the strain hardening capability and ductility of nanostructured metals. The first is grain size. When the grains become very small, they can no longer effectively store dislocations in their interior. In other words, nanocrystalline metals will lose their ability to store dislocations, which is the primary mechanism for work hardening. This is because the dislocations are so close to the grain boundaries that they are attracted to grain boundaries. This phenomenon was observed in nanostructured Ti processed by ECAP and cold rolling [150], where it was found that grains and sub-grains smaller than 100 nm are mostly dislocation free. This is the primary reason why nanocrystalline metals have low work hardening rate and low ductility. It should be noted that dislocations have been observed in very small grains below 20 nm, but these are exceptions that don't play a significant role in work hardening.

The second factor is the high initial dislocation density in relatively large grains of nanostructured metals processed by SPD techniques. This factor is active in most cold-worked metals because cold deformation usually produces high density of dislocations. There is a saturation dislocation density for the microstructure. The initial high dislocation density leaves little room for further dislocation accumulation during tensile testing and therefore leads to low strain hardening capability. As shown in Fig. 6, annealing to reduce the initial dislocation density can recover some strain hardening to produce better ductility. However, annealing also typically leads to the reduction of strength.

It should be noted that for nanocrystalline metals with low melting point, tensile testing at room temperature represents relatively high homologous temperature. The enhanced diffusion rate and grain boundary sliding in nanostructured metals could lead to significantly enhanced strain rate sensitivity, which leads to higher tensile plasticity (ductility) [57]. With decreasing grain size, both fcc and hcp nanostructured metals have enhanced strain rate sensitivity while bcc metals behave differently with the strain rate sensitivity decreases first and then increases [63].

3.2. *Strategies to improve ductility*

As discussed in the last section, the primary reason for the low ductility of nanostructured materials is the low strain hardening rate due to the small grain sizes in which dislocations cannot accumulate [18,151]. Therefore, the key to solving the low ductility problem of nanostructured metals is to restore their dislocation accumulation capability. To this end, several strategies have been developed with some success to recover the strain hardening capability and ductility [57,152,153]. Some of the strategies are discussed below.

Early strategies often involve annealing to increase the grain size and decrease the dislocation density, which often results in a trade-off between the strength and ductility [49,100,147,151,154,155]. Specifically, both larger grain size and lower dislocation density from annealing will help with recovering the work hardening capability, but at the same time lower the yield strength.

Several strategies have been developed to improve the ductility of nanostructured metals without sacrificing their strength. These strategies mostly employ the principle of blocking and storing dislocations in the grain interior. The first successful strategy involves

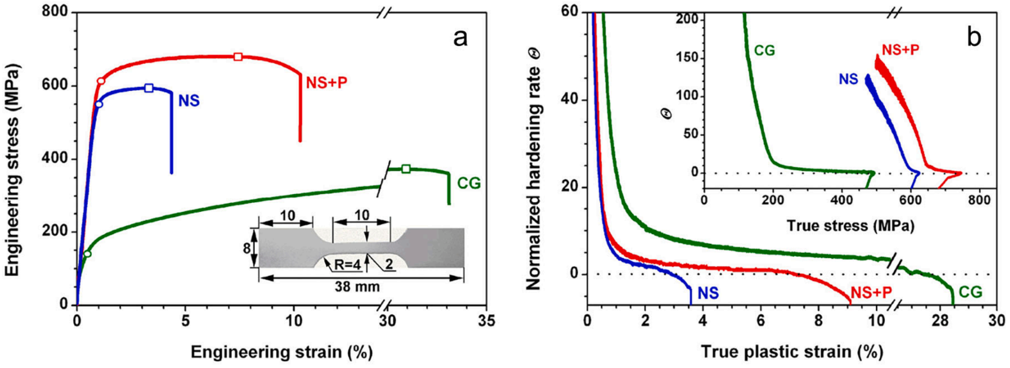

Fig. 7. (a) Precipitation in nanostructured Al 7075 alloy simultaneously increased the strength and ductility. (b) The precipitation in the nanostructured Al alloy increased its strain hardening capability [74].

distributing nano-precipitates in the grain interior to force dislocations to be stored in the grain interior. Zhao et al used an Al7075 alloy to prove this approach [74]. The Al alloy was first solution treated to dissolve all alloy elements into the Al and then quenched to form oversaturated solution. As shown in Fig. 7, the oversaturated solid solution with coarse grains (CG) has a low yield strength of 145 MPa and ductility (uniform elongation) over 30 % (green CG curve). The sample was then deformed by cryogenic rolling to produce a nanostructure with sub-grain sizes about 100 nm, which raised the strength to 550 MPa but lowered its ductility to ~ 3.3 %, a typical strength-ductility tradeoff. Aging the cryo-deformed nanostructured sample to produce high density of precipitates in the grain interior improved the ductility by 1.25 times to 7.4 %. Most significantly, its strength was increased by 12 % to 615 MPa, which breaks the spell of the strength-ductility trade-off. TEM investigation revealed that dislocations accumulated around the precipitates, which verifies that the approach worked very well.

The boundaries of nano twins in nanostructured metals can effectively act as barriers and accumulation sites for gliding dislocations, and consequently improve both the strength and ductility [57,62]. Coherent twin boundaries can be regarded as special grain boundaries with low boundary energies [69]. As dislocation barriers, twin boundaries have the same effect as grain boundaries in increasing the strength [66,128]. The advantage of twin boundaries over grain boundaries is the perfect coherency of the twin boundaries, (see Fig. 8) which makes it difficult for incoming dislocations to be incorporated into the twin boundaries [156]. In other words, twin boundaries are not as good dislocation sinks as grain boundaries. This makes the twin boundaries effective sites for dislocation accumulations, which improves strain hardening rate to produce high ductility. The simultaneous increases in strength and ductility by preexisting deformation twins are demonstrated in Fig. 9 [157].

Twin boundaries can be formed either by growth during the synthesis of nanocrystalline metals [25,129,158] or by plastic deformation of metals and alloys [62,122,139,145,156,159]. Both types of twins were found to be able to simultaneously increase strength and ductility [57,62,66,128,152,160]. It should be noted that detwinning could be activated during plastic deformation, and there is an optimum grain size range for the twinning structure to be stable for enhancing the mechanical properties of nanostructured metals [62,142,161]. In addition, since deformation twinning is significantly affected by stacking fault energy (SFE), the SFE also has effect on the strength and ductility [160,162,163]. Particularly, if the SFE is low enough, deformation twins could be activated in-situ during the tensile testing to increase the strain hardening and ductility[160].

Other strategies for increasing ductility without sacrificing strength of nanostructured materials include high-angle boundaries and low initial dislocation density [164,165], formation of stacking faults [166,167], hierarchical clustering of solute atoms [168], bimodal grain size distribution [49,169], etc. Interested readers are referred to a recent overview [57].

3.3. *Plasticity of nanostructured metals*

Nanostructured metals generally have very high plasticity, as exemplified in Fig. 6a. However, their ductility is usually low, as shown in Fig. 6b. Ductility can be regarded as tensile plasticity, i.e., the ability to deform under uniaxial tensile loading. It is often confused with plasticity in the materials community.

Nanostructured metals can be plastically deformed to very high plastic strains under some deformation modes other than tension, such as compression and rolling [57,147,170]. Plasticity is largely controlled by the number of slip systems that can be easily activated. As a result, hcp metals typically have low plasticity because they don't have the five independent slip systems required by the von Mises criterion [73]. In such cases, nanostructured metals have better plasticity than their coarse-grained counterparts because grain boundary processes such as grain boundary sliding offer additional deformation mechanisms to coordinate the plastic strain. For example, Mg alloys have been found to have improved plasticity after their grains are refined by severe plastic deformation [171–176].

It should be noted that the lack of strain hardening in nanostructured materials makes it susceptible to localized deformation such as shear banding. Shear banding can also occur in deformation modes other than tension. For example, nanostructured bcc metals have been reported to develop shear bands under compression [177–180].

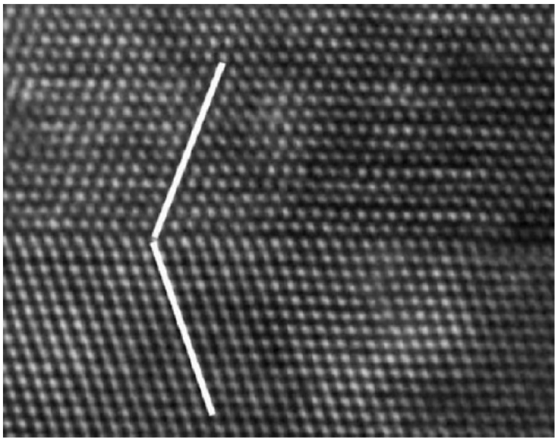

Fig. 8. High-resolution TEM image of a coherent twin boundary.

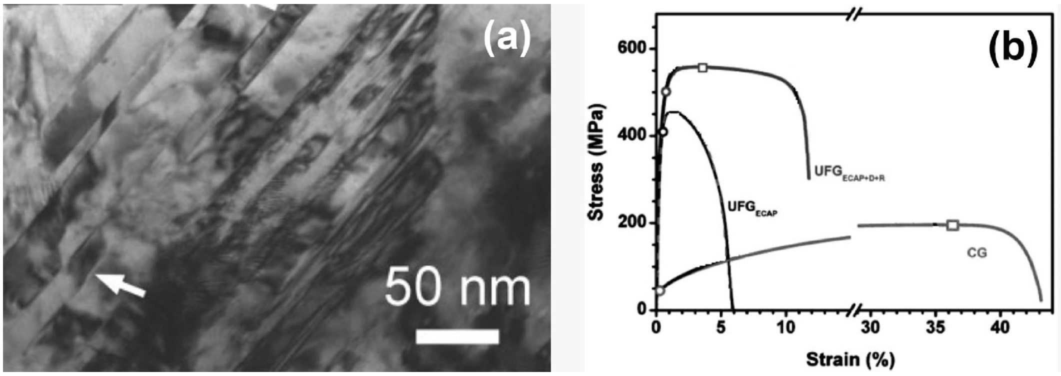

Fig. 9. (a) Deformation twins in Cu formed by ECAP + extrusion + cryogenic rolling (ECAP + E + R); (b) The sample with deformation twins has much higher ductility and also higher strength than the sample without deformation twins processed by ECAP [157].

4. Fundamentals of heterostructured materials

4.1. Classifications of heterostructured materials

Heterostructured (HS) materials can be classified into two different categories: structural and functional. Heterostructured

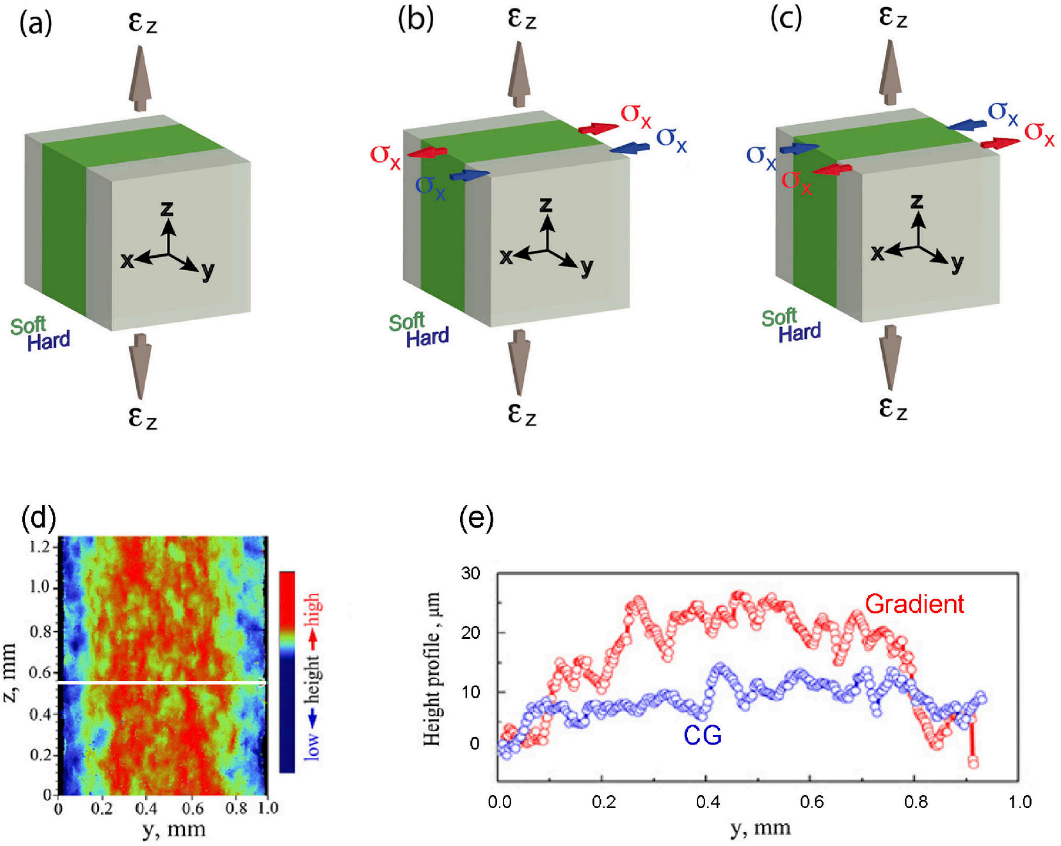

Fig. 10. A heterostructure with a soft coarse-grained layer sandwiched between two hard nanostructured layers. The soft and hard layers have the same elastic modulus. (a) All layers are elastic (elastic-elastic stage); (b) The central soft layer is deformed plastically while the hard layers are deforming elastically (elastic–plastic stage); (c) All layers are being deformed plastically (plastic-plastic stage); (d) Height contour on the side surface, perpendicular to the × axis, in the gauge section of a gradient structured IF steel sample at the tensile strain of 25 % [23]. (e) Measured height profiles along the white line in (d) in the gradient structured sample (red data points). The height profile of a standalone homogeneous coarse-grained (CG) sample after tensile testing to a strain of 0.3 is shown as blue data points for comparison.

structural materials contain zones with dramatic differences in mechanical properties, while heterogeneous functional materials contain zones with dramatic differences in physical properties. Conventional materials may also contain heterogeneous microstructures to some extent, such as a distribution of grain sizes, multiple phases, precipitates, second-phase particles, etc. A critical criterion to differentiate HS materials from conventional materials is that HS materials have a significant synergistic effect, i.e., the mechanical or physical properties of the HS materials are much higher than those predicted by the rule of mixture of the properties of individual zone components. Since so far most reports in the literature have been on HS structural materials, hereafter we simply referred to HS structural materials as heterostructured materials. Heterostructured functional materials will be briefly discussed in a section later.

HS materials possess superior combinations of strength and ductility that are not accessible to their homogeneous counterparts [1,181,182]. The heterostructures can be very diverse, including, but not limited to, heterogeneous lamella structure [2], bi-modal structure [49,164,183,184], gradient structure [6,23,24,185–187], dual phase structure [188–190], harmonic structure [33–35], layered structure [27,29], metal matrix composites [47,48,52,191–194], etc. For the first look, it is very hard to relate these structures with each other because they are so different. However, they are all composed of zones with dramatically different flow stresses [1]. It is this common feature of these heterostructures that renders HS materials superior mechanical properties. These heterostructures have different effectiveness in enhancing mechanical properties. Only after we fully understand the fundamental deformation physics of HS materials can we intelligently design them for the best performance. In this chapter, fundamentals of HS materials will be discussed, and future issues to be investigated will be briefly described.

4.2. *Mechanical incompatibility and strain partitioning*

Heterostructured (HS) materials are composed of zones with dramatically different flow stresses. These zones are mechanically incompatible at the elastic–plastic deformation stage and plastic deformation stage. The mechanical incompatibility leads to strain partitioning during deformation, where the softer zones sustain higher plastic strain [1,2,37,195]. If there is an elastic modulus difference among different zones, which may happen in multi-phase alloys, there may be also an elastic strain incompatibility at the elastic stage. The elastic incompatibility will not be discussed in this paper since it does not have a significant effect on the strength and ductility of HS metals.

For an easy description of the mechanical incompatibility during plastic deformation of heterostructured materials, let’s look at a heterostructure with a soft coarse-grained layer sandwiched between two hard nanostructured layers, as shown in Fig. 10a. This is one of the simplest heterostructures, which can be used to clearly describe the fundamental concepts of mechanical incompatibility.

Assuming that the hard and soft layers have the same elastic modulus, when a tensile strain ε_z is applied in the z direction, the soft and hard layers will deform together compatibly in the initial elastic stage. The sample will contract in the lateral X direction and thickness y direction, as governed by the Poisson ratio ν, i.e.

$$\varepsilon_x = \varepsilon_y = -\nu\varepsilon_z$$

where the values of ν scatter around 0.33 in the range of 0.27–0.44 for most metals [196,197].

With increasing applied strain and corresponding higher stress, the elastic–plastic stage will be reached in which the soft layer will start plastic deformation first while the hard layers remain elastic (see Fig. 10b). For the plastically deforming soft layer, its volume should remain constant during perfect plastic deformation, which leads to an apparent Poisson ratio of $\nu = 0.5$, which is larger than the normal elastic Poisson ratio. In other words, the soft layer will shrink faster than the hard layer in the lateral directions. This will lead to the development of tensile stress in the soft layer and compressive stress in the hard layer, as shown in Fig. 10b. Therefore, the mechanical incompatibility in this layered structure converted the uniaxial tensile stress into complex two-dimensional (2D) stresses.

When the hard nanostructured layers start plastic deformation, the plastic-plastic stage is reached (Fig. 10c). It is known that nanostructured metals have low strain hardening rate and typically start localized deformation and necking soon after yielding [6,17,56,57,75,100,151,198]. On the other hand, the coarse-grained soft layer will have high strain hardening capability to support the unstable hard layers. This sustains the whole sample to deform stably to a relatively high applied strain [6,23]. In other words, at the plastic-plastic stage before the whole sample starts necking, the nanostructured hard layer will shrink faster laterally than the coarse-grained soft layer. Therefore, the normal stresses in the x-direction will be reversed, producing tensile (positive) stress σ_x in the hard layers, and compressive (negative) stress σ_x in the soft layer, as shown in Fig. 10c. The faster shrinking of the nanostructured outer layers were indeed observed in gradient structured interstitial free (IF) steel (Fig. 10d,e). As a comparison, a homogeneous coarse-grained sample did not show obvious faster shrinking in its surface layers during the tensile testing [23].

As discussed in the above model system, the difference in mechanical strength and deformation behaviour converts the applied uniaxial tensile stress into complex, mutually constraining 2D stresses in the soft and hard layers. In addition, although the strains in the loading (z) direction ε_z are uniform and same for all layers, the lateral strains ε_x and ε_y are different in the hard and soft layers, i.e., strain partitioning occurs in the sample due to the mechanical incompatibility. The 2D stresses are caused by the strain partitioning. The model in Fig. 10 is a simplest 2D model. In a real HS material, the heterogeneity is likely-three dimensional (3D), in which the strain partitioning and corresponding internal stress partitioning will be also 3D. Strain partitioning and stress partitioning have been extensively reported in dual-phase steels [190,195,199–201]. However, the mechanism for the stress partitioning needs further study.

The change in stress state may activate multiple slip systems on different slip planes. Dislocations gliding on intersecting slip planes may intersect each other, which produces immobile jogs, or Lomer-Cottrell locks [170], leading to dislocation entanglement and consequent dislocation accumulation to increase strain hardening [23].

As discussed in the following sections, the strain partitioning causes back stress hardening in the soft zones and forward stresses in the hard zones, and together they produce hetero-deformation induced (HDI) hardening.

4.3. Hetero-deformation induced (HDI) strengthening and strain hardening

The primary reason for the observed superior combination of strength and ductility in heterostructured (HS) materials is HDI strengthening and HDI strain hardening [181]. Earlier publications attributed the superior mechanical properties to back stress hardening [1,19,27,37,46,202–208], where back stress is measured from mechanical testing [19,202]. However, it was recently realized that the back-stress concept cannot describe the complete physics that occurs during mechanical testing [181]. Specifically, both back stress and forward stress are developed in the HS materials during the mechanical testing, and the mechanical behaviour is affected by both of them and their interactions. Since both back stress and forward stress are caused by the heterogeneous deformation, the extra strengthening and strain hardening observed and measured in the HS materials were renamed hetero-deformation induced (HDI) strengthening and HDI strain hardening, respectively [181]. The HDI strengthening enhances the yield strength, while the HDI strain hardening helps to retain and improve the ductility.

It should be noted that the HDI strain hardening is also called kinematic hardening in the field of mechanics [203,209–212]. The term “kinematic hardening” describes the kinematic hardening phenomenon during mechanical testing, which is useful for describing the constitutive mechanical behaviour. Here we use the term “HDI hardening” to describe the physical origin of the kinematic behaviour, which is useful in understanding mechanisms to guide materials design for superior mechanical properties. In other words, the terms “HDI strengthening and HDI strain hardening” are more appropriate and useful for the materials community and field.

The HDI strengthening and HDI hardening are the collective result of interactions between back stress and forward stress [181]. The development of back stress and forward stress can be understood with the help of Fig. 11. As shown, geometrically necessary dislocations (GNDs) are emitted from a Frank-Read (F-R) dislocation source in the soft zone. Assuming the Frank-Read source can be activated at a critical shear stress of τ_0, at applied shear stress τ_a ($\tau_a > \tau_0$) there are *n* number of GNDs emitted, which are piled up against the zone boundary. Since these GNDs have the same Burgers vector, they collectively produce a long-range internal stress that prevents more dislocations to be emitted from the Frank-Read source. This is because this long-range internal stress is opposite to the applied shear stress and it offsets some of the applied stress so that the Frank-Read source experiences a local stress below the critical shear stress for dislocation emission. This long-range internal stress may also expel other dislocations whose Burgers vectors have an angle <90° angle with the Burgers vector of the GNDs. Since this long-range internal stress is opposite to the applied shear stress and acts to deter the plastic deformation in the soft zone, it is named the *back stress* (τ_b). For this Frank-Read source to emit more dislocations, higher applied stress is needed to overcome the back stress and the critical shear stress of τ_0, i.e., the minimum stress needed to emit more dislocations from the Frank-Read source is.

$$\tau_a = \tau_0 + \tau_b$$

where τ_0 is the critical stress to activate the Frank-Read source, and τ_b is the back stress. In other words, the back stress makes the soft zone appear stronger.

There is a stress concentration at the pile-up head, with a magnitude of $n\tau_a$ [73,213,214], where *n* is the number of dislocations in the pile-up. The stress concentration is applied on the zone boundary from the soft zone side. On the hard zone side, there must be a stress to balance it. This stress in the hard zone side should promote the deformation of the hard zone. In other words, the stress on the hard zone side has the same effect as the applied stress in driving dislocation slip. Therefore, the stress in the hard zone induced by the GND pile up in the soft zone is named the *forward stress* [181]. At the zone boundary, the back stress and forward stress are the same in their magnitude but opposite in their directions.

The interaction between the back stress and forward stress is not a zero-sum game. At the zone boundary, they cancel each other

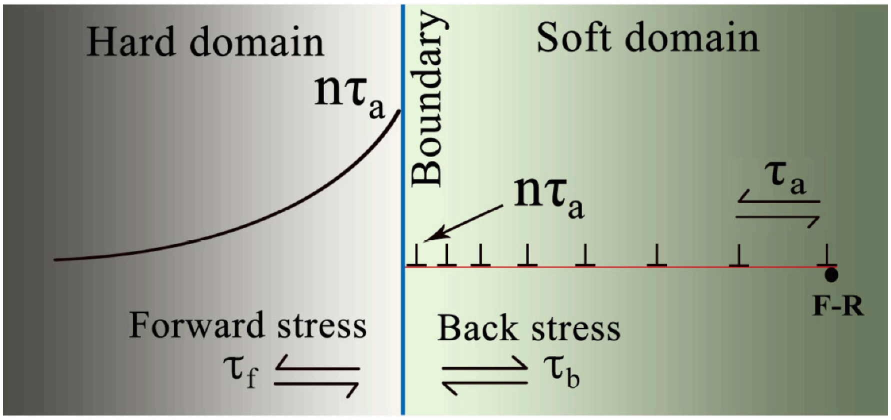

Fig. 11. Schematic of the pile up of geometrically necessary dislocations, which produces back stress in the soft zone and forward stress in the hard zone [181]. The back stress and forward stress are in the same magnitude at the zone boundary but in opposite directions. The back stress is in the opposite direction of the applied stress. The back stress and forward stress collectively produce the hetero-deformation induced (HDI) stress.

because they have the same magnitude but opposite directions. However, they have different profiles as a function of distance away from the zone boundary. This difference gives rise to the observed HDI strengthening and HDI strain hardening.

It should be noted that zone boundary also serves as a segment of grain boundary for grains adjacent to the zone boundary. Other grain boundaries in the interior of a soft zone may also serve as a location for GNDs to pile up, which also produce HDI strengthening and HDI strain hardening. This is a phenomenon that often occurs in conventional homogenous metals and alloys. However, such HDI hardening is usually not very strong, because the strength difference across such grain boundaries is much smaller than that across a zone boundary. The Bauschinger effect observed in conventional metals is mostly produced by this effect [215–218].

Furthermore, in the soft zones, subgrain dislocation cells (subgrains) may also develop during plastic deformation. Long-range back stress may develop inside the dislocation cells and forward stress may develop in the cell walls, which produce HDI strain hardening. However, such dislocation cell walls are less effective in producing the HDI strain hardening than grain boundaries because the crystal misorientations across cell walls are very low, which makes them less effective in blocking GNDs. This subject has been treated extensively by Mughrabi [219–222].

It should be noted that the GND pile-up model in Fig. 11 is an ideal case, which may be frequently observed in fcc metals with low stacking fault energies (SFEs) [15,16] or in hcp metals [2]. In fcc metals with medium to high stacking fault energy, non-planar slip may become the primary slip mode. Due to the easy cross-slip of GNDs, it may be hard for GNDs to pile up. Instead, the GNDs may be accumulated near the zone boundaries, which still produces back stress and HDI stress, but is less effective than the ideal case shown in Fig. 11. This issue is further discussed in Section 4.5.

4.4. *Measurement of hetero-deformation induced (HDI) stress*

As discussed earlier, the HDI stress was misunderstood as the back stress in earlier literature [2,19,181,202]. However, the equations used to calculate the back stress during tensile tests are still valid for calculating HDI stresses. The enhanced yield strength due to the HDI stress can be considered as HDI, while the increase of HDI stress with increasing plastic strain, i.e. the slope of HDI stress as a function of applied strain, can be considered as HDI hardening.

Feaugas [202] presented an equation to calculate the HDI stress from an unloading stress–strain curve:

$$\sigma_h = \frac{\sigma_{u0} + \sigma_u}{2} - \frac{\sigma^*}{2} \tag{9}$$

where σ_{u0} is the initial flow stress at the unloading strain of ε_u (see Fig. 12a), σ_u is the stress at which the unloading stress–strain curve deviates from the linear relationship by an arbitrary plastic strain offset in the range of $5\text{x}10^{-6}$ to 10^{-3} [202,203,223–226], σ^* is the thermal component of the flow stress as defined in Fig. 12a [202,227], which is also called the viscous stress [203].

The advantage of Eq. (9) is that the HDI stress can be calculated from the simple unloading curve, in which the point A is where the unloading started, the segment BC is the linear segment with a slope (modulus) of E_u. However, in practice, the segment BC may not be perfectly linear, leading to relatively large error in determining the points B and C. As mentioned earlier, the plastic strain offset value for determining the point C is also somewhat arbitrary from $5\text{x}10^{-6}$ to 10^{-3}. Due to the very small change in strain during the unloading experiment, a slight change or inaccuracy in the offset strain will lead to a dramatic change in the σ_u value determined on the unloading curve. These uncertainties lead to large uncertainty in the values of σ_u and σ^*, and consequently large scatter in the

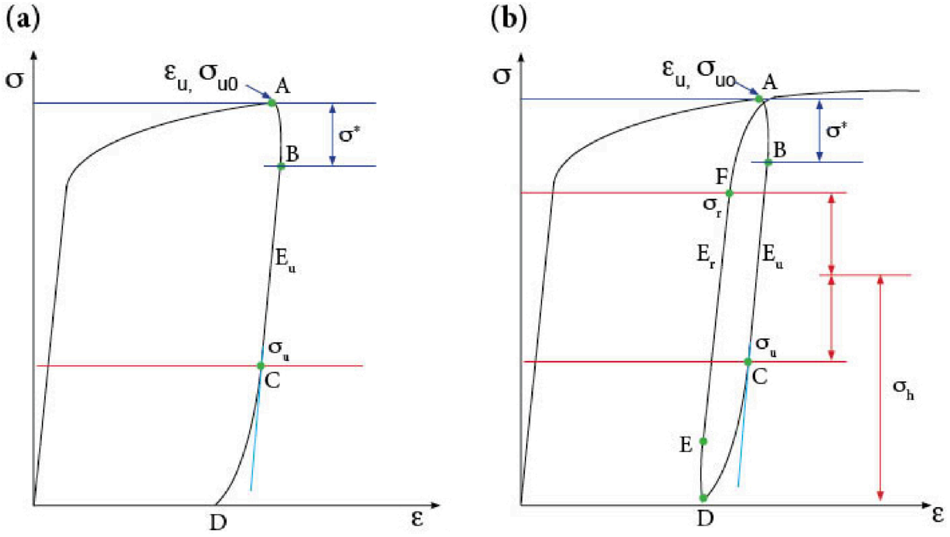

Fig. 12. (a) The unloading curve starting at point A, the viscous flow segment AB, the linear segment BC and the micro-plastic segment CD. The point C is considered the unloading yield point, where micro-plastic strain is started. (b) The complete unloading and reloading curve. The reloading curve DEF consists of the elastic segment EF, where F is the reloading yield point [19].

measured value of the HDI stress σ_h. Another issue about Eq. (9) is that it is a proposed equation, instead of mathematically derived based on some physical assumptions.

To overcome the deficiencies of above methodology in measuring the HDI stress, we have derived a new equation and procedure to measure the HDI stress [19]:

$$\sigma_h = \frac{\sigma_r + \sigma_u}{2} \tag{10}$$

where σ_r and σ_u are defined in Fig. 12b. σ_r is the reloading yield stress. This equation is derived basing on the assumption that the GND pile-up structure is reversible during the unloading–reloading process, which keeps the HDI stress approximately constant during the process. This assumption is consistent with earlier work in the literature [227].

A new procedure to determine the σ_r and σ_u was proposed to reduce the error in calculating the HDI stress. Instead of using the plastic strain offset to determine the σ_r and σ_u values on the unloading–reloading curves, we proposed to use the slope reduction from the linear elastic segments as the criterion to determine them. The physical meaning of this criterion is very clear. For example, a 10 % slope reduction can be regarded as 10 % of the volume undergoing perfect plastic deformation, i.e., 10 % of the volume does not contribute any elastic deformation to the stress–strain curve. Another advantage is that the slope, as derivative of the stress strain curve, is a much more sensitive parameter than strain, which makes it easier to accurately determine the σ_r and σ_u values.

The biggest advantage of the current equation and procedure is that the calculated HDI stress values are very stable with low scattering, as demonstrated in Fig. 13 for gradient structured IF steel [19]. As shown, the HDI stresses determined using 5 %, 10 % and 15 % slope reductions do not scatter very much. This is because the values of σ_r and σ_u deviate in the opposite direction with varying slope reduction, and some of their deviations cancel each other in the Eq. (10). Therefore, this methodology to calculate the HDI stress yields relatively stable HDI stress values for comparisons of data from different experiments.

As discussed earlier, in some cases it might not be easy to determine the slope (apparent Young's modulus) of the linear segments in the unloading–reloading stress–strain curves, because such a linear segment may be very short or even hard to find. In such cases, we suggest to use the slope of the initial elastic loading curve before yielding as the basis for the determination of the σ_r and σ_u values.

It should be noted that the Eq. (10) for calculating the HDI stress was derived under the assumption that the GND structure is reversible during the unloading–reloading cycle. However, when the HDI stress is very high, unloading to zero load and reloading again may not satisfy this condition. One consequence of this issue is that the determined σ_r value may be lower than the σ_u value, which does not make physical sense. In such cases, the unloading process should be stopped and reloading started above a certain stress level to satisfy the assumption for Eq. (10). This issue needs to be further studied.

4.5. Density gradient and configuration of geometrically necessary dislocations

As illustrated in the dislocation pile-up model in Fig. 11, more geometrically necessary dislocations (GNDs) are supposed to be located nearer the zone boundaries. In other words, there is a GND density gradient near the zone boundaries. The GNDs are known to change orientation of the lattice [27,73,214], causing the bending of lattice. Therefore, by measuring the lattice bending as a function of distance from the zone boundary, the GND density as a function of distance from the zone boundary can be calculated.

Electron backscatter Diffraction (EBSD) is a powerful method to measure lattice orientation, and has been used to measure the GND density near zone boundaries in a Cu-bronze layered structure [27]. In this work [27], a kernel average misorientation (KAM) method was used to determine the local misorientation from the EBSD orientation data [228]. The GND density information was calculated using the strain gradient theory by Gao and Kubin [21,229]:

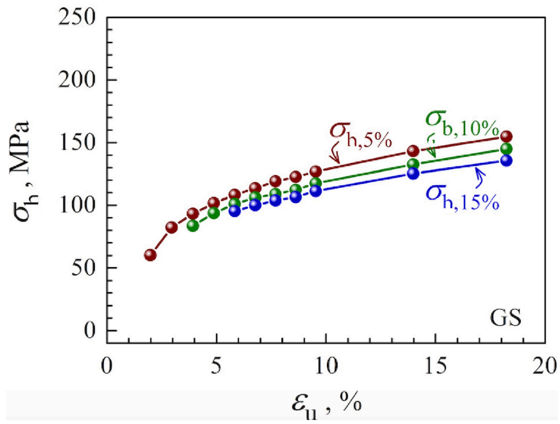

Fig. 13. Evolution of hetero-deformation induced (HDI) stress with increasing tensile strain ε_u for gradient structured (GS) IF steel. $\sigma_{h,x\%}$ represents HDI stress calculated using x% slope reduction from the slope of the linear segment.

$$\rho^{GND} = \frac{2\theta}{ub} \tag{11}$$

where ρ^{GND} is the GND density at points of interest, θ is the local misorientation measured using EBSD, b is the Burgers vector and u is the unit length of the point.

As shown in Fig. 14a, when a copper-bronze layered sample was tested under tension [27], gradient in GND density was built in the Cu layer near the Cu-bronze interfaces (see the red data points at 3 % applied strain and blue data points at 18 % strain). In addition, the GND density gradient increased with increasing applied strain, which explains the increasing HDI stress with applied strain (Fig. 14b). In other words, the GNDs continued to accumulate near the zone boundaries with increasing applied strain, which led to additional HDI hardening. This is consistent with the hypothesis in Fig. 11 that a GND gradient exists in front of the heterogeneous zone boundaries.

It should be noted that the KAM-based approach used in Fig. 14 only produces a scalar value and thus cannot reveal the tensor nature of GNDs. From this point of view, the KAM-based method is not appropriate. Tensor-based approaches have been proposed [230,231] and compared to the KAM approach using the sum of 9 tensor entries as the total dislocation density [228]. The two methods yield very consistent results in terms of qualitatively demonstrating the GND density distribution. The qualitative consistency is not surprising because both methods consider the lattice curvature (orientation change) in a plastically deformed crystal as a measure of stored dislocations, which physically makes sense [232]. Therefore, the KAM-based method still serves as a valid although imperfect method to measure GND density. On the other hand, the tensor approach also needs further development and refinement.

By definition, GNDs collectively produce orientation change of crystal lattice. However, depending on how the GNDs are assembled, GNDs may or may not produce long-range back stress [181]. Shown in Fig. 15a is the Type I assembly of GNDs in which all GNDs are piled up on a single slip plane. This scenario can happen when dislocations emitted from a Frank-Read dislocation source are stopped by a barrier such as HS zone boundary or grain boundary. Since these GNDs have the same Burgers vector, they will repel each other. In addition, their stress fields will be superimposed together to produce a long-range internal stress to repel other GNDs on the same slip plane, or other dislocations whose Burgers vector is at an obtuse angle ($>90^\circ$) with the Burgers vector of these GNDs. This long-range internal stress is called back stress, which will cause forward stress on the other side of the boundary and consequently HDI hardening, as discussed earlier. The slip plane will be also distorted (bent) due to the fact that all of the half planes of the GNDs are on one side of the slip plane.

The second type (Type II) GND assembly is shown in Fig. 15b, in which the GNDs stack up on top of each other. This is a textbook illustration of a low-angle grain boundary, across which there is a misorientation of $\theta = b/h$, where b is the magnitude of the Burgers vector and h is spacing of the dislocations. As shown, as an edge dislocation stacks on top of another edge dislocation, the tensile stress field of the top dislocation overlaps with the compressive strain field of the bottom dislocation. Therefore, there will be no long-range internal stress generated away from the small angle grain boundary. In other words, the Type II GND assembly does not produce back stress or HDI stress.

The third type of the GND assembly is the mixed type in which the GNDs are not piled up on the same slip plane, as shown in Fig. 15c. This will still produce long-range back stress, but it is not as effective as the Type I GND assembly. As discussed in Section 4.3, for fcc metals with low to medium to high SFE, dislocations may not slip in a planar manner, and cross-slipping may occur to destroy the perfect GND pile-up, which leads to the scenario as shown in Fig. 15c. Another mechanism that may produce the scenario as shown in Fig. 15c is the interactions of GNDs with other dislocations from other slip-planes to form dislocation entanglements or a dislocation cell structure near the zone boundaries. It was also reported in gradient nanotwinned Cu that when the twin thickness is in the nano-scale (<100 nm), the conventional GND pile as shown in Fig. 11 becomes impossible, and the GND structure may become more complex [233,234].

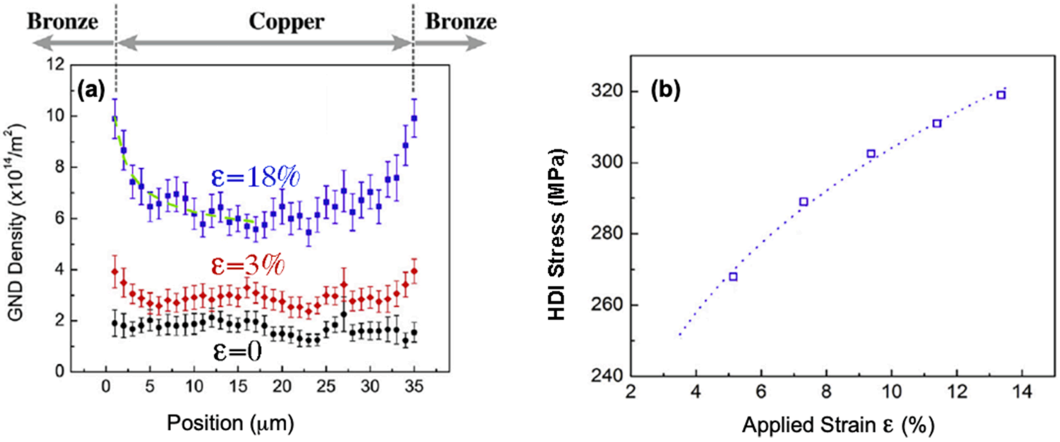

Fig. 14. (a) Density of geometrically necessary dislocations (GNDs) in copper near the copper-bronze interfaces as measured using EBSD, and (b) Hetero-deformation induced hardening with applied strain, in a copper-bronze layered processed by accumulative roll bonding followed by annealing.

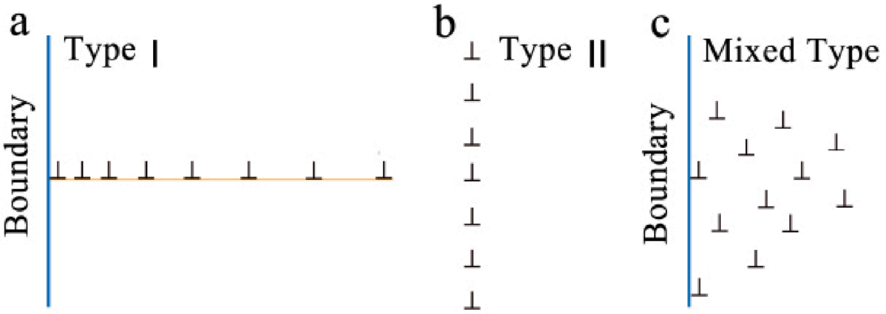

Fig. 15. Assemblies of geometrically necessary dislocations (GNDs) [181]. (a) Type I assembly: piling up of GNDs on a slip plane in front of a boundary or barrier. (b) Type II assembly: stacking up of GNDs on multiple slip planes. (c) Mixed Type: a mixture of type I and Type II assemblies.

Another type of dislocation assembly is the random distribution in the spacing and Burgers vectors of dislocations as in the case of dislocation entanglement (see Fig. 16). Such dislocations are collectively called statistically stored dislocations [20,21]. Stress exists in short ranges near individual dislocations, but in the long-range, the stress fields collectively cancel out. Such type of the dislocation assembly provides conventional dislocation hardening by making it hard for other gliding dislocations to move through them, as described by Eq. (3).

4.6. Strain gradient and dislocation mechanism

4.6.1. Strain partitioning in heterostructured materials

It is well known that there is strain partitioning in dual-phase steels [2,37,188,190,195,199–201,235,236], which are a type of HS materials [1]. The strain partitioning is also well demonstrated in an HS Ti sample processed by asymmetric cold rolling and partial recrystallization [2]. As shown in Fig. 17a, before tensile testing, the recrystallized large grains are equiaxed before deformation. The black matrix are grains smaller than 1 μm, most of which are un-recrystallized. After 9.5 % tensile strain, the equiaxed large grains became elongated in the tensile strain direction (Fig. 17b). The strain in these large grains can be estimated according to the ratio of their length to width, which has an average value of 45 %. This means that the small grains in the black matrix are deformed to strains much lower than the average 9.5 %. However, at the zone and grain boundaries between the large grains and the small grains the strain needs to be the same to prevent boundary cracking. Therefore, there must be strain gradients near the zone boundaries to accommodate the large strain differences between different zones.

4.6.2. Pile-up of GNDs and strain gradient

It has been theorized that geometrically necessary dislocations (GNDs) are needed to accommodate the strain gradient near the zone/grain boundaries [21,232]. This can be explained with the schematics in Fig. 18 [1]. As shown in Fig. 18A, there is a boundary between a fine-grained hard zone and large-grained soft zone. A Frank-Read source at point X emits dislocations with the same Burgers vector toward the zone boundary. These dislocations are GNDs and are piled up in front of the zone boundary. Their stress fields superimpose on top of each other to create a long-range internal stress, which is called back stress in soft zone to impede further dislocation emission from the dislocation source. Since plastic strain is produced by the slip of dislocations, the plastic strain at the zone interface is zero because no dislocation has reached it, while the plastic strain is highest at the dislocation source. Collectively, these

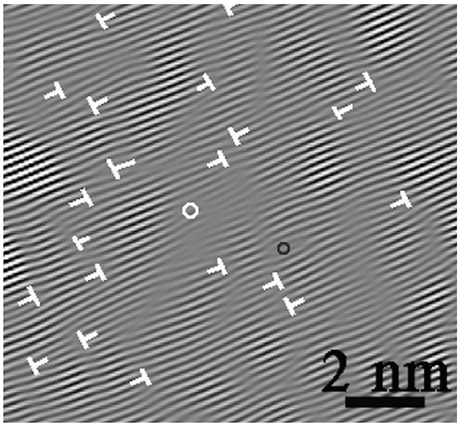

Fig. 16. Statistically stored dislocations with no long-range internal stress.

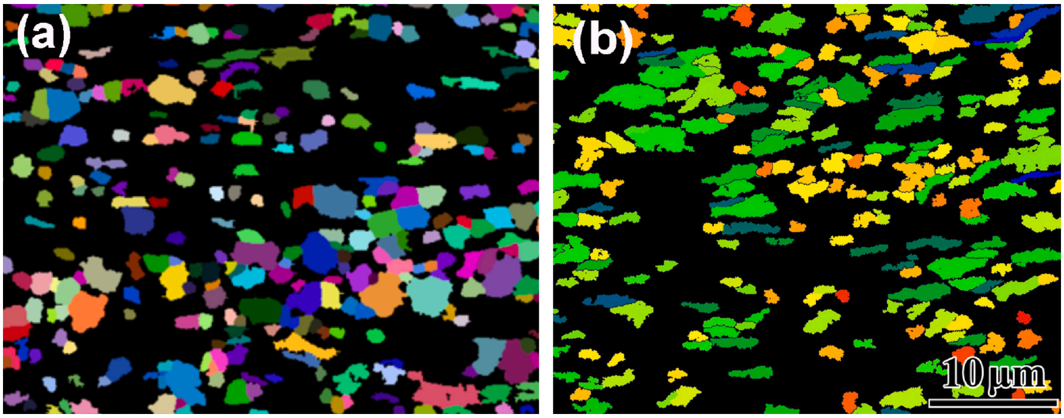

Fig. 17. (a) EBSD images of recrystallized grains>1 μm in heterostructured Ti processed by asymmetric cold rolling and partial recrystallization [2]. The black matrix is areas where grains are mostly not recrystallized. The recrystallized grains are equiaxed before tensile testing. (b) Elongated recrystallized grains after tensile testing to 9.5 % true strain.

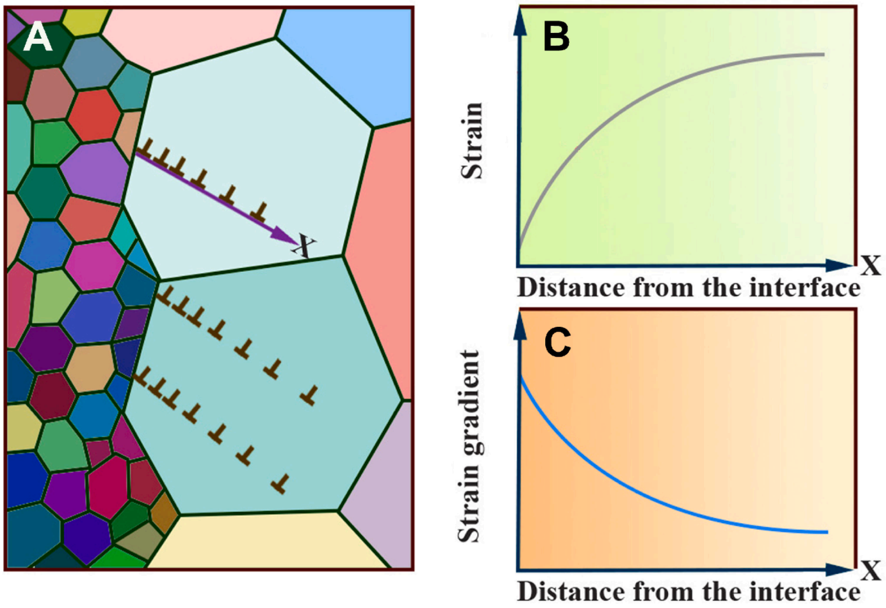

Fig. 18. A) Schematics of pile-ups of geometrically necessary dislocations (GNDs) in front of a zone interface [1]. The GNDs are emitted from Frank-Read sources in the interior of coarse grains of the soft zone. B) Plastic strain profile in front of the zone interface. C) Strain gradient profile in front of the zone interface.

GNDs produce a strain profile near the zone boundary, as schematically illustrated in Fig. 18B. The derivative of the strain profile, $d\varepsilon/dx$, where × is the distance from the zone boundary, is the strain gradient (Fig. 18C). As shown, $d\varepsilon/dx$ is positive (>0). Therefore, we designate such a strain gradient as the *positive strain gradient*.

4.6.3. Strain gradient measurement near zone boundary

To verify the hypothesis of strain gradient described in Fig. 18c, a high-resolution digital correlation technique was developed using semi-in-situ scanning electron microscopy [13]. A Cu-bronze layer-structured sample (Fig. 19a) was fabricated by accumulative roll bonding followed by appropriate annealing to recrystallize the deformed structure, which resulted in alternative coarse-grained Cu layers and ultrafine-grained bronze layers due to the difference in their thermal stability. The soft Cu layers and hard bronze layers had over 100 % difference in hardness, as shown in Fig. 19b. Strain gradient was found near the zone (layer) boundaries as shown in Fig. 19c. As shown, there are high strain (ε_{xx}) peaks at the zone boundaries that become higher with increasing applied strain. ε_{xx} is the strain in the sample thickness (lateral) direction, which is perpendicular to zone interfaces. There is theoretically no inter-layer mutual constraint in this direction so that the strain gradient could be clearly measured. The strain in the lateral direction was caused by the Poisson's ratio, which is why the ε_{xx} is negative. However, there is little strain (ε_{yy}) gradient in the tensile direction (y direction). This is

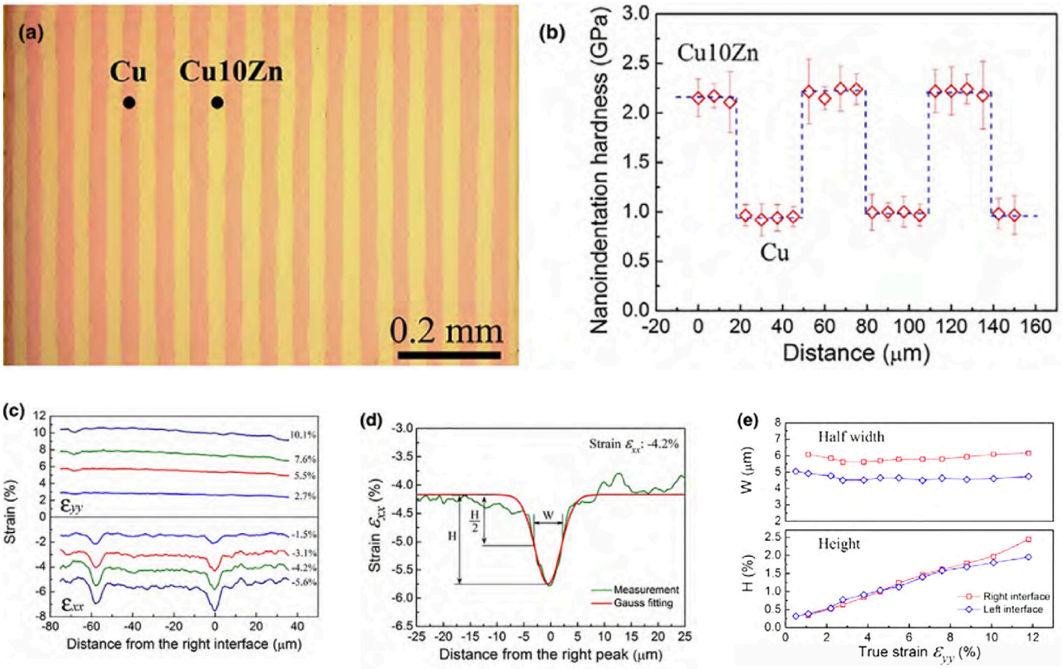

Fig. 19. (a) Cu-bronze layer-structured sample processed by ARB + annealing. (b) The microhardness difference in the Cu and bronze layers. (c) The evolution of strain across and two zone (layer) interfaces with increasing tensile applied strain, which is in the y direction. ε_{xx} is the lateral strain in the sample thickness direction, and the ε_{yy} is the longitudinal strain in the sample length (tensile) direction. (d) The strain profile across a zone interface, which is fitted with a smooth peak to calculate peak height H as well as its width w at half height. The latter is also called interface affected zone (IAZ) [13], later renamed the hetero boundary affected region (HBAR) [397]. (e) The evolutions of peak height H and width w at half height with increasing applied strain.

because a uniform external tensile strain is applied to all layers in the y direction for the layer-structured sample.

An ε_{xx} strain peak is fitted with a smooth curve in Fig. 19d with a peak height H. The peak width at half height maximum is designated as w, which was regarded as the width of the hetero boundary affected region (HBAR). As shown in Fig. 19e, the HBAR width w remains constant with increasing applied tensile strain, while the peak height increases with the applied strain, indicating that the strain gradient increased with applied strain in the HBAR.

From Fig. 19e, the maximum strain occurs at the peak maximum. Since ε_{xx} strain is negative, the more negative the value, the

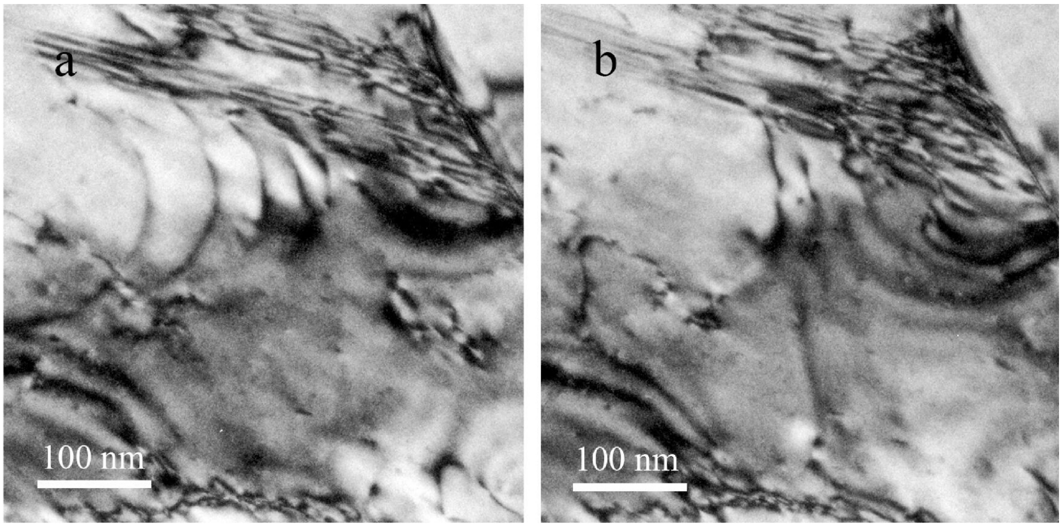

Fig. 20. TEM images of a Frank-Read sources in a Cu grain emitting dislocations toward the zone boundary. (a) A Frank-Read source produced five dislocation pile-ups against the interface, (b) The deactivation of the dislocation source.

higher the strain. This observation is clearly opposite to the scenario depicted in Fig. 18, where the plastic strain is zero at the zone interface, and increases with the distance from interface. In other words, there is a negative strain gradient near the interface, which cannot be explained by the conventional GND pile-up model based on Frank-Read dislocation sources. From conventional textbook understanding, the plastic strain should be higher at locations closer to the dislocation sources. Therefore, the results in Fig. 19 point to the interface as the dislocation sources, which is consistent with some early minority opinions that the dislocations are primarily from the ledges on the grain boundaries instead of Frank-Read sources in the grain interior [237,238]. Grain boundaries indeed become the primary dislocation sources in the nanocrystalline metals [62,125,126,239]. However, for coarse-grained metals, this needs further experimental study.

4.6.4. Dynamic Frank-Read source produces negative strain gradient

To probe the real mechanism for the unexpected observation of negative strain gradient in Fig. 19d, in-situ TEM observation under tension was performed on a Cu-bronze sample near the zone interface. Frank-Read dislocation sources were indeed observed in a Cu grain adjacent to the zone boundary (Fig. 20). Although dislocation emissions from the zone boundary were also observed in-situ, the overwhelming majority of dislocations were observed emitted from Frank-Read sources in the Cu grain interior. This observation proves false the longstanding minority argument that there are rarely Frank-Read dislocation sources in grain interior and the dislocations are mostly emitted from grain boundary ledges in coarse-grained metals [237,238].

In our conventional knowledge from the textbook, it is assumed that once a Frank-Read source is formed, it will continue to emit dislocations during the deformation. In fact, this assumption is what is based on in the discussion of Fig. 17, which reaches the conclusion of positive strain gradient. The observation of negative strain gradient in the *in-situ* TEM experiment clearly demonstrates the problem of the conventional static Frank-Read dislocation source concept.

A major discovery of this *in-situ* observation is that the Frank-Read dislocation sources were dynamically formed and deactivated over the entire deformation process. The observation of the dynamic Frank-Read source changes our understanding on how the Frank-Read sources work to supply dislocations needed for continuous plastic deformation. It has profound implications on several well-known and accepted theories/hypothesis, as discussed below.

i) *The negative strain gradient near the zone boundary was formed by the density-gradient of dynamic Frank-Read sources*. It was observed in the *in-situ* TEM experiment that Frank-Read sources were dynamically formed, and then deactivated after emitting some GNDs toward the zone boundary. The closer it is to the zone boundary, the more likely a Frank-Read Source is formed, thus producing a Frank-Read source density gradient near the zone boundary, which produces the negative strain gradient, although each Frank-Read source alone may produce a positive strain gradient. It is also observed that most GNDs produced by the Frank-Read sources glided to and were absorbed by the zone boundary, which did not contribute to any individual strain gradient.

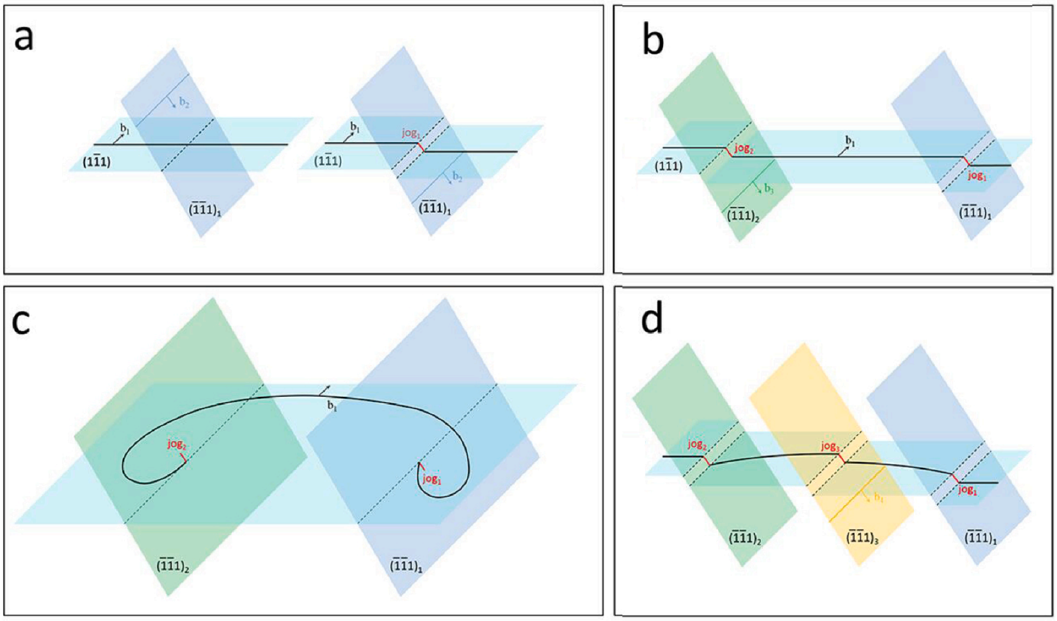

Fig. 21. Schematics of the dynamic generation and deactivation of Frank-Read dislocation sources [240]. (a) a sessile jog is produced on dislocation 1 due to the intersection with dislocation 2, (b) Two sessile jogs are produced to form a potential Frank-Read source, (c) the Frank-Read source is activated when the resolved applied stress reaches or surpasses the critical stress, (d) the Frank-Read source is deactivated when the third sessile jog makes the dislocation segments so short that the applied stress is no longer high enough to bow them out.

ii) There is no correlation between the plastic strain gradient and the GND pileup and accumulation near the zone boundaries. In a gradient plasticity theory by Gao *et al*, it was assumed that the strain gradient and the GND density near a zone/grain boundary can be quantitatively corelated [21,232]. This concept has been widely accepted by the scientific community [13]. This assumption was also based on the static Frank-Read source model described in Fig. 18. The *in-situ* TEM observation of GNDs disappearing into the zone boundaries indicates that the strain gradient cannot be related with the GND density near the zone boundary. This provides solid experimental support for revising and further developing the gradient plasticity theory.

4.6.5. Formation and deactivation mechanism of dynamic Frank-Read sources

The dynamic formation and deactivation of Frank-Read dislocation sources can be described with the help of Fig. 21. As shown in Fig. 21a, dislocation 2 is gliding on a $(\bar{1}\bar{1}1)$ plane in a face-centered cubic metal and intersects dislocation 1 gliding on a $(1\bar{1}1)$ plane, which produces a sessile jog on dislocation 1. If another sessile jog is produced on the dislocation 1 as shown in Fig. 21b, two points on the dislocation 1 will be pinned down and a potential Frank-Read source is formed. It will be activated when the applied stress reaches or surpasses the critical stress [214], see Fig. 21c,

$$\tau_c = \frac{2Gb}{l} \tag{12}$$

where G is the shear modulus, b is the Burgers vector magnitude and *l* is the distance between two pinning points. Considering that fcc metals have four intersecting slip planes, it logically has a high probability that a dislocation will be intersected by another dislocation gliding on different slip plane. Therefore, the probabilities for formation of potential Frank-Read sources and their activations are relatively high during the plastic deformation, as indicated by the observation of their dynamic formations under the in-situ TEM [240].

When another jog is produced between the first two jogs on the dislocation 1 as shown in Fig. 21d, two shorter segments will be produced, and the critical stress for operating these two shorter segments will be higher according to Eq. (12). If the applied resolved stress is lower than the critical stress for both shorter segments, this Frank-Read source will be deactivated, as frequently observed in the in-situ TEM experiment. This is not surprising considering the high probability of dislocations intersecting each other.

The dynamic formation and deactivation of Frank-Read sources are caused by the intersecting dislocations during the plastic deformation. Considering the high probability of dislocations intersecting each other, especially in fcc and bcc metals, the dynamic nature of the Frank-Read sources should be a common phenomenon. This has not been reported earlier because it can only be observed by *in-situ* TEM experiments. Most earlier TEM studies on dislocation are post-mortem, which is not capable of revealing this dynamic nature of Frank-Read sources.

4.7. HDI hardening vs strain gradient

As discussed earlier, the hetero-deformation induced (HDI) stress is caused by the interaction between the back-stress and forward stress [181]. The back stress is caused by the piling up of geometrically necessary dislocations (GNDs), and the forward stress is caused by the stress concentrations at the pileup head of the GNDs. Therefore, it can be deduced that the HDI stress is directly related to the pileups and accumulations of GNDs and GND density. Since the GND density cannot be quantitatively corelated with the strain gradient, as discussed in the last section, it can be reasonably hypothesized that the HDI hardening cannot be quantitatively corelated with the strain gradient near the zone boundaries.

To verify the above hypothesis, the evolution of strain gradient near the zone interfaces in a Cu-bronze layer-structured sample was measured using high-resolution DIC with increasing applied tensile strain, which is compared with the evolution of HDI stress [241].

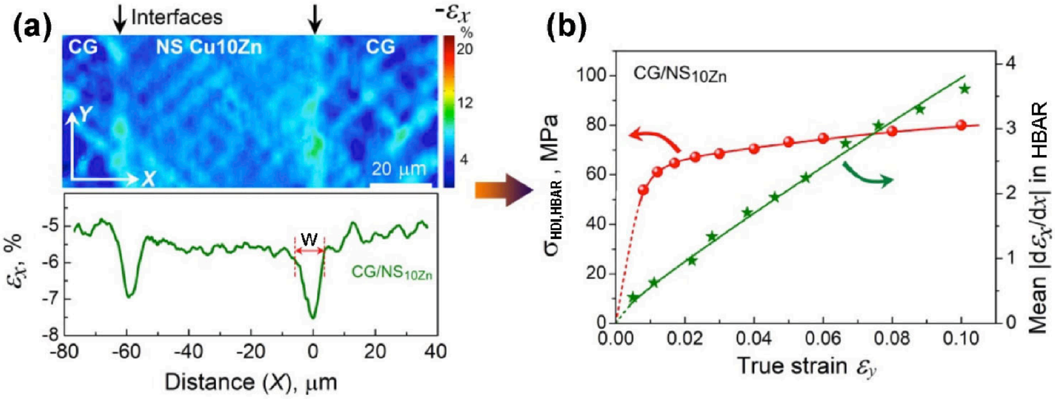

Fig. 22. Strain gradient vs HDI stress in a copper-bronze layer-structured sample with increasing applied true strain [241]. (a) DIC image and the strain profile across two zone boundaries, (b) the HDI stress in the hetero boundary affected region (HBAR) (red curve), and the mean strain gradient $|d\varepsilon_x/dx|$ in the HBAR (green curve).

As shown in Fig. 22a, hetero boundary affected regions (HBARs) were formed near two zone interfaces. Fig. 22b shows that the HDI stress in the HBAR, $\sigma_{HDI,HBAR}$ initially increased rapidly and changed to slower increase after a certain strain. This change occurred at the yield point on the stress–strain curve [241]. From these observations, it appears that the HDI hardening was proportional to the strain gradient before yielding, but changed to slower increase after yielding because the GNDs density in the HBAR no longer increases proportionally with the strain gradient. This is due to the fact that some of the GNDs will be absorbed by the zone boundaries as observed by the in-situ TEM experiment [240].

4.8. Strain banding and localization

Experimental evidence reported so far indicate that heterostructures promote the formation of local strain bands [13,17,198,242,243]. The earliest observation of strain banding was made on a copper-bronze layer-structured sample [13]. As shown in Fig. 23, the deformation strain is not uniform across the zone boundaries in the layer. Instead, local strain bands were developed from two directions that are about 45° from the vertical loading direction, i.e., the maximum shear stress direction, suggesting that they were driven by applied shear stress. Note that these strain bands have higher strain intensity near the zone boundaries, which produces the observed negative strain gradient. It is believed that the strain in the bands is dominated by shear strain, but this needs experimental verification. One obvious feature of these bands is that they are dispersed through the entire sample.

The dispersive strain bands were also observed on the surface of a gradient structured Ni sample [242]. The sample was processed by rotationally accelerated shot peening (RASP) with 2 mm steel balls [244], which produced two nanostructured surface layers with an average grain size of 68 nm and a coarse-grained central layer. As shown in Fig. 24, with increasing applied strain from 1.09 % to 21.06 %, dispersive local strain bands were developed over the nanostructured surface of the gradient Ni sample. These dispersive strain bands were called shear bands in the paper [242] because the orientations of the strain bands are close to the 45° to the loading direction, i.e., the maximum shear stress direction (see Fig. 24A2). These shear bands can be also called local strain bands because further study is needed on their origin.

Fig. 25a shows the evolution of strains in ε_y (tensile direction) strain bands with increasing applied strain. As shown, the strain peak in the strain bands becomes higher with applied strain. Fig. 25b shows similar trend in the ε_x (lateral) strain band, which is negative in values. The strain band peak height and width at half of peak maximum is defined by fitting the experimental curve with a Gauss function [242]. It is demonstrated in Fig. 25c that the average width of strain bands, $\overline{W}$, remained constant with increasing applied strain, while the strain peak height increased with applied strain. Fig. 25d shows that the spatial density of strain bands increased quickly initially, but reached a saturation at ∼ 3 % strain.

The stable evolution of dispersive strain bands was attributed to the constraint by the stable CG central layer, which prevented the strain bands from penetrating deep into the CG central layer. In addition, grain coarsening occurred in the nanostructured strain bands, which acted to help with regaining strain hardening capability and stabilizing the strain bands. The constant strain band width and increasing strain peak indicate that the strain gradient in the strain bands increased with applied strain, which may increase the GND density and HDI hardening in the strain bands [1]. In other words, the dispersive strain bands may have helped with increasing strain hardening rate and retaining the ductility of the gradient structured sample.

In contrast to the gradient structured Ni, the CG Ni samples did not produce strain bands under tensile strains up to 21.86 %. Strain bands did appear in nanostructured Ni, but there only a few large strain bands appeared and quickly failed the sample. In other words, the gradient structure promoted the formation of stable, dispersive strain bands [242].

Yuan et al reported another phenomenon of stable local strain banding in a gradient structured interstitial free (IF) steel [17]. As shown in Fig. 26, strain localization occurred at two locations at 1.0 % strain. The top strain localization was formed by two crossing strain bands, which grew steadily with applied strain up to 20.6 %. The strain localization spread along the gage length stably without failing the sample. The difference between this example and the dispersive stain bands in gradient Ni (Fig. 25) is that this IF steel sample had very thick gradient layer that extended all the way to the center (Fig. 26b), which is believed the reason for the formation and stable propagation of this primary strain localization. In other words, it appears that if the central CG layer is thick and the gradient layer is thin, it will be difficult for the strain bands to propagate side way to grow its width (e.g., Fig. 25). However, if the gradient layer is very thick and central CG layer is too thin to effectively constrain the strain bands, the strain bands may grow in width to propagate

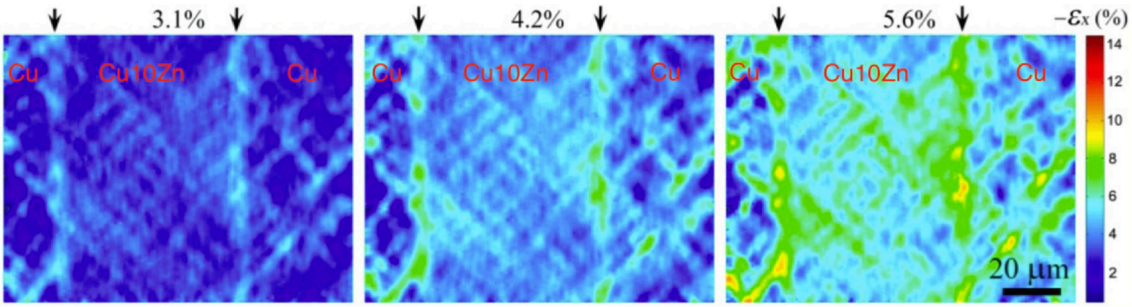

Fig. 23. Strain bands formed during tensile testing of a copper-bronze layer-structured sample at 3.1%, 4.2% and 5.6% strain, measured by high-resolution DIC [13]. Black arrows mark the zone boundaries.

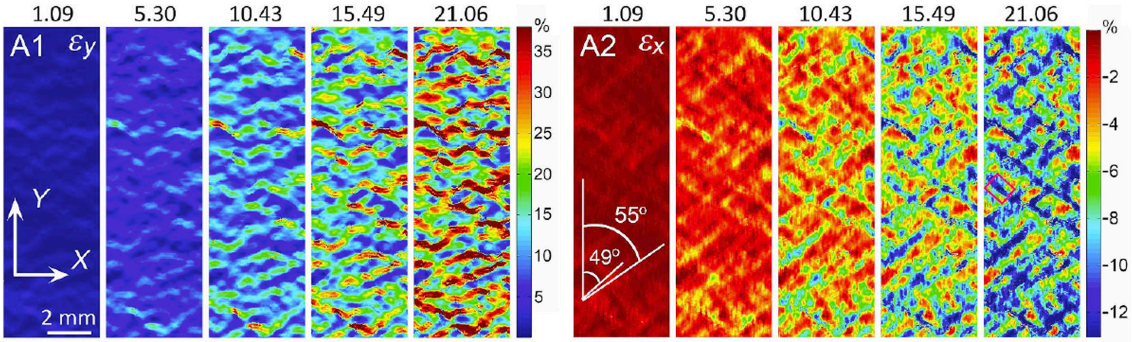

Fig. 24. Dispersive strain banding on the surface of a gradient structured Ni processed by RASP [242]. (A1) Strain map using strain ε_y in the tensile direction. (A2) Strain map using strain ε_x in the lateral direction. Note that ε_x is negative because the lateral strain is caused by the Poison's ratio. The strain bands are oriented at 49° − 55° to the tensile loading direction (y).

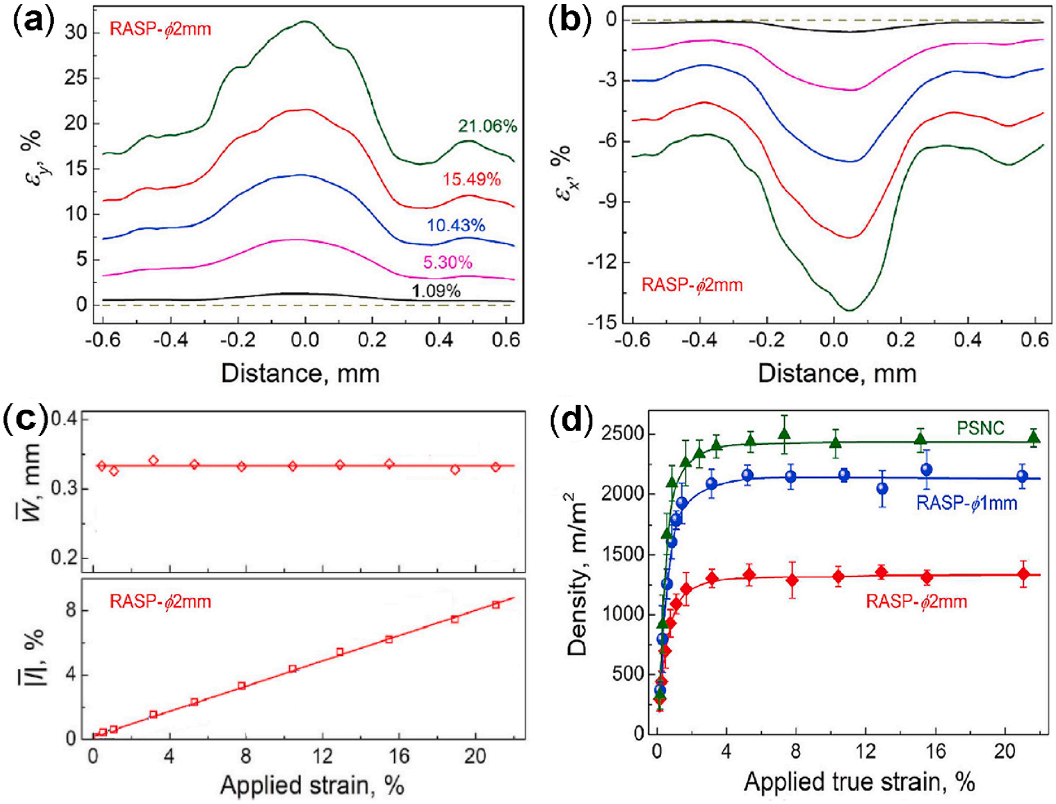

Fig. 25. Evolution of strains in strain bands in gradient structured Ni with increasing applied strain from 1.09% to 21.06% [242]. (a) Evolution of strains in ε_y (tensile) strain bands. (b) Evolution of strains in ε_x (lateral) strain bands. (c) The average width at half maximum of the strain peak remained constant while the average strain peak height increased with applied strain. (d) The evolution of the density of strain bands with increasing applied strain for three different gradient Ni samples.

along the gage (e.g., Fig. 26).

Interestingly, as shown in Fig. 26c, there is a sharp hardness drop in the strain bands at the early stage, *i.e.*, strain softening. This was caused likely by the deformation induced grain growth in the nanostructured surface layer. This phenomenon has been extensively reported for nanostructured metals [24,144,245–249]. Surprisingly, the microhardness increased in the strain localization zone upon further strengthening, indicating that the strain hardening capability can be recovered to some extent in the strain bands, which benefits the overall strain hardening rate and helps with retaining ductility.

The promotion of strain bands by heterostructures is clearly demonstrated in a bi-modal heterostructured Cu [198]. The Cu sample was first processed by Equal Channel Angular Pressing and cold rolling to produce ultrafine grained (UFG) structure and then annealed

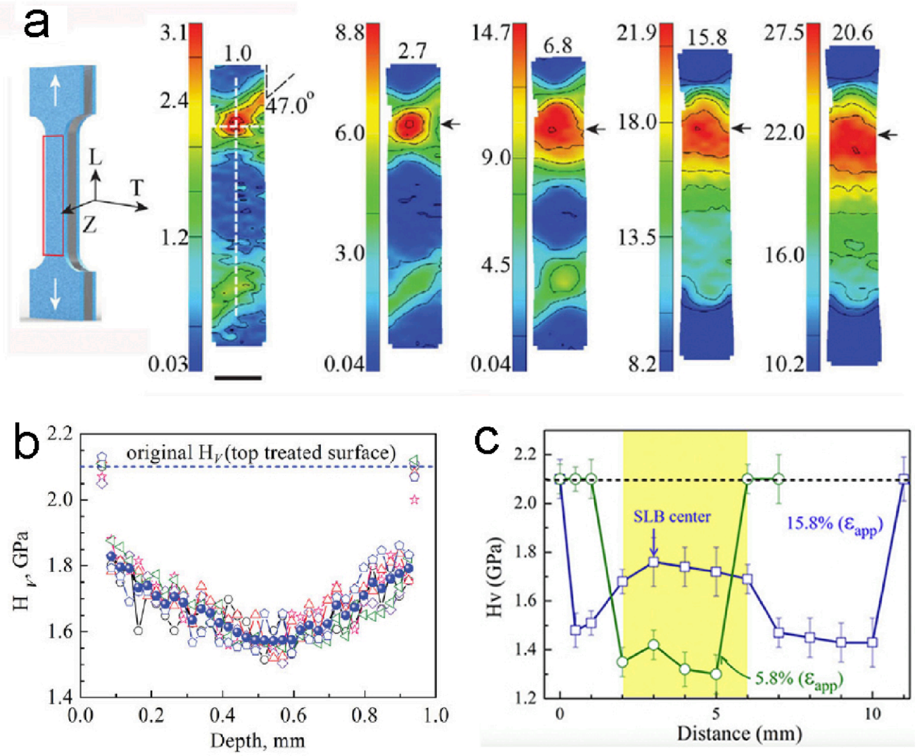

Fig. 26. Stable propagation of a local strain band in gradient structured IF steel with thick gradient layers [17]. (a) Tensile sample with a gage length of 10 mm, and strain evolution map on the surface of the entire gage length. (b) The microhardness profile along the thickness indicates that gradient layers extended all the way to the center. (c) Hardness dropped in the local strain bands and subsequent recovery of strain hardening capability.

to produce bi-modal heterostructure and coarse-grained (CG) structure. As shown in Fig. 27, under similar applied tensile strain, the bimodal samples with 30 % and 70 % recrystallized coarse-grains exhibited severe dispersive strain bands, while the CG Cu sample exhibited much less severe dispersive strain bands. The UFG sample failed at very low tensile strain before the dispersive strain band was developed.

It was concluded that both UFG zones and CG zones are needed to develop dispersive strain bands [198]. During the tensile deformation, the piling up of GNDs against zone boundaries will produce back stress in the CG zones, and forward stress in the UFG zones in the form of local stress concentrations. The local stress concentrations in the UFG zone (forward stress) may initiate local plastic deformation. Due to the low strain hardening capability of the UFG zones, local strain bands may be nucleated in the UFG zones. However, these local strain bands will be stopped once they cross into the CG zones because 1) CG zones will deform readily by dislocation slip to relieve local stress concentration and 2) CG zones have high strain hardening rate to stop and stabilize deformation. The constraint of active strain bands by CG zones makes it possible for other strain bands to form at other locations, therefore producing stable, dispersive strain bands.

It should be noted that these strain bands were called shear bands in the earlier publications [17,198,242]. This is because the orientation of these strains is very close to the maximum shear stress orientation, that is, 45° to the tensile loading direction. In addition, any dislocation slip in these strain bands is certainly driven by shear stress. However, there is no direct evidence that there is macroscopic shear strain in the strain bands. Recently, shear bands were indeed observed in heterostructured Ni under SEM [250]. It is still not clear if shears strain is involved in all shear bands. This needs to be further studied.

4.9. Hetero-deformation induced (HDI) stress and Bauschinger effect

Bauschinger effect has been observed extensively in conventional metals and alloys [216,217]. Typical Bauschinger effect is illustrated in Fig. 28a [218], in which $|\sigma_{ry}|\langle|\sigma_f|$. In conventional materials, the Bauschinger effect usually increases with increasing prestrain, as shown in Fig. 28b. In other words, σ_y becomes more negative with increasing tensile strain, but this increase is slower than σ_y. As shown in Fig. 28c, in gradient structured Cu, the σ_y becomes less negative with increasing tensile strain, which leads to higher reverse yield softening (Fig. 28d). In other words, there is a strong Bauschinger effect in the gradient sample, which is similar to the trend of the HDI stress. This is because the Bauschinger effect and the HDI hardening have the same physical origin [218]. It is suggested that the HDI hardening can be used as a quantitative measure of the Bauschinger effect.

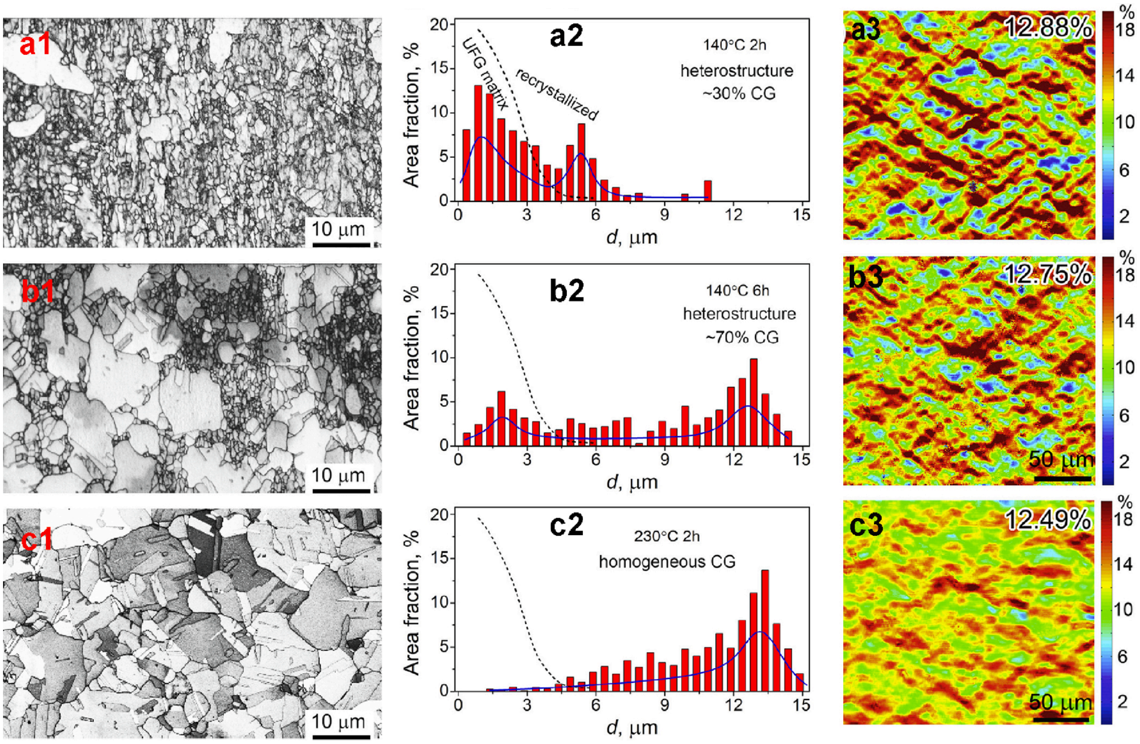

Fig. 27. Bi-modal heterostructures in Cu the formation dispersive strain bands [198]. (a1) Bi-modal heterostructure with 30% recrystallized coarse-grains (CG) and 70% of ultrafine grained Cu, (a2) its bi-modal grain size distribution histogram, and (a3) its dispersive ε_y (tensile strain) strain bands after 12.88% tensile loading. (b1) Bi-modal heterostructured Cu with 70% recrystallized CGs, (b2) its bi-modal grain size distribution histogram, and (b3) its dispersive ε_y strain bands after 12.75% tensile loading. (c1) Recrystallized CG Cu, (c2) its bi-modal grain size distribution histogram, and (c3) its dispersive ε_y strain bands after 12.49% tensile loading.

5. Processing and properties of heterostructured (HS) materials

Various processing technologies have been reported for fabricating heterostructured materials. Some of them have been around for decades, developed for processing nanostructured metals. Most importantly, current industrial facilities can also be used to manufacture some types of heterostructured (HS) materials at large scale and low cost. This greatly helps with the commercialization of HS materials since scaling up new materials technologies for large industrial production at low cost has always been the biggest challenge for their wide commercial applications. The ease fabrication of HS materials and the new materials science associated with them have led to the fast development of this new materials field and some commercialization activities is already underway. In the following, we describe some of the technologies that have been used to fabricate HS materials.

5.1. Heterostrustured lamella (HL) materials

Heterostructured lamellar structure is so far the most effective heterostructure for producing HDI strengthening and HDI strain hardening [15]. This structure was reported originally in Ti processed by asymmetric rolling plus subsequent partial recrystallization annealing [2], which produced recrystallized soft lamellae with a volume fraction of 25 %, dispersed in the non-recrystallized but recovered nanostructured matrix (Fig. 29a-c). The initial raw Ti sample has an equiaxed grain structure with an average grain size of 43 μm. As shown in Fig. 29c, there is a huge difference in grain size between the soft lamellar and the matrix. The soft lamellae consist of micron-sized grains (MGs) of $\overline{d}$ of 2.3 μm and are dislocation free. The matrix was only subjected to the recovery process and therefore will contain dislocations albeit with a reduced dislocation density as compared with the as-rolled state. Fig. 29d shows a recrystallized Ti grain with many pile-ups of geometrically necessary dislocations (GNDs). As discussed earlier, the GND pile-ups will effectively produce hetero-deformation induced (HDI) stress.

Fig. 30a,b show the tensile mechanical behavior and properties of the HLS Ti, as compared with those of ultrafine grained and coarse-grained Ti [2]. Fig. 30b shows that the HL samples have yield strength-ductility (uniform elongation) combinations that are clearly out of the conventional trade-off region. This is especially true for the HL60 and HL 80 samples, which have strength nearly as high as the ultrafine grained sample, and ductility values even larger than that of the coarse-grained Ti. This totally avoided the strength-ductility trade-off, which has been considered impossible according to our textbook and literature knowledge.

The high strengths of the HL60 and HL80 HLS samples violate several known principles of conventional materials science. First, the

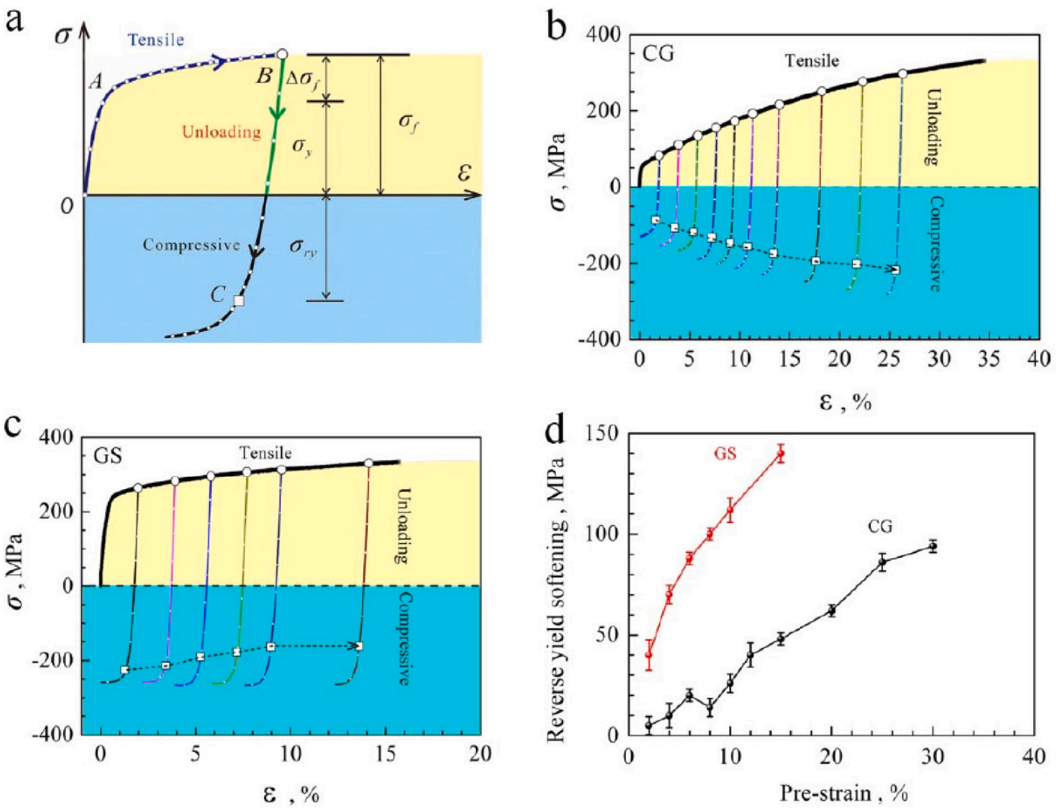

Fig. 28. (a) Schematic of the Bauschinger tensile-compressive tests, tensile curves and tensile-compressive curves for CG-Cu (b) and GS-Cu (c), and (d) reverse yield softening vs pre-strain.

partial recrystallization leads to the grain growth in 25 % of the sample volume, and this grain growth should consequently lead to lower yield strength, according to the well-known Hall-Petch relationship [54]. Second, the dislocation density in the recrystallized volume is reduced to almost zero and also significantly recovered in the un-recrystallized zones, which should also reduce the yield strength according to the Taylor equation [20–22]. Third, As shown in Fig. 30c, the HL60 sample has much higher strain hardening rate than both the ultrafine grained and coarse-grained sample, which violates the rule of mixtures. Coarse grained metals usually have high strain hardening rate because the large grains allow the effective accumulation of dislocations. In contrast, ultrafine grained metals have been found to have very low strain hardening rate because of their small grain sizes [57]. These expectations are clearly realized, as shown in Fig. 30c. HL samples have strain hardening rates that are higher than even the strain hardening of coarse-grained Ti, which is really unexpected and cannot be explained by conventional understanding of materials science, including the empirical rule of mixtures.

The superior mechanical properties of the HLS Ti are originated from the ultra-high hetero-deformation induced (HDI) strengthening and HDI strain hardening. As shown in Fig. 30d, the HDI stress is much higher than the stress produced by conventional dislocation hardening. Near the yield point, the HDI stress is as high as 400 MPa, which can be regarded as the increase of the yield strength caused by the HDI stress. After yielding, the HDI stress continues to increase to provide HDI hardening. Note that in conventional homogeneous metals, the HDI strengthening/strain hardening is usually lower than that of the dislocation strengthening/strain hardening, which is why the HDI stress is usually ignored in the literature when explaining the mechanical behavior/properties of homogenous materials. However, in the heterostructured materials such as the HL Ti, the HDI strengthening and strain hardening play a major or even dominant role in affecting the mechanical behaviors and in producing superior mechanical properties.

Ti has a hexagonal close-packed (hcp) crystal structure, which makes it easy for GNDs to pile up due to the difficulty of dislocation cross-slip. This is one of the reasons for hcp metals to have significant heterostructure effect, i.e., to develop high HDI stress.

The heterostructure effect is also found significant in face-centered cubic (fcc) metals, such as stainless steel [208], copper [251], Nickel [250], Mg alloy [252], medium/high entropy alloys [253–259]. For example, an HLS 316 stainless steel has been found to possess a very high yield strength of 1 GPa while retaining a good ductility of 9 % [208], as shown in Fig. 31. To process the HLS 316 stainless steel, a coarse-grained sample was cold rolled to a strain of 85 %, and then annealed at 750 °C for varying times to partially recrystallize the sample. As shown in Fig. 31c, the yield strength of HLS samples was increased by several times while their ductility was well retained.

The most versatile approach to make HLS materials is powder metallurgy, in which one can quantitatively control the volume fraction and morphology of the soft lamella. This approach has been demonstrated using Cu-Fe alloys [260]. Cu and Fe have very low

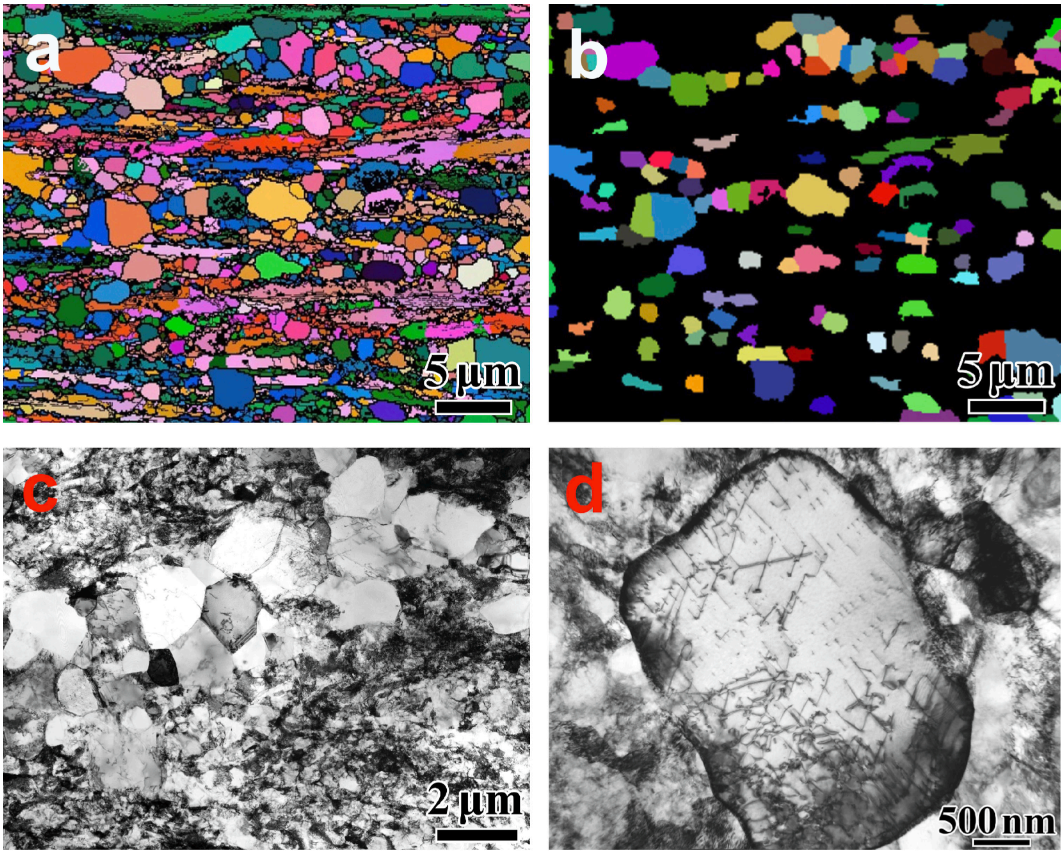

Fig. 29. Heterostructured lamella (HL) Ti produced by asymmetric rolling plus partial recrystallization [2]. (a) Electron back scattered diffraction (EBSD) image of the lamella Ti. (b) The EBSD image after blackening the un-recrystallized ultrafine-grained matrix. (c) Transmission electron microscopy (TEM) micrograph of a recrystallized soft lamellar and surrounding matrix. (d) Pile-ups of geometrically necessary dislocations in a recrystallized grain after tensile deformation for a strain of 2%.

mutual solubility and does not form intermetallic compounds, which makes them ideal for making soft Cu lamellae embedded in harder Fe matrix. The volume fraction of the soft lamellae can be controlled by the initial ratio of powder mixture while their length to thickness ratio can be controlled by the rolling strain after consolidation. The initial powder mixture can be from different metals and/or phases. It can also be a mixture of powders with the same composition but different grain sizes such as coarse-grained powder mixed with nanostructured powder.

The HL Cu-Fe samples were processed by mixing desired volume ratios of Cu powder and Fe powder, compacting them and then consolidating them at 1050 °C for 2 h, which were further cold rolled to a thickness reduction of 81 % and annealed at 360 °C for 30 min [260]. Fig. 32a shows the optical photograph of a heterostructure with soft Cu lamellae embedded in the hard Fe matrix. The volume fraction of the Cu lamella is 30 %. Each lamella was originated from an initial Cu particle. The elongated shape was produced by the cold rolling. Fig. 32b is an ion channelling contrast imaging (ICCM) micrograph, showing that the Fe matrix is coarse-grained while Cu is fine grained with a grain size of 1 μm. Fe precipitates were found in the Cu lamellae near the zone boundaries. Fig. 32c shows the microhardness difference in the soft Cu zones and hard Fe zones. Fig. 32d,e shows that the HLS Cu-Fe alloy has superior mechanical behavior and properties. As shown, the sample with 15 % of soft Cu lamella has both higher strength and higher ductility than the pure hard Fe sample that was subjected to the same thermomechanical processing, which is really surprising. This certainly cannot be explained by conventional empirical materials principles such as the rule of mixtures. The HL sample with 30 % vol. Cu lamellae exhibits the best yield strength-ductility combination. These superior mechanical properties were attributed to the effective heterostructure effect, i.e., the HDI strengthening and HDI work hardening, as shown in the Fig. 32f.

5.2. Gradient structured (GS) materials

The gradient structured (GS) materials refer to bulk materials with microstructural gradient(s) in one or more dimensions [185,261,262]. The microstructural gradient can be from grain size [23,24], twin density [25,233,234], a combination of grain size and twins [263], chemical concentration [264], density of nano-precipitates or fraction of constituent phases [265–267], etc.

Most gradient structured materials reported so far have been formed by grain-size gradient [23–25,53,185,187,265,268–275].

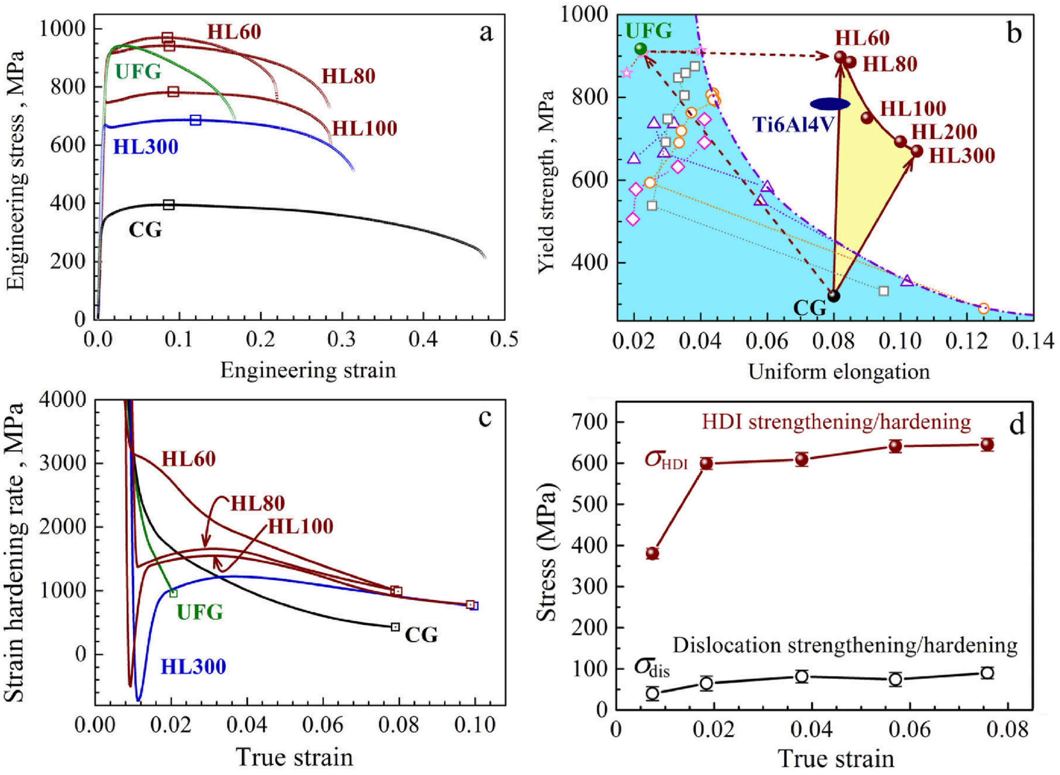

Fig. 30. The tensile mechanical behaviors and properties of the heterostructured lamella structured (HLS) Ti, as compared with those of ultrafine grained and coarse-grained Ti [2]. (a) The engineering stress–strain curves. (b) The HLS samples (HL60-HL300) break away from the conventional strength-ductility banana curve. (c) The corresponding true stress hardening($d\sigma_T/d\varepsilon_T$)-true strain (ε) curves before necking. (d) In the HLS Ti, the hetero-deformation induced (HDI) strengthening and HDI hardening are many times higher than those produced by dislocations.

Fig. 33 shows two types of samples with grain size gradient. Fig. 33a,b show a typical gradient sample consisting of a coarse-grained (CG) core sandwiched between two surface layers of either nano-grains or nanostructure, with a grain-size gradient in-between. Fig. 33c shows the schematic cross-section of a cylindrical gradient structured sample. Fig. 33d shows a schematic of a nano-structured surface layer below which is a grain-size gradient layer, which extends all the way the coarse-grained core. Fig. 33e is a typical grain size gradient in gradient structured interstitial-free steel [23].

As shown in Fig. 33e, in the gradient layer, the grain sizes can span 3–4 orders of magnitude from below 100 nm to a few tens of micrometers [23,24]. In the nanostructured layer, the yield strength can be several times higher than that of the CG layer, but the ductility shows the opposite trend, i.e., the trade-off between the strength and ductility [23,24]. This mechanical incompatibility will inevitably lead to heterogeneous deformation, which will stimulate new deformation physics [23,181].

The grain-size gradient samples are usually processed by surface mechanical attrition treatment (SMAT) [265], which involves repetitively impacting the sample surface with high speed balls. The SMAT process is in some way similar to the conventional shot peening, except that the balls are larger than the shots and velocity of the balls is higher than that in a normal shot peening. Consequently, a nanocrystalline layer on the surface can be produced, below which a grain-size gradient layer is generated. Several SMAT variants with similar processing principle have been reported, including rotational accelerated shot peening (RASP) [244,276,277], ultrasonic SMAT [278,279], severe shot peening (SSP) [280], etc. A related but different technique is surface mechanical grinding treatment (SMGT) [281–283], in which the severe plastic deformation of the surface layer is realized by the sliding of a hard ball/tip pressed against the surface. This technique can produce a smooth sample surface. Other deformation approaches to produce gradient structures include torsional straining [187,284–287], cyclic dynamic torsion[263], surface rotational rolling [288], rotary swaging[289–291], single-roll angular rolling [292], surface SPEC milling [293,294], surface mechanical rolling treatment [295], etc. As discussed later, the surface deformation approach often produces a residual stress in the sample, which may affect not only fatigue life but also the mechanical behavior of the sample.

A different approach for produce gradient structures include electro-deposition [25,233,269,296], and induction heating [297]. Note that the conventional industrial heat treatment techniques such as nitriding and cementing will produce a compositional gradient from the surface and may consequently produce a structural gradient during the subsequent thermal processing.

Lu et al [24] first demonstrated an extraordinary strength-ductility combination in gradient structured Cu. As shown in Fig. 34a, the yield strength of the gradient structured Cu doubles that of the CG Cu while its ductility is comparable to that of CG Cu. The high ductility is especially surprising and was attributed to the grain growth in the nanostructured Cu layer. Superior strength-ductility

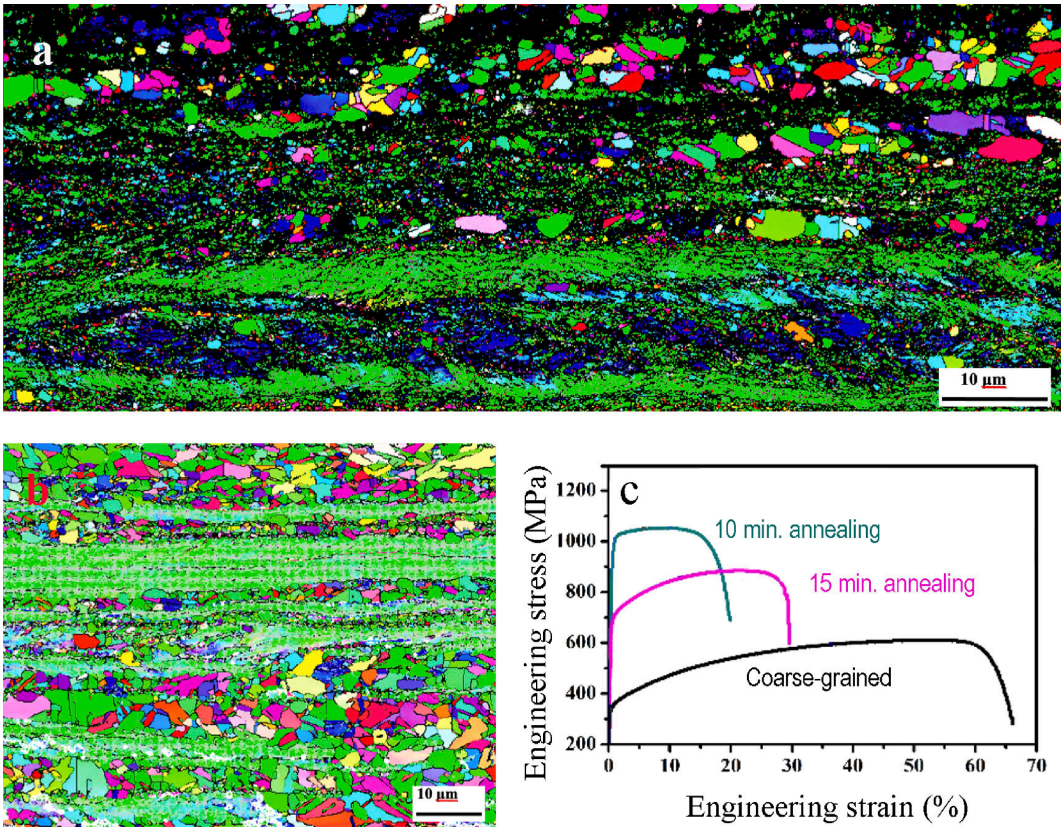

Fig. 31. Heterostructured lamella structured (HLS) 316 stainless steel processed by cold rolling for 85 % followed by annealing at 750 °C [250]. (a) EBSD micrograph of the sample annealed for 10 min. (b) EBSD micrograph of the sample annealed for 15 min. (c) The engineering stress–strain curves of the HLS samples annealed for 10 and 15 min and the coarse-grained as-received sample.

combinations have been also reported in various gradient structured metals and alloys even without grain growth. Examples include gradient structured interstitial-free (IF) steel (Fig. 34b) [23], Ni [269], TWIP steel (Fig. 34c) [187], and copper [298]. Recently, a gradient structured copper was synthesized with both grain size and twin spacing gradients [25] using electrodeposition, which exhibited both increased ductility over grain-size gradient Cu and enhanced yield strength (Fig. 34d). Higher ductility was observed when TRIP [275] or TWIP effect [53,268,270] occurred in the gradient structure.

The high ductility is attributed to high strain hardening in the gradient structured materials [15,23]. Several mechanisms for enhanced strain hardening were proposed. The first is the mechanically-driven grain growth in the NG layers during tensile testing [24,274]. Grain growth indeed can recover some strain hardening capability in the nanostructured layer, as recently demonstrated in gradient structured interstitial-free steel [17]. This recovers some capability of forest hardening in the NG layers [24]. However, this recovery is not enough to sustain uniform elongation without necking, which is why nanostructured metals usually have low ductility.

The second mechanism is hetero-deformation induced (HDI) strain hardening [1,15,16,181]. There is a plastic incompatibility upon straining between different layers and inside the gradient layer. Strain gradient appears where the geometrically necessary dislocations (GNDs) are produced to help to coordinate plastic deformation at hetero-boundaries. These GNDs pile up and accumulate near hetero-boundaries to induce HDI strengthening and HDI strain hardening [1,181]. HDI hardening is evidenced by hysteresis loops [23] and HDI stress (previously termed as back stress) [19,181] during unloading–reloading testing.

For samples processed by the surface plastic deformation techniques, residual stress is the third major contributor to the extra strain hardening in gradient structured materials [299]. Surface deformation usually produces significant compressive residual stress under the sample surface. Fig. 35 shows the *in-situ* synchrotron measurement results of an interstitial-free (IF) steel during a tensile test. Fig. 35a shows the residual stress profile along the depth of the gradient sample. As shown, the compressive stress layer is about 150 µm below the surface. It is this compressive stress layer that sustained the highest applied tensile stress during the tensile test, which contributes to strain hardening during the tensile straining (Fig. 35b). In addition, the compressive residual stress in this layer offsets the applied tensile stress during the tensile straining, and therefore started plastic deformation (yield) later than the layers on both sides, creating two plastic-elastic boundaries (Fig. 35c). GNDs in the plastically deforming layers pile up and accumulate near the zone boundaries, which effectively produces HDI strengthening and HDI strain hardening. Fig. 35d shows that the dislocation density accumulation is indeed highest outside of the compressive stress layer and near the interfaces. In addition, these two elastic–plastic interfaces migrate toward the center of the compressive layer with applied tensile strain, creating a trail of high-density dislocations in

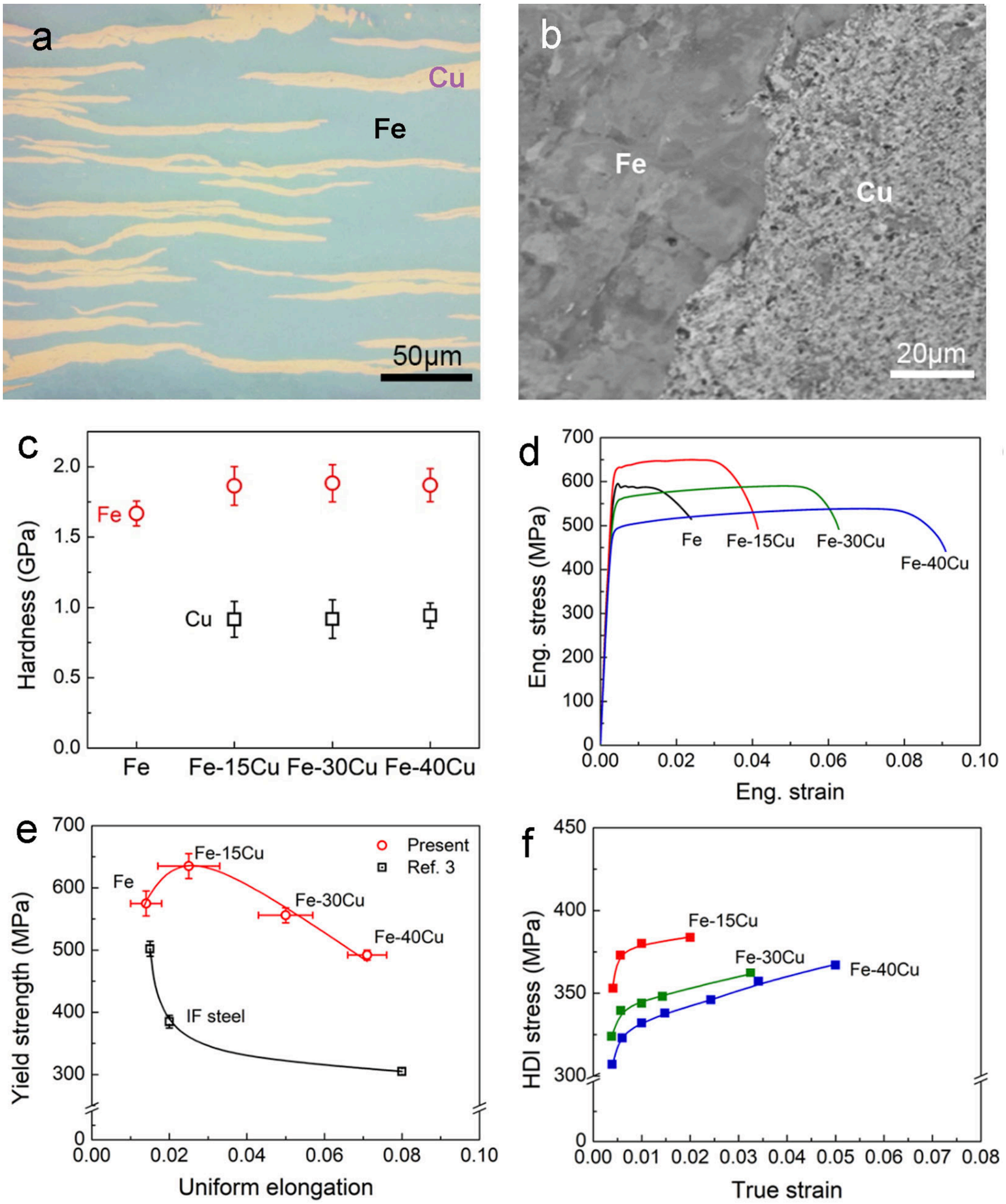

Fig. 32. Heterostructured lamella structured (HLS) Cu-Fe alloy [260]. (a) Optical photograph showing soft Cu lamellae (30% vol.) embedded in hard Fe matrix. (b) Ion channelling contrast imaging (ICCM) micrograph of Cu and Fe zones. (c) The microhardness difference in the soft Cu zones and hard Fe zones. (d) The tensile engineering stress–strain curves of the HL Cu-Fe alloy with varying soft Cu lamella volume fraction. (e) The yield strength-ductility combination as a function of the volume fraction of Cu lamellae. (f) The effect of the volume fraction of the Cu lamella on the hetero-deformation induced stress.

their wakes. These dislocations include the GNDs as well as statistical dislocations, both of which help to produce strain hardening.

The fourth contributor to the HDI strengthening and HDI strain hardening is the global mutual constraint between the gradient layers and soft CG central layer. As illustrated in Fig. 10, the mechanical incompatibility and the global mutual constraints will convert the uniaxial applied stress into multiaxial stresses, which could help to activate more slip systems and promote interactions among dislocations from different slip systems [23]. This will consequently lead to higher strain hardening. To verify this hypothesis, gradient Cu samples with double-sided constraint and single-sided constraint but the same volume fraction of CG layer fraction (see Fig. 36) were processed and tested [300]. It was found that the double-sided constraint yielded higher strength and higher ductility. It follows that the volume fraction of the CG layer should also affect the intensity of the global constraint. Consequently, an optimal volume

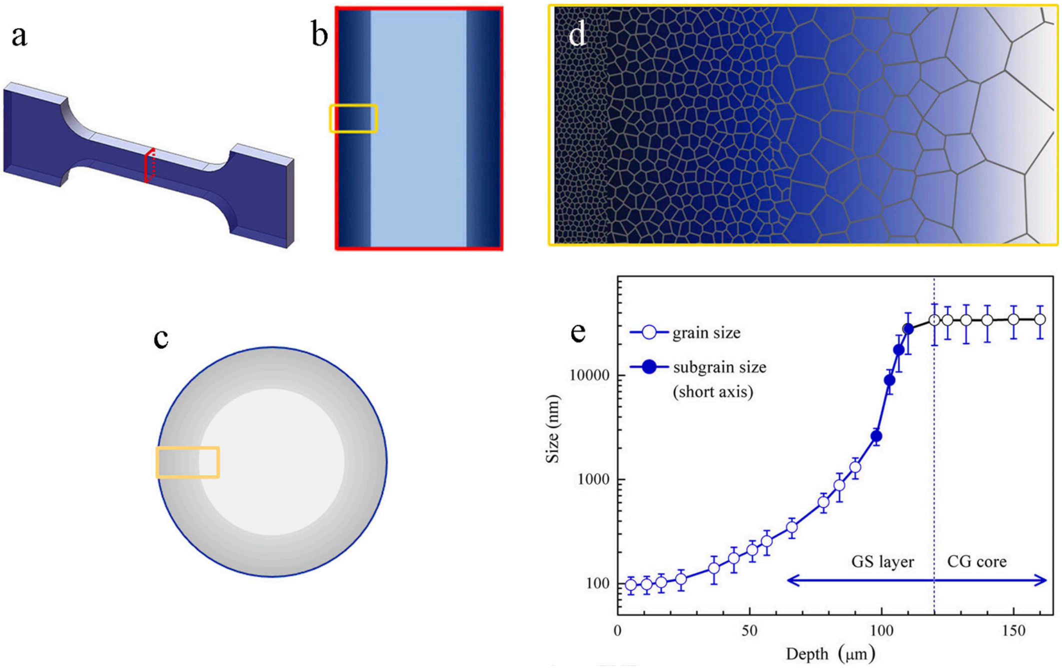

Fig. 33. Schematics of gradient structured samples. (a) Schematic of a gradient structured plate sample. (b) The cross-section of the plate sample with two nanostructured and gradient layers sandwiching a coarse-grained layer. (c) The schematics of the cross-section of a cylindrical gradient structured sample. (d) Schematic of a nanostructured surface layer on top of a grain-size gradient layer. (e) A typical grain size gradient in gradient structured interstitial-free steel [23].

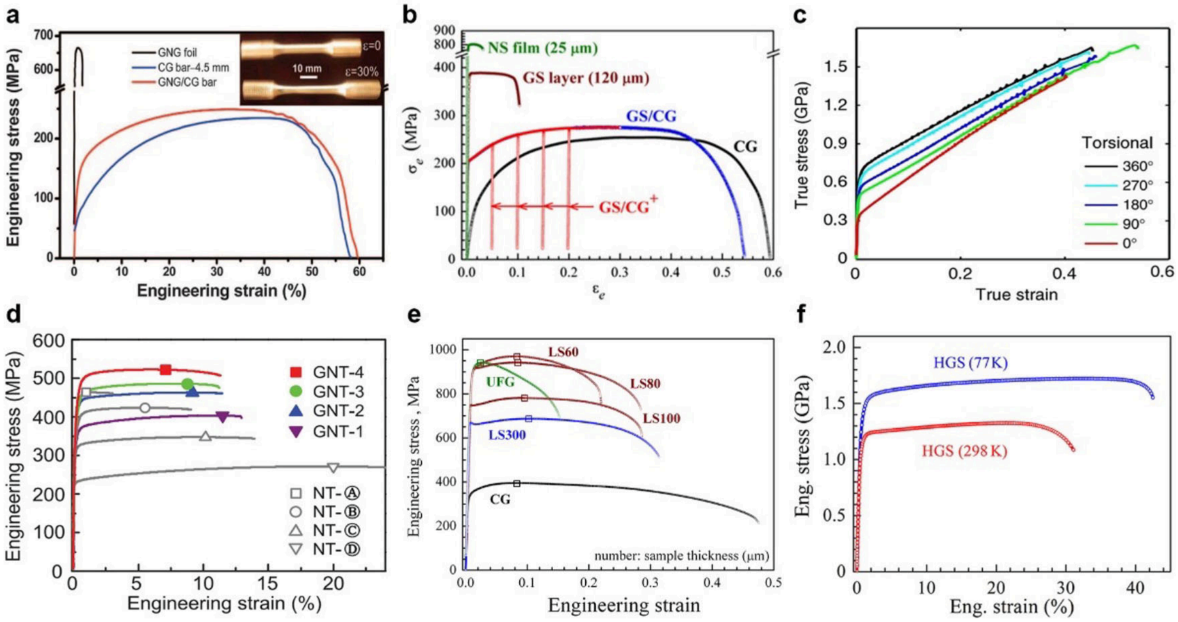

Fig. 34. Tensile stress–strain curves in various heterogeneous structures. (a) GS Cu [24]. (b) GS IF steel [23]. (c) GS TWIP steel [187]. (d) GNT Cu [25]. (e) LS Ti [398]. (f) HS CoCrNi MEA [189]. GS: gradient structure. LS: lamellar structure. NG: nanograin. CG: coarse grain. NS: nanostructure. GNG: gradient nanograin. GNT: gradient nanotwin. NT: nanotwin. HGS: heterogeneous grain structure.

fraction for the CG layer should exist. This was indeed found true in gradient structured Cu [301].

Recently, it was found that gradient nanotwinned metals with twin thickness gradient developed significant extra strengthening as compared with the samples with homogeneous twin thickness [233,234], which was attributed to the strain gradient developed

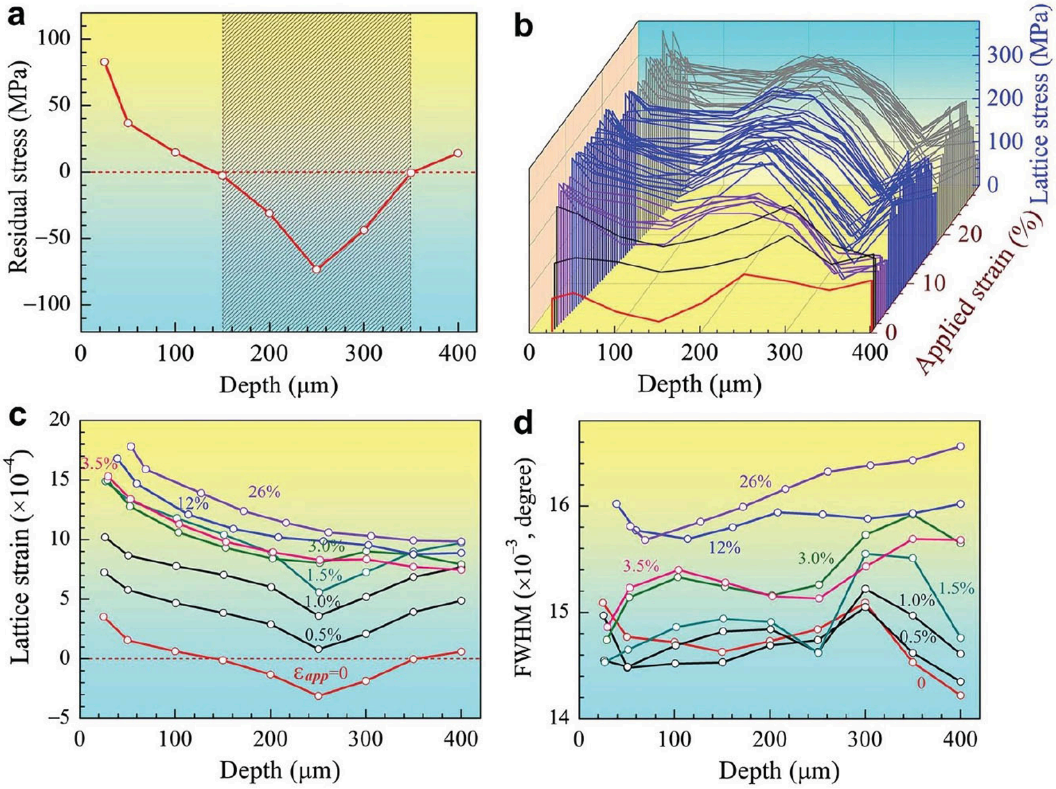

Fig. 35. Experimental results by *in-situ* XRD synchrotron during a tensile test [299]. (a) Residual stress distribution below the surface prior to tensile loading. (b) The evolution of axial lattice strain along the depth at varying applied tensile strain. (c) The evolution of axial stress (strain) along the depth. (d) The full width at half maximum (FWHM) of diffraction peaks (representing dislocation density) along the depth with applied strain.

between different twin layers. The strain gradient needs to be accommodated by GNDs, which produce back stress in the soft layers with larger twin thickness to strengthen the material. In addition, the combined experimental study and modelling reveals that the higher structural gradient led to higher extra strengthening. These observations provide strong support to the general principle of heterostructured materials as discussed in Section 4.3. However, this GND arrangements observed here are different from the ideal GND pile-up model shown in Fig. 11. This suggests that GND arrangements can be very versatile in different microstructures and metals with different intrinsic properties such as stacking fault energy, as discussed in Section 4.5.

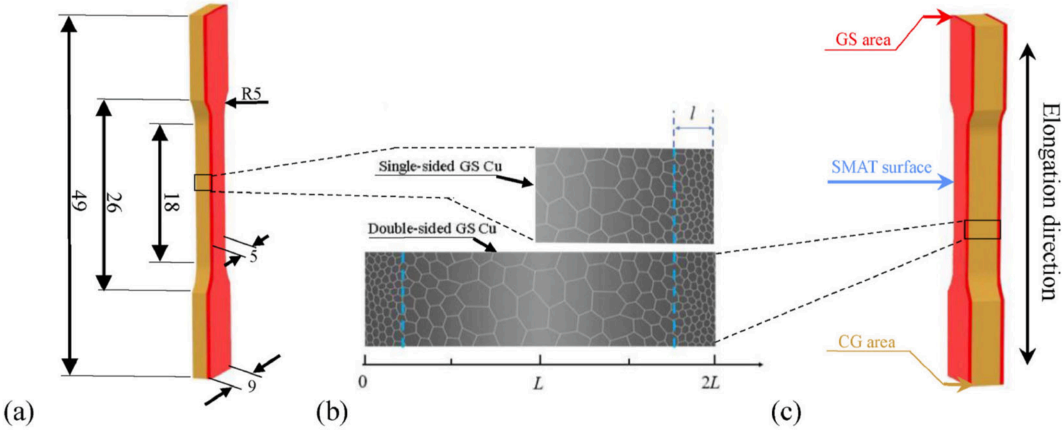

Fig. 36. (a) The geometry and size of a tensile sample with the single-sided gradient structure. (b) Schematic illustration of the single-sided GS and the double-sided GS the samples processed by SMAT. (c) The geometry of the double-sided GS sample [300].

5.3. Layer structured (LS) materials

Layer structured materials can be regarded as composites consisting of multiple 2D layers of different phases/metals [15]. They are also called laminate-structured metals earlier, but this sometimes may be confused with heterogeneous lamella structured metals. The difference is that the layer structured metals consist of continuous 2D layers, while the lamellae in the heterogeneous lamella structured metals is not continuous. Early studies of layer-structured metals primarily focused on thin foils of a few micrometers in thickness synthesized by various thin film techniques including electrodeposition [302,303], evaporation, sputtering [304–308], molecular beam epitaxy [309,310], etc. Very high strength is usually observed in these studies, especially when each layer is very thin (<500 nm) [311–315]. Their strength follows the Hall-Petch relationship with the layer thickness [311,314–317]. This is not surprising because grains often span the entire layer thickness [15]. These samples might be good for fundamental study but are too thin and small for practical structural applications.

A severe plastic deformation technique, accumulative roll bonding (ARB) (Fig. 37), which was developed for processing ultrafine-grained materials [318–321], has been used to process layer structured materials recently [27]. ARB is a technology that can be used to process sheet samples that are large enough for practical industrial applications [312]. Surprisingly, ARB can not only fabricate large layer-structured materials, but also very thin layered samples with interfaces similar to what is produced by deposition methods when the layers become very thin, e.g. in the Zr/Nb and Cu/Nb systems [29,322]. ARB has been reported to manufacture the following layer structured material systems Ag/Fe, Ag/Ni, Cu/Nb, Cu/Ta, Zr/Nb, as well as Mg-alloy/Nb and Cu-bronze (Cu-10 % Zn) [27,320,323–327].

Layer-structured materials is not the best in mechanical properties as compared with other heterostructured materials [1,2]. However, they are one of the best for fundamental studies [2,13,240], because they can be fabricated to have clear and controllable inter-zone (phase) interfaces. For example, Cu-bronze layered structure processed by ARB was used to study the effect of interface spacing on the mechanical properties [27]. Fig. 38a-c shows the optical micrographs of Cu-bronze layered structure processed by ARB for 2, 3 and 5 passes followed by annealing, denoted as N2, N3 and N5, respectively. Their microstructures are shown in Fig. 38d-f, which reveals ultrafine-grained (UFG) bronze layer and coarse-grained Cu layer. Annealing twins can be observed in the Cu layer. The strength of the UFG bronze layer is over 100 % higher than that in the coarse-grained layer (Fig. 19b) [13], which indicates a significant mechanical incompatibility during tensile deformation.

Fig. 38g shows tensile stress–strain curves of these three samples. As shown, with decreasing interface spacing, i.e., smaller layer thickness, both yield strength and ductility increased. Fig. 38h further shows that both the ultimate strength and ductility increased with decreasing layer thickness (increasing interface density). These results indicate the important role played by interfaces on the mechanical properties. It was found that the geometrically necessary dislocations (GNDs) piled up and accumulated near the interfaces to produce back stress in the soft Cu layers and forward stress in the hard bronze layers to produce extra HDI strain hardening [27,181], which acted to increase the yield strength and ductility. It is noted that in Fig. 38, the samples with the thinnest layer had a layer thickness of 31 μm. The effect of layer thickness (interface density) on the mechanical behavior was further studied to include samples with layer thickness smaller than 31 μm [13].

Fig. 39 shows the effect of layer thickness (interlayer spacing) on the mechanical behavior [13]. From the true stress–strain curves (Fig. 39a), it can be seen that both the yield strength and the strain hardening increased with decreasing layer thickness. Fig. 39b shows that the ductility (uniform elongation) first increased with decreasing layer thickness, reached maximum ductility at the layer thickness of about 15 μm, and then started to decrease, demonstrating that there is an optimum layer thickness for the best combination of strength and ductility. This is the thickness at which the hetero-boundary affected regions (HBARs) start to overlap with each other [13]. The HDI hardening was found significant in the layer structured Cu-bronze sample (Fig. 39c), and was believed responsible for the observed initial simultaneous increase of yield strength and ductility [13,27]. As shown, the HDI hardening is much higher than the dislocation induced hardening. Fig. 39d shows that the layer-structured sample has superior combination of strength and ductility over the homogeneous samples [13], which was also attributed to the HDI hardening [13,27].

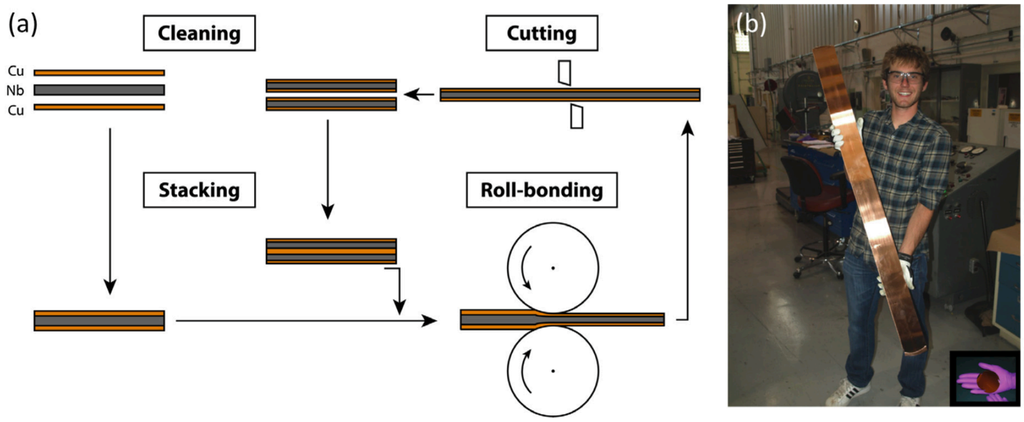

Fig. 37. (a) Schematic of accumulative roll bonding. (b) Large ARB-processed Cu-Nb layer-structured workpiece held by a graduate student [312].

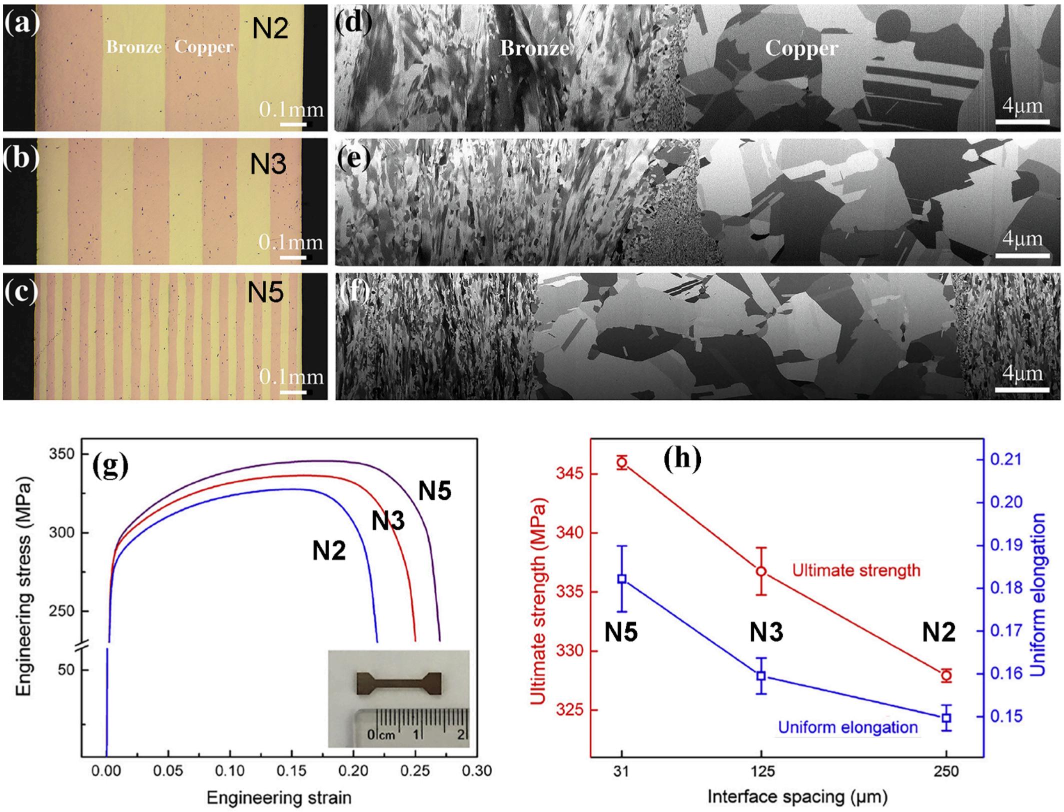

Fig. 38. Optical micrograph of Cu-bronze (10 %Zn) samples processed using ARB for (a) 2 passes (N2), (b) 3 passes (N3), and (c) passes (N5). Their microstructures from ion channelling contrast microscopy are shown in (d) to (f), respectively. (g) The tensile stress–strain curves. (h) Increase of both ultimate strength and ductility with decreasing layer thickness.

5.4. Multi-modal structured (BMS) materials

One of the earliest reported observations on the superior mechanical properties of heterostructured materials is on bi-modal nanostructured Al alloy by Lavernia's group [169]. In this study, 5083 Al alloy powder produced by spray-atomization was cryomilled in liquid nitrogen, followed by degassing, hot isostatic pressing and hot extrusion. A bi-modal microstructure was observed in which coarse grains were embedded in nanostructured matrix. Superior combination of a yield strength of 334 MPa and elongation to failure of 8.4 % was obtained (see Fig. 40a). Importantly, good strain hardening was observed despite of its small average grain sizes (34 nm) as measured by X-ray diffraction.

High density of dislocation structure was observed in the CG grain (see Fig. 40b) [15,328], which was believed responsible for the high strain hardening and good ductility. It was hypothesized that the dislocations were piled up in the coarse grains against its boundaries with the nanostructured zone, as shown in Fig. 40c. This not only increases the dislocation density to produce dislocation hardening according to the Ashy equation [20], but also the HDI strain hardening [1,15,181], which collectively produced the observed good strain hardening for good ductility. In addition, it is also believed that the coarse grain can act to blunt cracks from the nanostructured zone.

Another well-known work on bi-modal structured materials was reported on Cu, which was processed by cryogenic rolling followed by annealing [49]. The bi-modal structure consists of ~ 25 vol% of coarse-grained (1–3 μm) embedded in ultrafine-grained matrix (<200 nm). The coarse grains are equiaxed with some annealing twins. A superior combination of strength and ductility (uniform elongation) was observed. Its high strength was attributed to the fine grain sizes while the high ductility was attributed to high strain hardening rate, which was believed enabled by several factors including triaxial-stress state in the confined coarse grains, high-density of geometrically necessary dislocations (GNDs), twinning, and strain partitioning with the soft coarse-grains carrying higher plastic strains. However, the concepts of back stress and HDI strain hardening were not raised in this paper. Nevertheless, the concept of GNDs and strain partitioning mentioned in this paper represented the most advanced understanding of the mechanisms of high ductility in bi-modal structured materials at the time when this paper was published.

After these early reports [49,169], many follow-on researches were performed on bi-modal metals with limited successes in improving the strength and ductility [34,35,50,51,183,184,329–336]. The lack of good understanding of the mechanism for the high strength and strain hardening hindered the development of bimodal metals and alloys. As a result, most studies are based on the trial-and-error approach instead of being guided by physics-based understanding. As we learned later, a few critical heterostructural

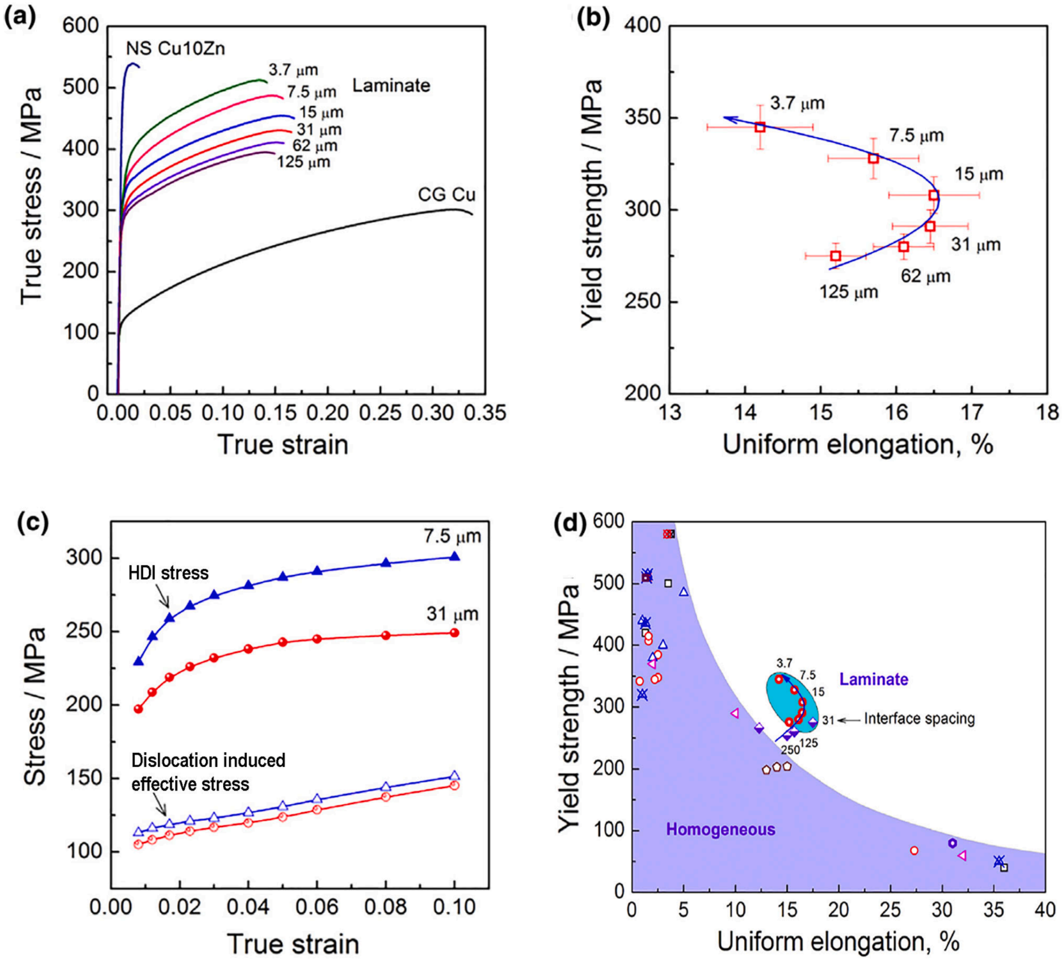

Fig. 39. The effect of layer thickness on the mechanical behaviour and properties of Cu-bronze (10 %Zn) layer-structured samples [13]. (a) True stress–strain curves, the numbers near the curves are layer thickness/interlayer spacing. (b) Yield strength vs ductility (uniform elongation) with decreasing layer thickness indicates an optimum layer thickness for the best combination of strength and ductility. (c) Evolution of HDI stresses and dislocation hardening stresses with applied strain. (d) Comparison of strength and ductility (uniform elongation) between the layer-structured CG–Cu/NS–bronze samples and the conventional homogenous materials.

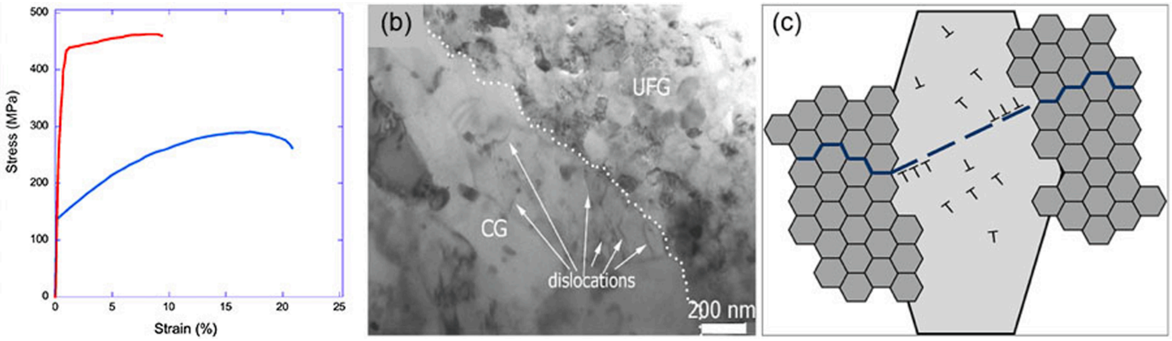

Fig. 40. Bi-modal structured 5083 Al alloy with superior combination of strength and ductility. (a) Tensile properties of bimodal structured 5083Al alloy [399], (b) High-density dislocation in a coarse grain [328], (c) Schematic of dislocation piling up against coarse-nano zone interface, and crack blunting by the CG grain.

features are essential for producing high strength and high HDI strain hardening [1,181], including embedding the soft zone in the hard matrix, high density of zone boundaries, and appropriate zone boundary spacing. The bimodal structures reported in the literature were not purposely designed with these factors in consideration.

In addition to bimodal structured material, multimodal structured materials were also reported [164,337–341]. These materials were reported to have superior combinations of strength and ductility. The mechanisms for their superior mechanical properties are similar to heterostructured materials including bi-modal structured materials. The benefit of multimodal structure is that if the deformation heterogeneities were initiated at different stress and plastic strain levels, the strain hardening is expected to last for a longer plastic strain, and consequently produces better ductility.

5.5. *Harmonic structured materials*

Harmonic structure was defined by Ameyama as consisting of coarse-grained cores embedded in three-dimensional UFG networks [342]. The processing of harmonic structures can be clearly described by Fig. 41 [343]. As shown, the process starts with spherical initial coarse-grained particles, which are milled using low energy so that only the particle surfaces are deformed plastically to produce an ultrafine grained surface layer. The low energy milling was carried out either in a planetary ball mill [194,336,342,344–346] or a high-pressure gas jet mill [343]. The as-milled powder is then consolidated into bulk harmonic structured materials. It is noted that the fast diffusion rate of the UFG surface layer should help the consolidation process, making it easier to consolidate the powder. The UFG surface layers of the power particles are transformed into the UFG networks and the coarse-grained cores after the consolidation, as schematically illustrated in Fig. 41.

A number of research papers have been published in the area of harmonic structured materials in recent years [33,36,37,336,342–354]. As an example [33], pure Cu (99.96 % purity) with an average particle size of 160 μm was mechanically milled in a planetary mill in Ar gas, producing particles with deformed UFG surface layers. The milling is a critical step in making harmonic structured materials. The thickness of the UFG layer can be controlled by varying the milling duration as well as other milling parameters. The energy of the milling for each impact between the balls and the particle should be low so that the powder particles are only deformed in their surface layers and remains spherical (see Fig. 42).

The as-milled powder was sintered using spark plasma sintering (SPS) at 600 °C under 100 MPa pressure for 1 h to produce sintered samples with a diameter of 15 mm and thickness of 4 mm. Fig. 43a shows a typical harmonic structure after sintering, which has a 36 % vol. of the shell structure. It is noted that nanostructured surface layers of the particles facilitate the consolidation because of the faster diffusion kinetics of the nanostructures. The mechanical behaviours of the samples with varying harmonic structures are compared in Fig. 43b, which reveals that with increasing volume fraction of the shell structure, both the yield strength and ductility increased. This demonstrates the advantage of the harmonic structure [33].

This superior combination of mechanical properties is believed produced by the HDI strengthening and HDI strain hardening because the harmonic structure is a type of heterostructure [15]. It should be noted that the improvement in the yield strength in Fig. 43b is not dramatic, suggesting a weak HDI strengthening. It is reasoned that if the density of the zone interfaces is increased, the HDI strengthening and HDI strain hardening will become stronger to yield even better mechanical properties. This can be easily done by elongating the spherical soft core and hard-shell structure by cold deformation such as rolling. This effect was indeed observed.

The harmonic structure can be an ideal structure for studying the fundamentals of heterostructured materials, because the heterostructural parameters such as the volume fractions, shape and sizes of the soft zones can be well controlled using the processes of low energy milling and consolidation. Further investigation is needed to investigate this type of heterostructures.

5.6. *Dual-phase structured materials*

Dual-phase structured materials are a class of materials consisting of two-phases with different crystal structures or compositions

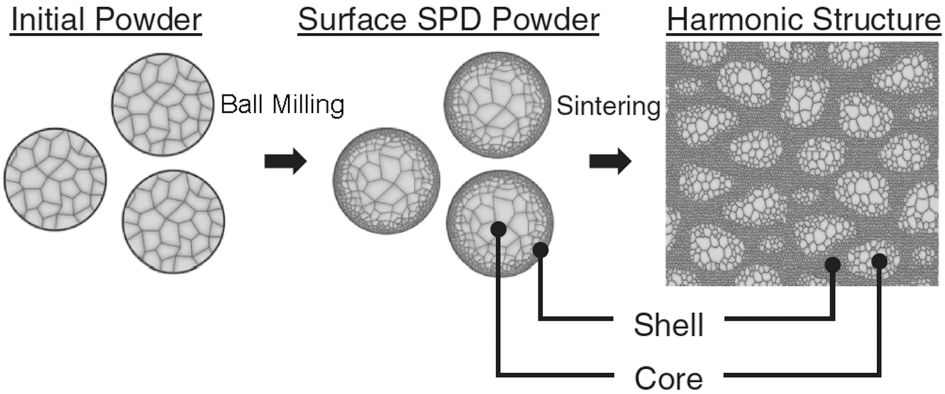

Fig. 41. Schematics of the processing steps for producing harmonic structured materials [343].

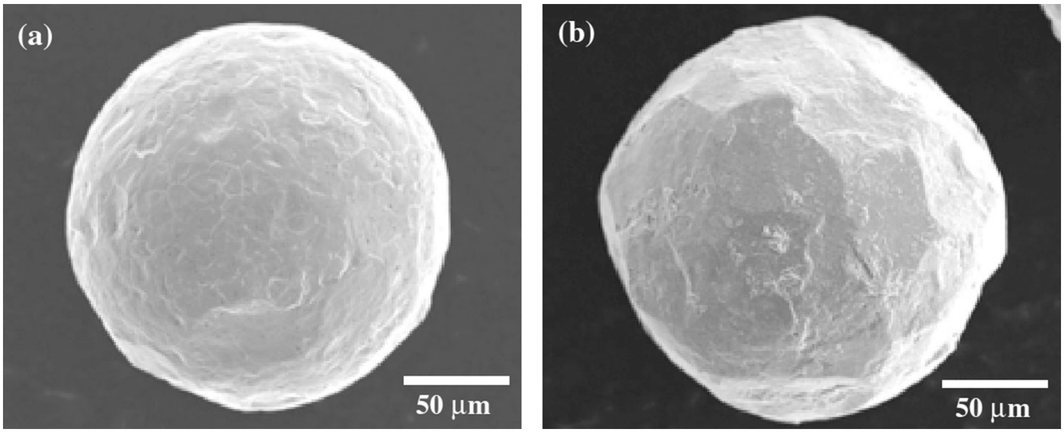

Fig. 42. (a) The image of an initial spherical Cu powder particle. (b) An Cu powder particle after low energy milling [33].

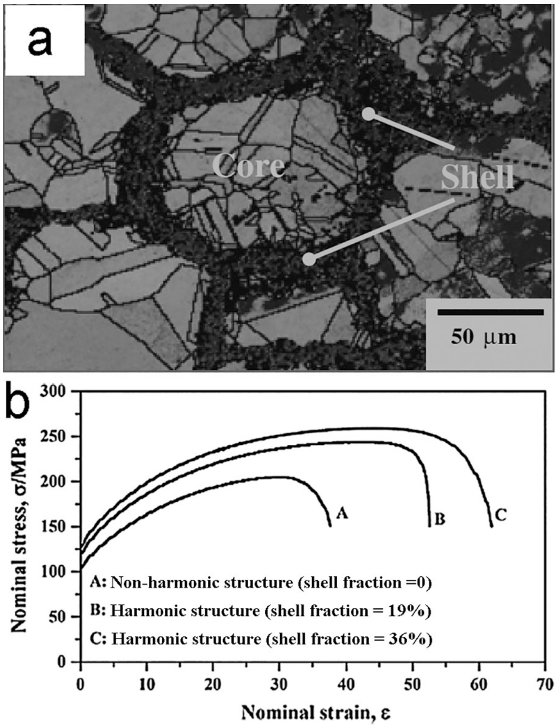

Fig. 43. (a) A typical harmonic structure of copper produced by SPS consolidation of Cu powder milled under low energy. (b) Comparison of mechanical behaviours of the samples with varying volume fraction of the hard shell structure [33].

[15,355]. For example, conventional eutectic or eutectoid (e.g., pearlite) structures are typical dual-phase structures with different crystal structures. Spinodal decomposition structure is a typical dual-phase structure with different composition but the same crystal structure. A popular class of materials developed using the dual-phase concept are dual-phase steels [15,38–40,356], which have been developed for the automobile applications [188,357]. The most popular dual-phase steels reported in the literature are martensite-ferrite dual phase steel [39,41,44,188,195,355,358–363], although other dual phase steels and alloys have also been reported [268,364–366].

The advantage of the martensite-ferrite dual phase steels is that the volume fraction of the martensite phase can be easily controlled by adjusting the austenitization temperature in the ferrite–austenite two-phase zone of the phase diagram, which determines the ratio of the austenite to ferrite. The austenite will be transformed to form martensite during the subsequent quenching. In practice, the volume fraction of martensite is typically in the range of 3–30 % [40,188], although higher martensite volume fractions were also reported in the literature [363,367,368]. Due to the low volume fraction of martensite phase, the martensite zones are typically embedded in the soft ferrite matrix as hard islands.

The mechanical properties of dual phase steels typically have low yield strength and high strain hardening rate, high ultimate strength, high ductility and bake hardening at the paint baking temperature (∼170 °C) [188]. Another major advantage of the dual-phase steels is their good formability [15,357,369]. Low carbon dual phase steels also have good weldability. These properties render dual-phase steels superior properties and low cost, making them ideal for automobile applications [43,355].

The most salient feature of the mechanical behaviors of dual-phase steels is their high apparent strain hardening rate, which consequently leads to higher ductility [190,200,358,370]. The superior mechanical properties were attributed to strain partitioning in dual phase steel, where the soft phase carries higher plastic strain than the hard phase [188,190,195,199,200,365]. However, it was not clear why strain partitioning would produce higher strain hardening rate. Recently, we proposed that dual phase steels are a class of heterostructured materials, which consequently have strong HDI strain hardening to contribute to the observed high strain hardening [1,181]. The HDI strain hardening arises from the mechanical incompatibility of the two phases, which caused strain partitioning. Since the strain needs to be continuous across the interfaces, strain gradient will develop near the interfaces, which is accommodated by GNDs. The accumulation of GNDs will cause the HDI stress increase and consequently produce HDI hardening. High HDI hardening was indeed observed in a dual phase steel [364]. The HDI hardening is superimposed on the conventional dislocation hardening to produce the observed high strain hardening.

The principle in heterostructured materials can also be used to process dual phase steels to produce nanostructures. As discussed earlier, to produce high HDI hardening for superior mechanical properties, it is desired to have high flow stress difference between heterostructured zones, i.e., the phases in dual phase steels. Recently, we have demonstrated that it is also possible to use the heterostructures to process nanomaterial [371]. However, in this case, the flow stress difference between the two phases needs to be optimized to facilitate the deformation of the hard phase. In this work [371], a low carbon steel containing (wt%) 0.19C-1.01Mn-1.4Si Mn was austentized at 950 °C followed by water quench to produce a fibrous dual phase structure in which elongated martensite zones are embedded in the ferrite matrix, as shown in Fig. 44a. Counterintuitively, warm rolling at 300 °C produced a much finer lamella structure with an average thickness of 17.8 nm (Fig. 44b) than cold rolling at room temperature (54.6 nm, Fig. 44c).

At room temperature, due to the huge difference in flow stress, cold rolling often fragments the hard martensite zones instead of forcing them to co-elongate with the ferrite zones because the ferrite zones are too soft to transfer uniform stress on to the neighboring martensite zones. As a result, ferrite zones will sustain much higher plastic strain, producing a strong strain partitioning. The lower plastic strain sustained by the martensite phase makes it difficult to refine the martensite. In addition, localized strain bands are known to be active in such heterostructured materials [13,17,198,242,250], which might be responsible for the observed fracturing of the martensite zones. In contrast, at 300 °C the martensite is softened, while the ferrite is strengthened due to the diffusion of C from the martensite to ferrite, which makes them more compatible for co-deformation together during the warm rolling [371]. In addition, C atoms are found to be segregated to the martensite-ferrite interfaces to stabilize the lamellar structure. It appears that 300 °C provides

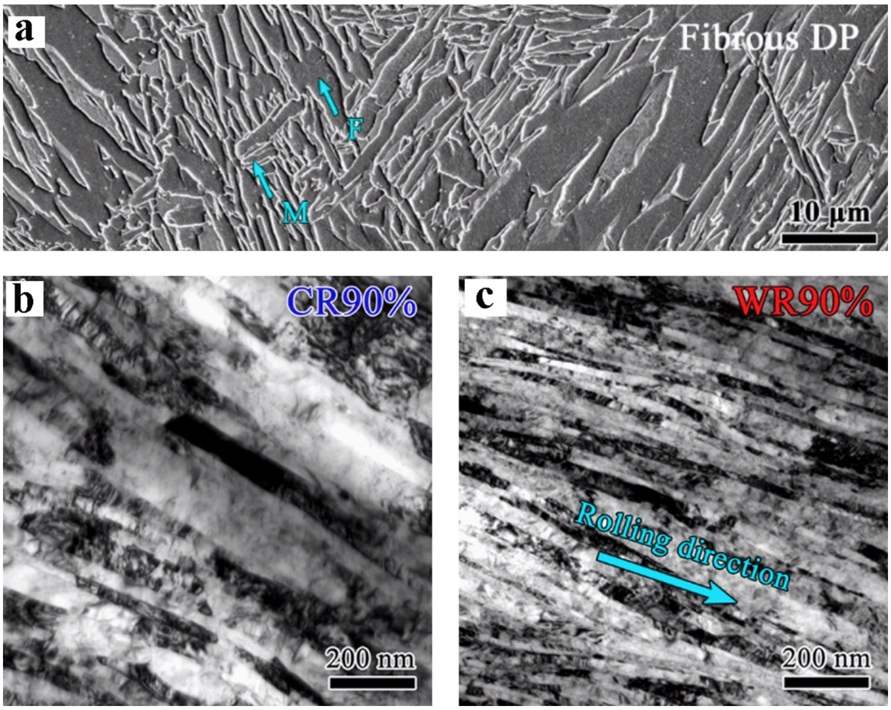

Fig. 44. (a) SEM image of martensite-ferrite dual phases in a low carbon steel after quenching from the austenite-ferrite two-phase region of the phase diagram. (b) TEM image after cold rolling the as-quenched sample for 90 % thickness reduction. (c) TEM image after warm rolling the as-quenched sample for 90 % thickness reduction at 300 °C.

the optimum compatibility for structure refinement in this low carbon steel. The very fine lamellar structure makes the nanostructured dual-phase steel stronger even than its martensite, which demonstrates the potential using the heterostructure concept to produce ultra-strong steels. This approach reported here should be applicable to all low carbon steels.

5.7. Heterostructured functional materials

The concept of heterostructured materials can also be applied to functional materials, where the trade-off of essential functional properties may also exist [15,372]. Functional materials that may benefit from the heterostructured concept include magnetic materials [373–375], thermoelectric materials [376], ferroelectric materials [377], etc. Here we will use the heterostructured magnet as an example to demonstrate the advantage of heterostructured functional materials. As deliberated below, many types of heterostructures for the structural materials can also be applied to the functional materials such as magnets.

Saturation magnetization (M_s) and coercivity (H_c) are crucial properties of permanent-magnet materials [378]. Obtaining a large energy density for a permanent magnet requires both high M_s and high coercivity H_c. However, like the strength-ductility trade-off in metals, a gain in M_s is inevitably accompanied by a loss in H_c, which limits the maximum energy density that can be achieved for permanent magnetic materials [372].

A research group at Yanshan University has recently made a pioneering study to produce a superior combination of the magnetization-coercivity by engineering heterogeneous and ordered nanostructures in a hybrid material that consists of hard and soft magnetic grains [374,375,379–381]. The hard magnetic grains have a large H_c and the soft magnetic grains have a high M_s. Such a new conceptual strategy exploits the benefits of both the heterogeneous or ordered nanostructure and the hybrid material, which opened up a new research area of permanent-magnetic materials. To date, several structural designs have been successfully explored to build high-performance permanent magnetic materials, including bimorphological [374,375], layered [379], core/shell [380] and gradient [381] nanostructures. These seemingly different strategies share a common design principle: the designed structural heterogeneities or ordered structures lead to large H_c while maintaining high M_s provided by the hybrid materials, since these structures themselves have important impacts on the magnetization reversal of ferromagnets. As such, the heterostructured magnets with heterogeneous or ordered nanostructures exhibit a superior magnetization-coercivity combination, thus yielding record-high energy densities (i.e., energy product) achieved so far with low rare-earth metal contents, for example, 28–31 MGOe for bulk anisotropic nanocomposite magnets [374,379] and 26 MGOe for isotropic permanent magnets [381].

5.7.1. Magnets with bimorphological oriented nanostructures

Li and co-workers proposed a design concept of bimorphological oriented nanostructures. The engineered heterogeneous nanostructure comprises aligned hard-magnetic SmCo rod-shaped grains, ~10 nm in diameter and 20–40 nm in length, and soft-magnetic α − Fe(Co) equiaxed grains with a high fraction (~28 wt%) and small size (~10 nm) (see Fig. 45) [374]. Such nanostructures were fabricated by multistep deformation. First, the morphology and structure of Fe(Co) nanocrystals were well controlled through purposely dispersing them in a SmCo-based amorphous matrix with ball milling. Then, the mixture was consolidated into bulk materials and deformed under high-pressure thermal compression (HPTC). The strain energy anisotropy of SmCo crystals yielded at high stress

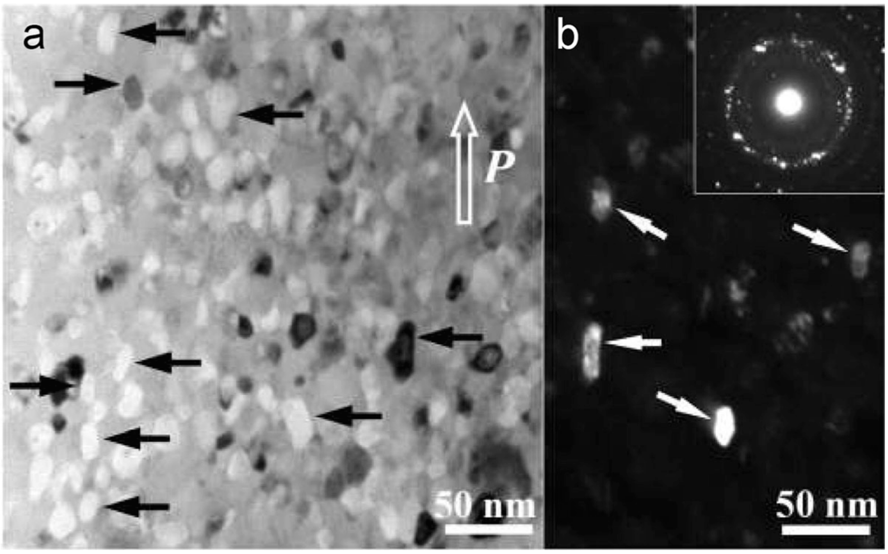

Fig. 45. Bimorphological SmCo/FeCo oriented nanostructures [374]. (a) Bright-field and (b) dark-field transmission electron microscopy (TEM) images and the corresponding selection area electron diffraction (SAED) patterns (inset) of the nanostructure. This nanostructure consists of the oriented rod-shaped SmCo grains (indicated with the arrows; ~10 nm in diameter and 20–40 nm in length) and the equiaxed Fe(Co) grains (~10 nm in diameter).

(~1 GPa) and large strain (~80 %), coupled with temperature gradient, enables their oriented growth in the amorphous matrix, producing aligned rod-shaped nanograins.

The resulting nanostructure exhibits a high energy density of 28 MGOe for this class of bulk nanocomposite magnets with low rare-earth contents and outperforms, for the first time, their corresponding pure rare-earth magnet, with 58 % enhancement in energy product. The superior performance is attributed to the enhanced magnetization-coercivity combination that is resulted from the magnetic coupling between nanostructured domains (grains), in which the oriented SmCo grains and the high fraction of ultrafine Fe (Co) grains contribute to high remanent magnetization (B_r), while the rod-shaped SmCo nanograins are favorable for large H_c, e.g., an increase of 22 % in H_c as compared to the equiaxed SmCo nanograins. The key idea of this strategy is the creation of ultrafine oriented SmCo nanograins (<10 nm in diameter) using strain-energy anisotropy through a solid-state phase transformation under the HPTC [372].

5.7.2. *Magnets with layered ordered nanostructure*

Huang *et al* devised a strategy to build bulk layered ordered nanostructures with functional units. The nanostructure is characterized by ordered layers of NdFeB nanograins embedded in a SmCo + FeCo nano-grained matrix (see Fig. 46) [379]. In contrast to previous studies, they utilize a blend of amorphous and nanocrystalline materials as precursor to realize the bulk layered nanostructure by HPTC. First, the FeCo particles were homogeneously dispersed in a Sm-Co amorphous matrix through mechanically milling to control their grain size, distribution, and fraction. Second, the SmCo-based amorphous precursor was thoroughly mixed with NdFeB nanocrystalline ribbon powder. Next, the mixed precursor was consolidated into a bulk material and deformed by HPTC to yield the desirable ordered structures with alternating layers of (FeCo + SmCo) and NdFeB, while the HPTC produced the oriented SmCo and NdFeB nanograins.

The ordered layered architecture makes a significant contribution to the strong exchange-coupling between soft and hard magnetic grains at high soft magnetic fractions and has an important impact on magnetization reversal, for example, leading to previously unachievable multi-step pinning behavior in magnetic reversal process. Such unique magnetization reversal mechanism enables a favorable combination of high B_r and large H_c. As a result, the layered ordered nanostructure exhibits a record-high energy product (31 MGOe) achieved to date for this class of bulk nanocomposite magnets, with the soft magnetic fraction exceeding 20 wt%. Moreover, the novel design strategy allows separate manipulation of conflicting components in different layers and thus enables simultaneous control over all the structural properties of constituents on the nanometer scale, which is significant for the fabrication of heterostructured materials in a well-controlled way.

5.7.3. *Magnets with core/shell heterogeneous nanostructures*

A core/shell nanostructure enables efficient interaction (e.g., exchange coupling) between the core and shell constituents, but its synthesis is generally limited to nanoparticles. Li *et al.* reported a self-assembly strategy to fabricate three-dimensional (3D) core/shell nanostructures, with hard-magnetic $Nd_2Fe_{14}B$ core (~45 nm in diameter) and soft-magnetic α-Fe shell (~10 nm in thickness) grains (Fig. 47) [380]. A major advantage of the core/shell heterogeneous nanostructure over the conventional homogeneous nanostructure is to realize a strong exchange coupling between the hard and soft magnetic grains, when a high soft-magnetic fraction (~30 wt%) is present. The resulting 3D core/shell nanostructure allows both high B_r and large H_c, leading to a large energy product of 25 MGOe. The 3D core/shell nanostructures were fabricated through sequential growth of the core and shell nanocrystals in a Nd-Fe-B melt. It is anticipated that by aligning the hard-phase grains along their easy magnetization axes, higher energy products can be achieved in such core/shell heterostructured magnets.

5.7.4. *Magnets with gradient ordered nanostructure*

In principle, ordered structures with gradient variation in grain sizes should have important impacts on magnetization reversal and macroscopic properties of magnetic materials, as large grains have a lower reverse field than that of smaller ones [378]. Recently, by engineering $Nd_2Fe_{14}B$/α-Fe gradient ordered nanostructures (Fig. 48) [381], Lou and co-workers discovered a directional magnetization reversal that initiates first in large grains and then towards smaller ones through micromagnetism simulations and experiments (Fig. 49). This is in contrast to the conventional random and nonuniform magnetization reversal in ferromagnetic materials. Such directional magnetic reversal enables them to achieve a large H_c without sacrificing M_s, thus leading to a record-high energy product (26 MGOe) for isotropic nanocomposite magnets which usually have values of approximately 20 MGOe. The directional magnetization reversal is achieved by judiciously creating an orderly arrangement of grain sizes and phase contents within the material, thus yielding an ordered magnetization reversal.

To realize this idea, Lou *et al.* successfully fabricated $Nd_2Fe_{14}B$/α-Fe nanostructures with gradient variations in both the grain size and α-Fe content by solidification with a temperature gradient using the melt-spinning (MS) technique with Nd-Fe-B alloys [381]. They suggest that the grain gradient in engineered α-Fe/$Nd_2Fe_{14}B$ nanostructures originates from the MS process with a temperature gradient, while the α-Fe phase gradient might result from deliberately introduced cluster structures (or crystal nuclei) in alloy melt, which might have nonuniform spatial distributions in the melt and thus cause the α-Fe phase gradient by heterogeneous nucleation in the MS process.

This strategy proposed by Lou *et al.* should be general and applicable to other systems for creating ordered structures, e.g., grain gradient and phase gradient, to achieve superior mechanical and functional properties. The methodology using cluster structures in alloy melt could be directly applied to manipulate phase transformation in solidification processes, e.g., to produce ultrafine nanocrystalline materials with simpler compositions and/or to fabricate new structural and functional materials.

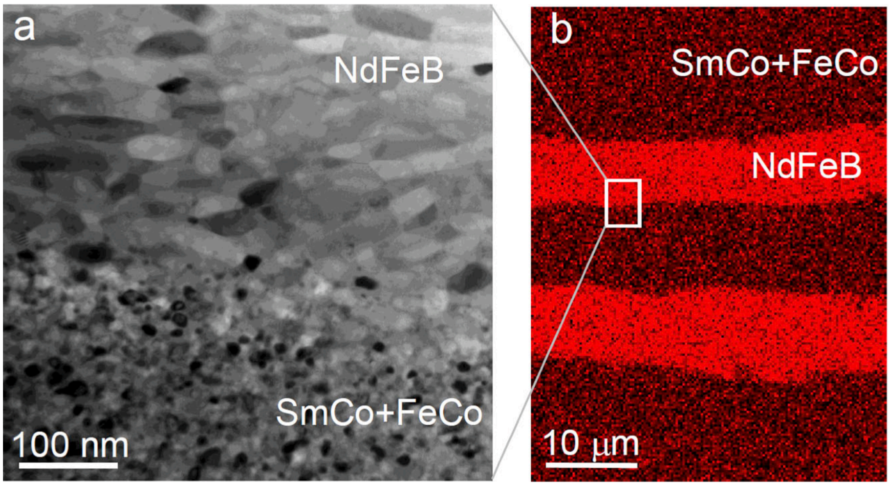

Fig. 46. NdFeB/(SmCo + FeCo) layered ordered nanostructures [379]. (a) TEM image and (b) energy dispersive X-ray (EDX) mapping (using Fe Kα_1, red) of a layered ordered nanostructure. The layers of NdFeB nanograins are embedded in a SmCo + FeCo nano-grained matrix.

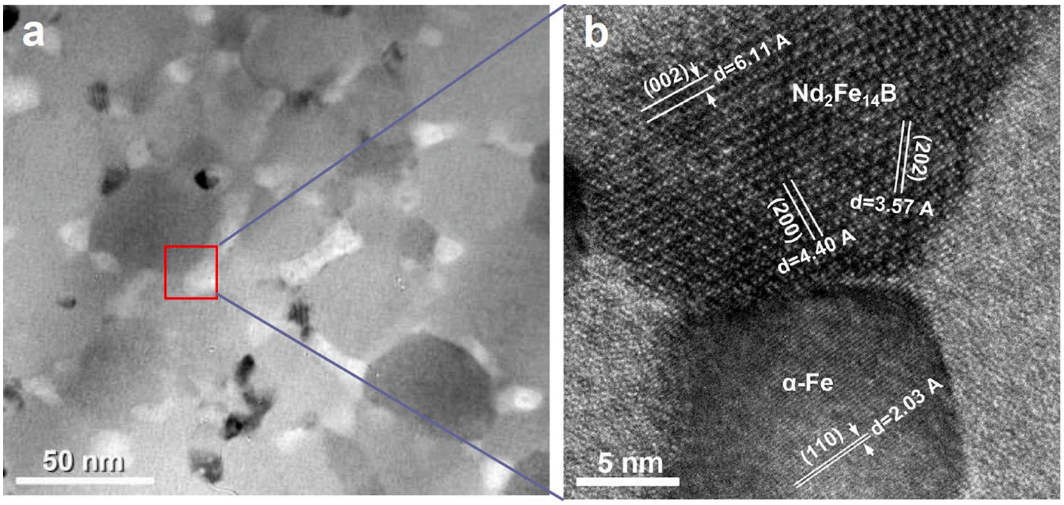

Fig. 47. $Nd_2Fe_{14}B$/α-Fe core/shell heterostructures [380]. (a) TEM and (b) high-resolution TEM images of a core/shell heterogeneous nanostructure. The nanostructure comprises $Nd_2Fe_{14}B$ core (~45 nm in diameter) and α-Fe shell (~10 nm in thickness) grains.

6. Design principles of heterostructured materials

As discussed in Section 4, the superior mechanical properties of heterostructured (HS) materials are attributed to the hetero-deformation induced (HDI) strengthening to enhance the yield strength and the HDI strain hardening to retain and even increase the ductility [1,15,181]. Therefore, it is critical to design alloys and their heterostructures to enhance the HDI stress. In this section, we will discuss the principles of designing HS materials for the best mechanical properties.

6.1. *Alloy design*

The HDI stress is collectively produced by a pair of stresses that are opposite in directions: back stress and forward stress. Locally, the back stress is produced by the piling up of geometrically necessary dislocations (GNDs) in a soft zone, which produces a stress concentration at the zone boundary with a magnitude of $n\tau_a$ [73,213,214], where n is the number of GNDs and τ_a is the applied shear stress. The stress concentration induces the forward stress across the zone boundary in the hard domain. On the zone boundary, the back stress and the forward stress balance each other since they are the same in magnitude but opposite in direction. However, the stress distribution in the soft zone and the hard zone will be different. Therefore, the evolutions of back stress and forward stress are not a zero-sum game overall. This produces the global HDI stress, which can be measured using the loading-reloading experiment during a tensile or compressive testing.

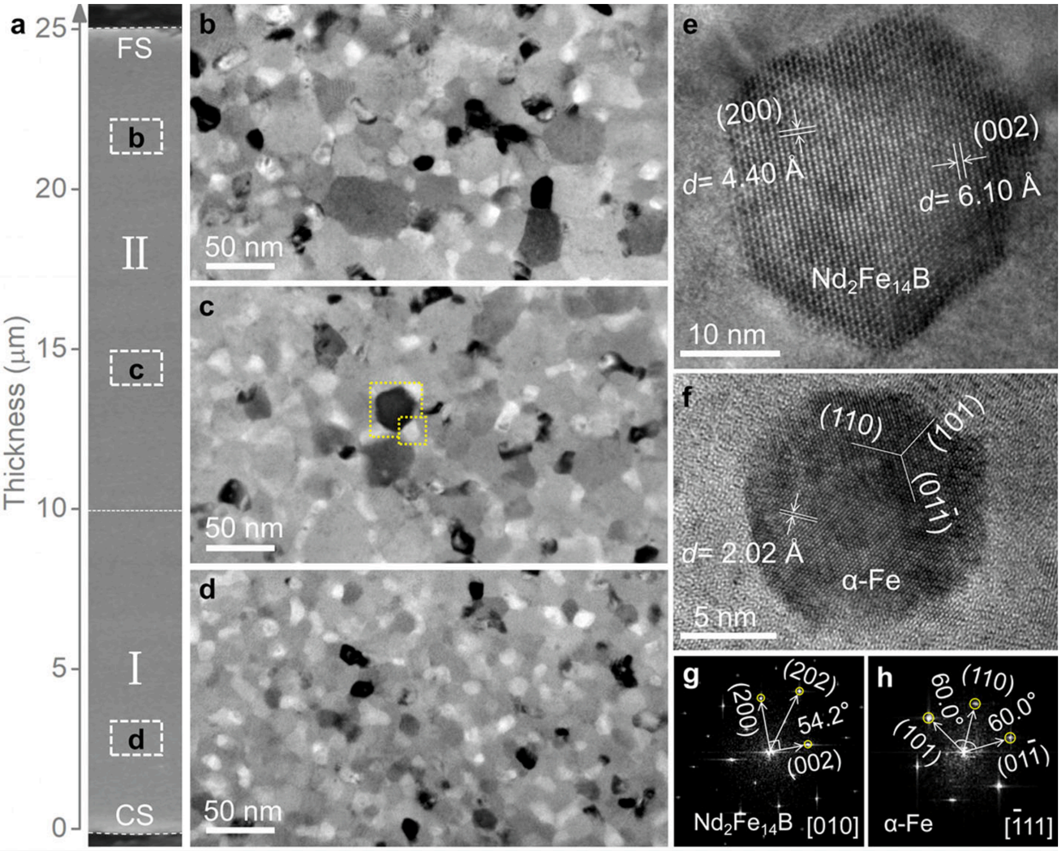

Fig. 48. $Nd_2Fe_{14}B$/α-Fe gradient ordered nanostructures [381]. (a) Cross-sectional SEM image and (b to d) bright-field TEM images of a gradient nanostructure marked in (a), with an ordered arrangement of grain sizes from the cooling side (CS) to the free side (FS) of melt-spun ribbons. (e to h) High-resolution TEM images and their corresponding fast Fourier transformation (FFT) of the coarse (e and g) and small (f and h) nanograins marked in (c).

Logically, it can be assumed that higher back stress should lead to higher forward stress, and consequently higher HDI stress. To produce higher back stress, it is desired for dislocations to slip in a planar manner so that they can easily pile-up against the zone boundaries. There are several ways to promote planar slip, including lowering stacking fault energy (SFE) [238], and short-range solute clustering (ordering) [382,383]. Other factors that promote planar slip in fcc metals include high shear modulus, large atomic misfit, and high solute content [384].

The key to maintaining planar slip is to prevent dislocation from cross-slipping. In fcc metals, a perfect dislocation is often dissociated into two partial dislocations with a stacking fault in between to form a stacking fault ribbon [124]. The stacking fault width is determined by the balance of the repulsive force between the two partials and the extra energy in the stacking fault. Lower stacking fault energy leads to a wider stacking fault, i.e., larger separation of the two partials. For cross-slip to occur, the two partials need to be combined to form a perfect dislocation first, which has an energy barrier that needs to be overcome by the applied shear stress. Larger separation makes it more difficult for the two partials to come together to combine, which makes cross slip more difficult. In other words, low SFE promotes planar slip. This is reflected in the defect structure formed by deformation. It is reported that low SFE fcc alloys such as stainless steel typically form GND pileups near grain boundaries due to planar slip [238], while medium to high SFE metals and alloys such as Cu and Al typically form cell structures due to cross-slip of dislocations [238,385,386].

Logically, any factors that makes it more difficult for the two partials of a perfect dislocation to combine should promote planar slip. It is reasoned that solute atoms, large atomic misfits, and high shear modulus promote planar slip because they increase lattice friction for dislocation slip and hence make it harder for the partials to move together [384]. This may be the reason why high-entropy alloys often has very high strain hardening [387–390].

Short-range solute clustering and ordering promote planar slip because the leading partial destroys the clustering/ordering, leading to slip plane softening [382,383,390]. Small precipitates that can be cut through by dislocations have similar effect.

Crystal structures may also have a significant effect on the planar slip and consequently high HDI stress. It has been observed that hcp Ti usually has planar slip [2,391]. As a result, heterostructured Ti has been found very effective in producing the HDI strengthening and hardening to improve strength and ductility [2]. Due to the low symmetry and limited slip systems of hcp crystal systems [392], it is more difficult for dislocations to cross slip from one slip plane onto another slip plane. Therefore, it is expected that heterostructured

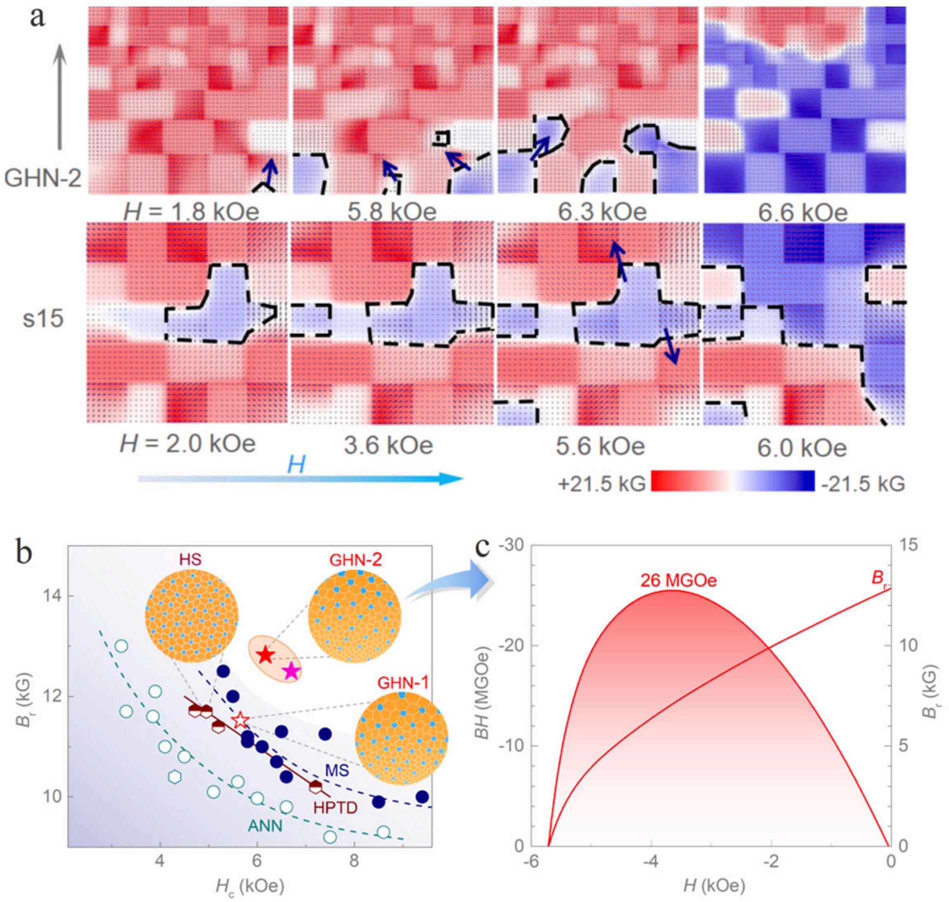

Fig. 49. Magnetization reversal and magnetic properties of $Nd_2Fe_{14}B/\alpha\text{-}Fe$ gradient ordered nanostructures [381]. (a) Micromagnetism simulations on magnetization reversal of gradient (GHN-2) and homogeneous (s15) nanostructures. (b) Remanence (B_r) and coercivity (H_c) of representative isotropic $\alpha\text{-}Fe/Nd_2Fe_{14}B$ nanocomposite magnets prepared by various approaches. (c) Energy products (BH curve) of the synthesized GHN-2, where magnetic-field induction $B = H + 4\pi M$.

hcp metals and alloys can develop high HDI strengthening and strain hardening. This has been demonstrated in heterostructured Ti. Further experimental studies on other hcp metals and alloys are needed to verify this hypothesis.

As discussed earlier, dual phase materials represent a type of effective heterostructures. Alloy design is also needed to produce the most effective HDI hardening. It is desirable to design dual-phase materials with relatively large strength difference between the two phases so that stronger HDI hardening is produced. In addition, it is also desired that both phases have good plasticity so that cracks do not develop to fail the materials, which allows the HDI hardening to work to improve ductility.

6.2. Heterostructures design

From our current understanding of the physics of heterostructured materials [1,2,13,181,299], we can provide qualitative guidance to the design of heterostructures. As discussed earlier, HDI strengthening and HDI strain hardening are responsible for the observed superior mechanical properties and behaviours. Therefore, it will be desirable to maximize the effect of back stress and minimize the effect of forward stress so that the HDI stress can be maximized. To this end, the heterostructure should be designed to promote GND pileups, in terms of their number density as well as the lengths of individual pileups. In addition, the strength difference between the hard zones and soft zones should be large so that the effect of the forward stress on the hard zone can be reduced. Note that the forward stress adds to the applied stress in the hard zone to deform the hard zone. Large difference in strength allows higher back stress to build up in the soft zone before the hard zone starts to yield, which consequently increases the yield strength. Lastly, it is important for the hard zones to be plastically deformable so that the zone interface will not fail, in which case void or cracks will be initiated at the zone boundaries. The nucleation and growth of voids is another type of failure mechanism, which could occur even under high strain hardening rate. This is another failure mode that may occur before necking. This is the reason why most metal matrix composites reinforced with hard particles usually don’t have high ductility.

6.2.1. *Geometry of heterostructured zones*

To design superior heterostructures, it is necessary to keep in mind that for higher HDI effect, we need to increase the number of pile-ups per unit sample volume. It naturally follows that we need to increase the density of zone boundaries to provide more potential locations for GND to pile up. Therefore, a lamellar structure in which the soft zone is flattened will be much more effective in promoting HDI effect than an equiaxed structure because the former has higher boundary area to volume ratio. Indeed, we have found that lamellar structured Ti with micrometer-sized soft Ti lamellar embedded in ultrafine grained (UFG) matrix produced the best heterostructure effect, i.e. exhibiting the strength of the UFG matrix and even higher ductility than the coarse-grained Ti [2], which was considered impossible according to our conventional understanding of materials science.

Another type of heterostructure with high zone boundary area per unit volume is for the soft zone to have a needle geometry, which also have high boundary area to volume ratio. Recent experimental results indeed verified that such a heterostructure can produce superior combination of strength and ductility [393].

Importantly, the two types of heterostructures discussed above are conducive to large-scale conventional industrial production. Specifically, the lamellar heterostructure can be produced by rolling while the needle heterostructure can be produced by extrusion, both of which are conventional processing technologies.

6.2.2. *Spacing of zone interfaces*

Since the GNDs are piled up against the zone boundaries, which produces the back stress, it naturally follows that there must be an optimum zone-boundary spacing, i.e., the thickness of the soft lamellae. If the spacing is too large, only the hetero-boundary affected region (HBAR) is contributing to back stress development, and other regions in the soft lamellae will be ineffective in promoting HDI strengthening and hardening. If the spacing is too small, there will not be enough space for the GNDs to pile up to their full capacity. Similar argument also applies to the hard zones. These are deliberated below.

There are two spacings to be considered for designing a heterostructure. The first is the zone boundary spacing across the soft zones, i.e., the soft zone thickness *t* as shown in Fig. 50. This should be determined by the average length of the GND pile-ups. The GND pile-ups produces a hetero-boundary affected region (HBAR) on both sides of a zone boundary [13]. The back stress is largely produced in the HBAR in the soft zone. It has been observed that the optimum zone boundary spacing across the soft zones, i.e. the soft zone thickness, is when the two HBARs across from a soft zone start to overlap, which is about 15 μm in the case of Cu-bronze layered heterostructure [13]. When the Cu layer thickness is>15 μm, both yield strength and ductility increase with decreasing thickness. However, when the thickness is smaller than 15 μm, decreasing the thickness will decrease the ductility although the yield strength will continue to increase. The observed thickness effect is caused by the influence of thickness on the effectiveness of HDI stress development. With decreasing thickness, the density of zone interfaces increases, which facilitates the development of GND pile-ups to increase the back stress. On the other hand, below a critical thickness at which the HBARs start to overlap, further decreasing the

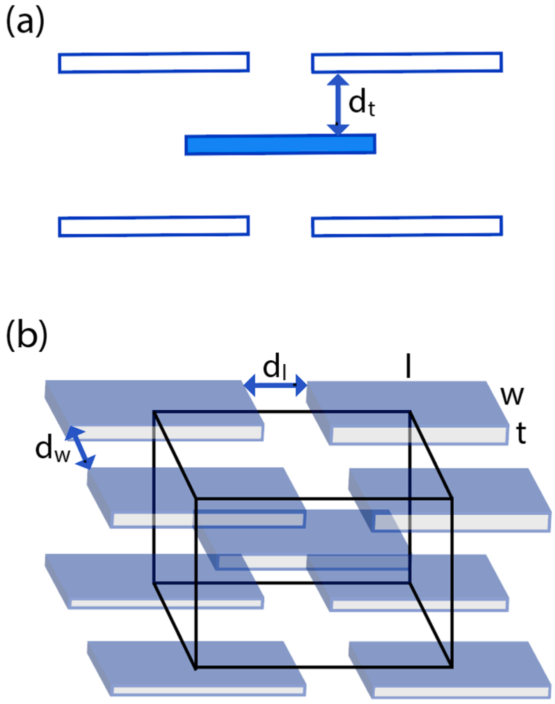

Fig. 50. Schematics of a mathematical model for heterogeneous lamellar structure. The platelets represent the soft zone lamellae. (a) The side view of the lattice of soft zone lamellae. (b) The 3D representation of the lattice unit cell of the soft zone lamellae, which is in a body centered orthorhombic arrangement.

thickness limits the space available for GND pile-ups to fully develop, which reduces the HDI strain hardening rate.

The zone boundary spacing across the hard zone (*d* in Fig. 50) should also play a role in the HDI strain hardening, although it is not well understood. The HBAR thickness in the hard zones should be associated with how fast the forward stress decays with increasing distance from the zone boundary, as shown in Fig. 11. The hard zone thickness should be large enough to allow the HBAR development. This is not well understood and should be further studied. Experimentally, this is related to the volume fraction of the hard zones. As shown in Fig. 50, assuming the soft zone lamellae assemble in a body-centered orthorhombic lattice, the volume fraction of the soft zones can be easily derived as.

$$f_s = \frac{1}{(1 + d_l/l)(1 + d_w/w)(1 + d_t/t)} \tag{13}$$

where l, w and t are the length, width and thickness of the soft zone lamellae, respectively; d_l, d_w and d_t are the gaps of between soft zones along the length, width and thickness directions as definitions in Fig. 50. When the width w is comparable to thickness t, and l ≫ t, the soft zone will be shaped like a fiber, and the structure can be called as fibrous heterostructure.

As shown in Fig. 50, if the length l and width w of the soft lamellae are much larger than its thickness t, the structure can be approximated as a layered structure with alternative soft and hard layers. As discussed earlier, layer structured materials may have very high strength when the layer thickness is very small, but their ductility is usually not very high. The reason is that in the continuous layer structure, the soft and hard layers are forced to deform at about the same applied strain because of their mutual constraint. In other words, strain partitioning will be limited, which limits the HDI strain hardening. For the same reason, if the length l is much larger than thickness and the width is comparable to t, the structure can be approximated by soft long fibers/ribbons embedded in hard matrix, it will limit the strain partitioning in the longitudinal direction, which also limits the HDI hardening. In summary, it is not desired for the soft zones to have any dimension to be too large.

6.2.3. *Volume fraction of the soft zones*

Heterostructured (HS) materials should be designed to have the soft zones embedded in a hard but plastically deformable matrix. The volume fraction of the soft zones is an important parameter for producing superior mechanical properties in HS materials. It was found that for the HS lamella Ti, the optimum volume fraction of the soft zone is in the range of 20 % to 30 % [2]. The optimum volume fraction may be influenced by several factors such as the morphology and texture of heterostructures, the strength difference between the soft and hard zones as well as the SFE of the soft zones. It is deduced that for the highest HDI strengthening and strain hardening, the soft zones should be fully constrained by the matrix of hard zones. In other words, the hard zones should connect to form a continuous hard matrix network. In such a scenario, during a tensile test, the soft zone will try to start plastic deformation first by activating dislocation sources such as the Frank-Read source. GNDs from dislocation sources will glide and be stopped by the zone boundaries where they pile up [2]. This will produce back stress in the soft zone to increase the global yield strength. Because the soft zones are totally surrounded and constrained by the hard matrix, they cannot plastically deform to change their shape easily, thus making it effective to build up the back stress, which significantly improves the yield strength. This has been demonstrated in HS lamellar Ti [2].

Logically, for the soft zones to be embedded in the hard matrix, the volume fraction of the soft zones should be<50 %. In addition, the volume fraction of the hard zones should be high enough to fully constrain the soft zones. This explains why the optimum volume fraction of the soft zones is far below 50 %.

On the other hand, if the volume fraction of the soft zones is above 50 %, the soft zones will form a network so that the plastic strain path can go around the hard zones to cause global yielding. In other words, a heterostructure with hard zones embedded in a soft matrix will have limited capability to increase the global yield strength. However, this is exactly what is designed in most composite materials and dual phase materials reported in the literature and used in practical applications.

7. Perspectives and outstanding issues

Heterostructured (HS) materials are a class of materials that not only have vast opportunities for fundamental studies to pave their scientific foundation, but also have great potentials for fast industrial applications. The commercialization and practical applications of new materials are often stymied by the following two critical factors. The first factor is the scalability of the technology for large-scale industrial production. This often needs extensive research and development. The scaling up of new technologies from laboratory to commercial production often takes a long time at very high cost. What works well in a laboratory may not work at large scale or may not work consistently for easy control of the quality of the commercial product. The second factor is the cost, which includes the cost of purchasing and installing production facility as well as the cost of producing the product itself. New materials are developed to enable new technologies or to replace existing materials. The replacement of existing materials is especially cost sensitive for civilian products such as automobiles. The scaling up for commercialization of a new technology is often in the R&D stage when the public funding for fundamental research is drying up while the technology is not mature enough to attract sufficient private funding from for-profit companies for commercialization. Consequently, the technology dies without being able to secure enough funding to sustain its R&D activities. Promising technologies die so often in this stage that it is dubbed the technological “valley of death” [394].

One of the biggest advantages of HS materials is that they can be produced by current industrial technologies and facilities, which eliminates any technology barrier for their commercialization. It also avoids upfront huge capital investment. The adoption of the current industrial technology and facilities makes it very economical to produce HS materials at low cost, which makes them competitive when compared with existing materials. For example, HS steels can be processed using the current industrial rolling and annealing process at steel mills, which could potentially develop a new series of high-performance and low-cost steels for the manufacturing industries such as automobiles. In fact, common industrial thermo-mechanical technologies and facilities such as forging, rolling, extrusion, drawing, and heat treatment can all be used to process HS metals and alloys. It is this potential for industrial applications that will sustain HS materials for a long-lasting life.

As a new materials field, there are many known and unknown fundamental and engineering issues to be solved, which provides for abundant research opportunities for the materials community. A new scientific principle, hetero-deformation induced (HDI) strengthening and HDI hardening, is responsible for the superior mechanical properties of HS materials, which is a major factor in determining their mechanical behavior. The HDI strengthening and HDI hardening are adding to the conventional dislocation-based strengthening and hardening to provide additional enhancement of strength and ductility. Below we will discuss the scientific and engineering issues that are hitherto known in the field of HS materials.

The first issue is the interaction of geometrically necessary dislocations (GNDs) with zone boundaries to develop hetero-deformation induced (HDI) stress. Logically, when an array of GNDs slip toward a zone boundary, they may be stopped in front of the boundary, transmitted across the boundary, pushed into the boundary, or reflected from the boundary. They may also cross slip to escape the pile up. These scenarios will determine the effectiveness in producing the HDI strengthening and hardening. The occurrence of these scenario will be influenced by the intrinsic properties of materials such as the stacking fault energy and crystal structure, as well as the microstructural characteristics such as zone boundary structure and misorientation, strength difference across the boundary, crystal structure difference across the boundary, etc.

GND pile-ups against zone boundaries is the most effective way to produce back stress in the soft zones and forward stress in the hard zones, which consequently produce high HDI stress. Stacking fault energy (SFE) should affect the GND pile-up. Low SFE promotes planar dislocation slip, which makes it easier for GNDs to pile up, while high SFE makes it easier for GNDs to cross slip to avoid a long pile-up. Therefore, it can be deduced that the SFE will affect the development of HDI stress and HDI hardening. This needs a systematic study. The scenario of GNDs being pushed into the zone boundary and absorbed by the boundary has been observed in an *in-situ* TEM study of Cu-bronze layered structure [240]. The GND absorption by and transmission across the zone boundary will logically lead to the saturation of the number of GNDs in the pile up. These need to be studied so that we can understand the HDI evolution and mechanical behavior of HS materials. Other unknown GND-zone boundary interactions may also exist, which will be discovered in the future.

The second issue is the mechanisms for the nucleation and growth of dispersed shear bands, and their relationship with GND pile ups. Highly dispersive strain bands have been observed in almost all HS materials reported so far. It is an effective way for the HS materials to distribute the plastic deformation over a longer gage length to delay the formation of a major strain localization to fail the sample. It is critical to probe the nucleation and growth mechanisms of local strain bands. One hypothesis is that the nucleation of a local strain band is associated with one or multiple GND pile ups, but this is yet to be verified experimentally. This is critical to understanding the deformation mechanisms of HS materials. In addition, it is suspected that local strain bands are most likely shear bands, i.e., caused by local shear strains, which needs to be verified.

The third is computational investigation, coupled with experimental study, to probe the GND interaction with the zone boundaries, after which analytical modelling is needed to derive equations to predict the optimal hetero-zone size, geometry and distribution for the best strength-ductility combination. The heterostructured materials reported so far have been largely made by the trial-and-error approach. Although we already have some basic idea on how to design HS materials, as discussed in the last section, we still don't understand the HS materials enough to quantitatively design the heterostructures. The ultimate goal is to design HS materials using their composition and desired heterostructure for the best mechanical or physical properties.

The fourth issue is to combine different heterostructures to develop dual heterostructures or trio heterostructures, and to synergistically couple heterostructures with conventional toughening mechanisms such as the transformation induced plasticity (TRIP), twinning induced plasticity (TWIP), or deformation twinning, etc. If each strain hardening mechanisms are activated sequentially at different straining stage, it may maintain high strain hardening rates to a very high tensile strain, i.e., producing very high ductility. The sequential activation of multiple strain hardening (SMSH) strategy has been reported in a heterostructured high-entropy alloy, which is the first successful attempt in this direction [395] and ultrafine grained materials [396]. There are endless possible combinations among HS structures and with other conventional toughening mechanisms, which provides for a vast design space for HS materials.

The fifth issue is the development of processing technologies with good control of the heterostructures, good scalability and low processing cost. This is critical for the real-world commercial applications of heterostructured materials.

Declaration of Competing Interest

The authors declare that they have no known competing financial interests or personal relationships that could have appeared to influence the work reported in this paper.

Acknowledgements

The authors acknowledge the help of Prof. Xiangyi Zhang in writing the section 5.7 on functional heterostructured materials. This work is supported by the Ministry of Science and Technology of China (2021YFA1200202, 2019YFA0209900 and 2017YFA0204402), the National Natural Science Foundation of China (11988102, and 11972350), the Hong Kong Research Grants Council (GRF 11214121), the Hong Kong Institute for Advanced Study, City University of Hong Kong, and the Chinese Academy of Sciences (Grant

No. XDB22040503).

References

[1] Wu XL, Zhu YT. Heterogeneous materials: a new class of materials with unprecedented mechanical properties. Mater Res Lett 2017;5:527–32.
[2] Wu XL, Yang MX, Yuan FP, Wu GL, Wei YJ, Huang XX, et al. Heterogeneous lamella structure unites ultrafine-grain strength with coarse-grain ductility. Proc Natl Acad Sci USA 2015;112:14501–5.
[3] Suresh S. Graded materials for resistance to contact deformation and damage. Science 2001;292:2447–51.
[4] Miserez A, Schneberk T, Sun CJ, Zok FW, Waite JH. The transition from stiff to compliant materials in squid beaks. Science 2008;319:1816–9.
[5] Gao Z, Zhang YY, Song NN, Li XD. Biomass-derived renewable carbon materials for electrochemical energy storage. Mater Res Lett 2017;5:69–88.
[6] Wu XL, JIang P, Chen L, Zhang JF, Yuan FP, Zhu YT. Synergetic Strengthening by Gradient Structure. Mater Res Lett. 2014;2:185-91.
[7] Chung KF, Yu WK. Mechanical properties of structural bamboo for bamboo scaffoldings. Eng Struct 2002;24:429–42.
[8] Espinosa HD, Rim JE, Barthelat F, Buehler MJ. Merger of structure and material in nacre and bone - Perspectives on de novo biomimetic materials. Prog Mater Sci 2009;54:1059–100.
[9] Gopalan H, Chokshi AH. The mechanical behavior of nacre across length scales. J Mech Behav Biomed 2018;78:96–107.
[10] Lin AYM, Meyers MA. Interfacial shear strength in abalone nacre. J Mech Behav Biomed 2009;2:607–12.
[11] Lopez MI, Martinez PEM, Meyers MA. Organic interlamellar layers, mesolayers and mineral nanobridges: Contribution to strength in abalone (Haliotis rufescence) nacre. Acta Biomater 2014;10:2056–64.
[12] Ritchie RO. The conflicts between strength and toughness. Nature Mater 2011;10:817–22.
[13] Huang CX, Wang YF, Ma XL, Yin S, Höppel HW, Göken M, et al. Interface affected zone for optimal strength and ductility in heterogeneous laminate. Mater Today 2018;17:713–9.
[14] Wang JT. Historic Retrospection and Present Status of Severe Plastic Deformation in China. Mater Sci Forum 2006;503–504:363–70.
[15] Zhu YT, Ameyama K, Anderson PM, Beyerlein IJ, Gao HJ, Kim HS, et al. Heterostructured materials: superior properties from hetero-zone interaction. Mater Res Lett 2021;9:1–30.
[16] Zhu YT. Introduction to Heterostructured Materials: A Fast Emerging Field. Metall Mater Trans A 2021;52:4715–26.
[17] Yuan FP, Yan DS, Sun JD, Zhou LL, Zhu YT, Wu XL. Ductility by shear band delocalization in the nano-layer of gradient structure. Mater Res Lett 2019;7:12–7.
[18] Zhu YT, Wu XL. Ductility and plasticity of nanostructured metals: differences and issues. Mater Today Nano 2018;2:15–20.
[19] Yang MX, Pan Y, Yuan FP, Zhu YT, Wu XL. Back stress strengthening and strain hardening in gradient structure. Mater Res Lett 2016;4:145–51.
[20] Ashby MF. Deformation of Plastically Non-Homogeneous Materials. Philos Mag 1970;21:399–1000.
[21] Gao H, Huang Y, Nix WD, Hutchinson JW. Mechanism-based strain gradient plasticity - I Theory. J Mech Phys Solids 1999;47:1239–63.
[22] Meyers MA, Chawla KK. Mechanical Behavior of Materials. Upper Saddle River, NJ: Prentice Hall, Inc; 1999.
[23] Wu XL, Jiang P, Chen L, Yuan FP, Zhu YT. Extraordinary strain hardening by gradient structure. Proc Natl Acad Sci USA 2014;111:7197–201.
[24] Fang TH, Li WL, Tao NR, Lu K. Revealing Extraordinary Intrinsic Tensile Plasticity in Gradient Nano-Grained Copper. Science 2011;331:1587–90.
[25] Cheng Z, Zhou HF, Lu QH, Gao HJ, Lu L. Extra strengthening and work hardening in gradient nanotwinned metals. Science 2018;362:559.
[26] Long JZ, Pan QS, Tao NR, Lu L. Residual stress induced tension-compression asymmetry of gradient nanograined copper. Mater Res Lett 2018;6:456–61.
[27] Ma XL, Huang CX, Moering J, Ruppert M, Höppel HW, Göken M, et al. Mechanical Properties in Copper/Bronze Laminates: Role of Interfaces. Acta Mater 2016;116:43–52.
[28] Ma XL, Huang CX, Xu WZ, Zhou H, Wu XL, Zhu YT. Strain hardening and ductility in a coarse-grain/nanostructure laminate material. Scripta Mater 2015;103:57–60.
[29] Beyerlein IJ, Mayeur JR, Zheng SJ, Mara NA, Wang J, Misra A. Emergence of stable interfaces under extreme plastic deformation. Proc Natl Acad Sci USA 2014;111:4386–90.
[30] Wang J, Zhou Q, Shao S, Misra A. Strength and plasticity of nanolaminated materials. Mater Res Lett 2017;5:1–19.
[31] Li X, Kreuter T, Luo XM, Schwaiger R, Zhang GP. Detecting co-deformation behavior of Cu-Au nanolayered composites. Mater Res Lett 2017;5:20–8.
[32] Yuan R, Beyerlein IJ, Zhou CZ. Homogenization of plastic deformation in heterogeneous lamella structures. Mater Res Lett 2017;5:251–7.
[33] Sawangrat C, Kato S, Orlov D, Ameyama K. Harmonic-structured copper: performance and proof of fabrication concept based on severe plastic deformation of powders. J Mater Sci 2014;49:6579–85.
[34] Vajpai SK, Ota M, Watanabe T, Maeda R, Sekiguchi T, Kusaka T, et al. The Development of High Performance Ti-6Al-4V Alloy via a Unique Microstructural Design with Bimodal Grain Size Distribution. Metall Mater Trans A 2015;46:903–14.
[35] Zhang Z, Vajpai SK, Orlov D, Ameyama K. Improvement of mechanical properties in SUS304L steel through the control of bimodal microstructure characteristics. Mater Sci Eng A 2014;598:106–13.
[36] Vajpai SK, Ota M, Zhang Z, Ameyama K. Three-dimensionally gradient harmonic structure design: an integrated approach for high performance structural materials. Mater Res Lett 2016;4:191–7.
[37] Park HK, Ameyama K, Yoo J, Hwang H, Kim HS. Additional hardening in harmonic structured materials by strain partitioning and back stress. Mater Res Lett 2018;6:261–7.
[38] Araki K, Takada Y, Nakaoka K. Work-Hardening of Continuously Annealed Dual Phase Steels. T Iron Steel I Jpn 1977;17:710–7.
[39] Davies RG. Influence of Martensite Composition and Content on Properties of Dual Phase Steels. Metall Trans A 1978;9:671–9.
[40] Davies RG. Deformation-Behavior of a Vanadium-Strengthened Dual Phase Steel. Metall Trans A 1978;9:41–52.
[41] Kadkhodapour J, Schmauder S, Raabe D, Ziaei-Rad S, Weber U, Calcagnotto M. Experimental and numerical study on geometrically necessary dislocations and non-homogeneous mechanical properties of the ferrite phase in dual phase steels. Acta Mater 2011;59:4387–94.
[42] Kundu A, Field DP. Influence of plastic deformation heterogeneity on development of geometrically necessary dislocation density in dual phase steel. Mater Sci Eng A 2016;667:435–43.
[43] Vaccari JA. Dual Phase Steels - Super Formable and 80,000 Psi +. Prod Eng 1978;49:50–4.
[44] Zhang JL, Morsdorf L, Tasan CC. Multi-probe microstructure tracking during heat treatment without an in-situ setup: Case studies on martensitic steel, dual phase steel and beta-Ti alloy. Mater Charact 2016;111:137–46.
[45] Li HQ, Misra A, Zhu YT, Horita Z, Koch CC, Holesinger TG. Processing and characterization of nanostructured Cu-carbon nanotube composites. Mater Sci Eng A 2009;523:60–4.
[46] Xu R, Fan GL, Tan ZQ, Ji G, Chen C, Beausir B, et al. Back stress in strain hardening of carbon nanotube/aluminum composites. Mater Res Lett 2018;6:113–20.
[47] Zhao L, Guo Q, Li Z, Fan GL, Li ZQ, Xiong DB, et al. Grain boundary-assisted deformation in graphene-Al nanolaminated composite micro-pillars. Mater Res Lett 2018;6:41–8.
[48] Liu J, Chen Z, Zhang FG, Ji G, Wang ML, Ma Y, et al. Simultaneously increasing strength and ductility of nanoparticles reinforced Al composites via accumulative orthogonal extrusion process. Mater Res Lett 2018;6:406–12.
[49] Wang YM, Chen MW, Zhou FH, Ma E. High tensile ductility in a nanostructured metal. Nature 2002;419:912–5.
[50] Witkin D, Lee Z, Rodriguez R, Nutt S, Lavernia E. Al-Mg alloy engineered with bimodal grain size for high strength and increased ductility. Scr Mater 2003;49:297–302.
[51] Lee Z, Witkin DB, Lavernia EJ, Nutt SR. Bimodal microstructure and mechanical properties of cryomilled nanocrystalline Al-7.5Mg. Nanomaterials for Structural Applications 2003;740:21–6.
[52] Choudhuri D, Shukla S, Green WB, Gwalani B, Ageh V, Banerjee R, et al. Crystallographically degenerate B2 precipitation in a plastically deformed fcc-based complex concentrated alloy. Mater Res Lett 2018;6:171–7.

[53] Chen AY, Li DF, Zhang JB, Song HW, Lu J. Make nanostructured metal exceptionally tough by introducing non-localized fracture behaviors. Scripta Mater 2008;59:579–82.
[54] Hertzberg RW. Deformation and Fracture Mechanics of Engineering Materials. 3rd ed. New York: Wiley; 1989.
[55] Smith WF, Hashemi J. Foundations of Materials Science and Engineering. 4th ed. Boston: McGraw-Hill; 2006.
[56] Wu XL, Zhu YT. Ductility and plasticity of nanostructured metals: differences and issues. Mater Today Nano 2018;2:15–20.
[57] Ovid'ko IA, Valiev RZ, Zhu YT. Review on superior strength and enhanced ductility of metallic nanomaterials. Prog Mater Sci. 2018;94:462-540.
[58] Zhao YH, Guo YZ, Wei Q, Topping TD, Dangelewicz AM, Zhu YT, et al. Influence of specimen dimensions and strain measurement methods on tensile stress-strain curves. Mater Sci Eng A 2009;525:68–77.
[59] Zhao YH, Guo YZ, Wei Q, Dangelewiez AM, Zhu YT, Langdon TG, et al. Influence of specimen dimensions on the tensile behavior of ultrafine-grained Cu. Scripta Mater 2008;59:627–30.
[60] Pande CS, Cooper KP. Nanomechanics of Hall-Petch relationship in nanocrystalline materials. Prog Mater Sci 2009;54:689–706.
[61] Meyers MA, Mishra A, Benson DJ. Mechanical properties of nanocrystalline materials. Prog Mater Sci 2006;51:427–556.
[62] Zhu YT, Liao XZ, Wu XL. Deformation twinning in nanocrystalline materials. Prog Mater Sci 2012;57:1–62.
[63] Cheng GM, Jian WW, Xu WZ, Yuan H, Millett PC, Zhu YT. Grain Size Effect on Deformation Mechanisms of Nanocrystalline bcc Metals. Mater Res Lett 2013;1:26–31.
[64] Yamakov V, Wolf D, Phillpot SR, Mukherjee AK, Gleiter H. Deformation-mechanism map for nanocrystalline metals by molecular-dynamics simulation. Nature Mater 2004;3:43–7.
[65] Van Swygenhoven H, Derlet PM, Froseth AG. Stacking fault energies and slip in nanocrystalline metals. Nature Mater 2004;3:399–403.
[66] Lu K, Lu L, Suresh S. Strengthening Materials by Engineering Coherent Internal Boundaries at the Nanoscale. Science 2009;324:349–52.
[67] Gleiter H. Nanocrystalline Materials. Prog Mater Sci 1989;33:223–315.
[68] Gleiter H. Nanostructured Materials. Adv Mater 1992;4:474–81.
[69] Porter DA, Easterling KE, Sherif MY. Phase Transformation in Metals and Alloys. Third Edition ed. New York: CRC Press; 2009.
[70] Li LL, Xu WZ, Saber M, Zhu YT, Koch CC, Scattergood RO. Influence of scandium addition on the high-temperature grain size stabilization of oxide-dispersion-strengthened (ODS) ferritic alloy. Mater Sci Eng A 2015;636:565–71.
[71] Saber M, Xu WZ, Li LL, Zhu YT, Koch CC, Scattergood RO. Size effect of primary Y2O3 additions on the characteristics of the nanostructured ferritic ODS alloys: Comparing as-milled and as-milled/annealed alloys using S/TEM. J Nucl Mater 2014;452:223–9.
[72] Clyne TW, Withers PJ. An Introduction to Metal Matrix Composites. New York: Cambridge University Press; 1995.
[73] Hull D, Bacon DJ. Introduction to Dislocations. 3rd ed. Oxford: Pergamon Press; 1984.
[74] Zhao YH, Liao XZ, Cheng S, Ma E, Zhu YT. Simultaneously increasing the ductility and strength of nanostructured alloys. Adv Mater 2006;18:2280–3.
[75] Valiev RZ, Alexandrov IV, Zhu YT, Lowe TC. Paradox of strength and ductility in metals processed by severe plastic deformation. J Mater Res 2002;17:5–8.
[76] Gleiter H. Deformation of polycrystals: mechanisms and microstructures: proceedings of the 2nd Risø International Symposium on Metallurgy and Materials Science. Demark: Roskilde; 1981.
[77] Gleiter H. Structure and Properties of Nanometer-Sized Materials. Phase Transitions 1990;24–6:15–34.
[78] Gleiter H. Nanostructured materials: Basic concepts and microstructure. Acta Mater 2000;48:1–29.
[79] Valiev RZ, Islamgaliev RK, Alexandrov IV. Bulk nanostructured materials from severe plastic deformation. Prog Mater Sci 2000;45:103–89.
[80] Valiev RZ. Nanostructuring of metals by severe plastic deformation for advanced properties. Nature Mater 2004;3:511–6.
[81] Valiev RZ, Estrin Y, Horita Z, Langdon TG, Zehetbauer MJ, Zhu YT. Producing bulk ultrafine-grained materials by severe plastic deformation. JOM 2006;58(4):33–9.
[82] Valiev RZ, Langdon TG. Principles of equal-channel angular pressing as a processing tool for grain refinement. Prog Mater Sci 2006;51:881–981.
[83] Koch CC. Structural nanocrystalline materials: an overview. J Mater Sci 2007;42:1403–14.
[84] Phillpot SR, Wolf D, Gleiter H. Molecular-Dynamics Study of the Synthesis and Characterization of a Fully Dense, 3-Dimensional Nanocrystalline Material. J Appl Phys 1995;78:847–61.
[85] VanSwygenhoven H, Caro A. Plastic behavior of nanophase Ni: A molecular dynamics computer simulation. Appl Phys Lett 1997;71:1652–4.
[86] Schiotz J, Di Tolla FD, Jacobsen KW. Softening of nanocrystalline metals at very small grain sizes. Nature 1998;391:561–3.
[87] Yamakov V, Wolf D, Salazar M, Phillpot SR, Gleiter H. Length-scale effects in the nucleation of extended dislocations in nanocrystalline Al by molecular-dynamics simulation. Acta Mater 2001;49:2713–22.
[88] Derlet PM, Van Swygenhoven H. Length scale effects in the simulation of deformation properties of nanocrystalline metals. Scripta Mater 2002;47:719–24.
[89] Van Swygenhoven H, Derlet PM, Hasnaoui A. Atomic mechanism for dislocation emission from nanosized grain boundaries. Phys Rev B 2002;66:024101.
[90] Yamakov V, Wolf D, Phillpot SR, Gleiter H. Deformation twinning in nanocrystalline Al by molecular dynamics simulation. Acta Mater 2002;50:5005–20.
[91] Yamakov V, Wolf D, Phillpot SR, Gleiter H. Grain-boundary diffusion creep in nanocrystalline palladium by molecular-dynamics simulation. Acta Mater 2002;50:61–73.
[92] Yamakov V, Wolf D, Phillpot SR, Mukherjee AK, Gleiter H. Dislocation processes in the deformation of nanocrystalline aluminium by molecular-dynamics simulation. Nature Mater 2002;1:45–8.
[93] Gutkin MY, Ovid'ko IA, Skiba NV. Crossover from grain boundary sliding to rotational deformation in nanocrystalline materials. Acta Mater 2003;51:4059–71.
[94] Schiotz J, Jacobsen KW. A maximum in the strength of nanocrystalline copper. Science 2003;301:1357–9.
[95] Yamakov V, Wolf D, Phillpot SR, Gleiter H. Dislocation-dislocation and dislocation-twin reactions in nanocrystalline Al by molecular dynamics simulation. Acta Mater 2003;51:4135–47.
[96] Froseth AG, Derlet PM, Van Swygenhoven H. Dislocations emitted from nanocrystalline grain boundaries: nucleation and splitting distance. Acta Mater 2004;52:5863–70.
[97] Wolf D, Yamakov V, Phillpot SR, Mukherjee A, Gleiter H. Deformation of nanocrystalline materials by molecular-dynamics simulation: relationship to experiments? Acta Mater 2005;53:1–40.
[98] Langdon TG. Twenty-five years of ultrafine-grained materials: Achieving exceptional properties through grain refinement. Acta Mater 2013;61:7035–59.
[99] Estrin Y, Vinogradov A. Extreme grain refinement by severe plastic deformation: A wealth of challenging science. Acta Mater 2013;61:782–817.
[100] Valiev RZ, Estrin Y, Horita Z, Langdon TG, Zehetbauer MJ, Zhu YT. Fundamentals of Superior Properties in Bulk NanoSPD Materials. Mater Res Lett 2016;4:1–21.
[101] Nieman GW, Weertman JR, Siegel RW. Mechanical-Behavior of Nanocrystalline Cu and Pd. J Mater Res 1991;6:1012–27.
[102] Fougere GE, Weertman JR, Siegel RW. Processing and Mechanical-Behavior of Nanocrystalline Fe. Nanostru Mater 1995;5:127–34.
[103] Rittner MN, Weertman JR, Eastman JA. Structure-property correlations in nanocrystalline Al-Zr alloy composites. Acta Mater 1996;44:1271–86.
[104] Sanders PG, Weertman JR, Barker JG. Structure of nanocrystalline palladium and copper studied by small angle neutron scattering. J Mater Res 1996;11:3110–20.
[105] Sanders PG, Fougere GE, Thompson LJ, Eastman JA, Weertman JR. Improvements in the synthesis and compaction of nanocrystalline materials. Nanostru Mater 1997;8:243–52.
[106] Rittner MN, Weertman JR, Eastman JA, Yoder KB, Stone DS. Mechanical behavior of nanocrystalline aluminum-zirconium. Mater Sci Eng A 1997;237:185–90.
[107] Sanders PG, Youngdahl CJ, Weertman JR. The strength of nanocrystalline metals with and without flaws. Mater Sci Eng A 1997;234:77–82.
[108] Agnew SR, Elliott BR, Youngdahl CJ, Hemker KJ, Weertman JR. Microstructure and mechanical behavior of nanocrystalline metals. Mater Sci Eng A 2000;285:391–6.
[109] Koch CC. Synthesis of nanostructured materials by mechanical milling: Problems and opportunities. Nanostruct Mater 1997;9:13–22.
[110] Malow TR, Koch CC. Mechanical properties, ductility, and grain size of nanocrystalline iron produced by mechanical attrition. Metall Mater Trans A 1998;29:2285–95.

[111] Koch CC. Bulk Behavior of Nanostructured Materials. In: Siegel RW, Hu E, Roco MC, editors. Nanostructure Science and Technology, A Worldwide Study: Final Report by WTEC Panel; 1999. p. 93.

[112] Huang B, Perez RJ, Lavernia EJ. Grain growth of nanocrystalline Fe-Al alloys produced by cryomilling in liquid argon and nitrogen. Mater Sci Eng A 1998;255:124–32.

[113] He L, Ma E. Processing and microhardness of bulk Cu-Fe nanocomposites. Nanostru Mater 1996;7:327–39.

[114] Zheng BL, Ertorer O, Li Y, Zhou YZ, Mathaudhu SN, Tsao CYA, et al. High strength, nano-structured Mg-Al-Zn alloy. Mater Sci Eng A 2011;528:2180–91.

[115] Wen HM, Zhao YH, Zhang ZH, Ertorer O, Dong SM, Lavernia EJ. The influence of oxygen and nitrogen contamination on the densification behavior of cryomilled copper powders during spark plasma sintering. J Mater Sci 2011;46:3006–12.

[116] Zhang X, Wang H, Scattergood RO, Narayan J, Koch CC, Sergueeva AV, et al. Studies of deformation mechanisms in ultra-fine-grained and nanostructured Zn. Acta Mater 2002;50:4823–30.

[117] Zhang X, Wang H, Scattergood RO, Narayan J, Koch CC, Sergueeva AV, et al. Tensile elongation (110%) observed in ultrafine-grained Zn at room temperature. Appl Phys Lett 2002;81:823–5.

[118] Youssef KM, Scattergood RO, Murty KL, Koch CC. Ultratough nanocrystalline copper with a narrow grain size distribution. Appl Phys Lett 2004;85:929–31.

[119] Youssef KM, Scattergood RO, Murty KL, Horton JA, Koch CC. Ultrahigh strength and high ductility of bulk nanocrystalline copper. Appl Phys Lett 2005;87:091904.

[120] Youssef KM, Scattergood RO, Murty KL, Koch CC. Nanocrystalline Al-Mg alloy with ultrahigh strength and good ductility. Scripta Mater 2006;54:251–6.

[121] Liao XZ, Huang JY, Zhu YT, Zhou F, Lavernia EJ. Nanostructures and deformation mechanisms in a cryogenically ball-milled Al-Mg alloy. Philos Mag 2003;83:3065–75.

[122] Liao XZ, Zhou F, Lavernia EJ, He DW, Zhu YT. Deformation twins in nanocrystalline Al. Appl Phys Lett 2003;83:5062–4.

[123] Liao XZ, Zhou F, Lavernia EJ, Srinivasan SG, Baskes MI, He DW, et al. Deformation mechanism in nanocrystalline Al: Partial dislocation slip. Appl Phys Lett 2003;83:632–4.

[124] Liao XZ, Srinivasan SG, Zhao YH, Baskes MI, Zhu YT, Zhou F, et al. Formation mechanism of wide stacking faults in nanocrystalline Al. Appl Phys Lett 2004;84:3564–6.

[125] Zhu YT, Liao XZ, Srinivasan SG, Zhao YH, Baskes MI, Zhou F, et al. Nucleation and growth of deformation twins in nanocrystalline aluminum. Appl Phys Lett 2004;85:5049–51.

[126] Wu XL, Liao XZ, Srinivasan SG, Zhou F, Lavernia EJ, Valiev RZ, et al. New deformation twinning mechanism generates zero macroscopic strain in nanocrystalline metals. Phys Rev Lett 2008;100:095701.

[127] Huang JY, Liao XZ, Zhu YT, Zhou F, Lavernia EJ. Grain boundary structure of nanocrystalline Cu processed by cryomilling. Philos Mag 2003;83:1407–19.

[128] Lu L, Shen YF, Chen XH, Qian LH, Lu K. Ultrahigh strength and high electrical conductivity in copper. Science 2004;304:422–6.

[129] Lu L, Schwaiger R, Shan ZW, Dao M, Lu K, Suresh S. Nano-sized twins induce high rate sensitivity of flow stress in pure copper. Acta Mater 2005;53:2169–79.

[130] Youssef KMS, Koch CC, Fedkiw PS. Influence of additives and pulse electrodeposition parameters on production of nanocrystalline zinc from zinc chloride electrolytes. J Electrochemical Soc 2004;151:C103–11.

[131] Chen XH, Lu L, Lu K. Electrical resistivity of ultrafine-grained copper with nanoscale growth twins. J Appl Phys 2007;102:083708.

[132] Cho MK, Cho JW, Wu JH, Cho JU, Choi YJ, Kim YK. Inverse Hall-Petch relation of nanostructured Ni films prepared by electrodeposition. Current Appl Phys 2010;10:57–9.

[133] Lu L, Li SX, Lu K. An abnormal strain rate effect on tensile behavior in nanocrystalline copper. Scripta Mater 2001;45:1163–9.

[134] Li HQ, Ebrahimi F. Ductile-to-brittle transition in nanocrystalline metals. Adv Mater 2005;17:1969.

[135] Li HQ, Ebrahimi F. Transition of deformation and fracture behaviors in nanostructured face-centered-cubic metals. Appl Phys Lett 2004;84:4307–9.

[136] Ebrahimi F, Ahmed Z, Li H. Effect of stacking fault energy on plastic deformation of nanocrystalline face-centered cubic metals. Appl Phys Lett 2004;85:3749–51.

[137] Wu X, Zhu YT, Chen MW, Ma E. Twinning and stacking fault formation during tensile deformation of nanocrystalline Ni. Scripta Mater 2006;54:1685–90.

[138] Wu XL, Ma E, Zhu YT. Deformation defects in nanocrystalline nickel. J Mater Sci 2007;42:1427–32.

[139] Wu XL, Narayan J, Zhu YT. Deformation twin formed by self-thickening, cross-slip mechanism in nanocrystalline Ni. Appl Phys Lett 2008;93:031910.

[140] Wu XL, Qi Y, Zhu YT. Partial-mediated slips in nanocrystalline Ni at high strain rate. Appl Phys Lett 2007;90.

[141] Wu XL, Zhu YT. Partial-dislocation-mediated processes in nanocrystalline Ni with nonequilibrium grain boundaries. Appl Phys Lett 2006;89.

[142] Wu XL, Zhu YT. Inverse grain-size effect on twinning in nanocrystalline Ni. Phys Rev Lett. 2008;101:025503-.

[143] Li HQ, Choo H, Liaw PK. The effect of temperature on strain rate sensitivity in a nanocrystalline Ni-Fe alloy. J Appl Phys. 2007;101:063536-.

[144] Liao XZ, Kilmametov AR, Valiev RZ, Gao HS, Li XD, Mukherjee AK, et al. High-pressure torsion-induced grain growth in electrodeposited nanocrystalline Ni. Appl Phys Lett. 2006;88:021909-.

[145] Liao XZ, Zhao YH, Srinivasan SG, Zhu YT, Valiev RZ, Gunderov DV. Deformation twinning in nanocrystalline copper at room temperature and low strain rate. Appl Phys Lett 2004;84:592–4.

[146] Liao XZ, Zhao YH, Zhu YT, Valiev RZ, Gunderov DV. Grain-size effect on the deformation mechanisms of nanostructured copper processed by high-pressure torsion. J Appl Phys 2004;96:636–40.

[147] Jia D, Wang YM, Ramesh KT, Ma E, Zhu YT, Valiev RZ. Deformation behavior and plastic instabilities of ultrafine-grained titanium. Appl Phys Lett 2001;79:611–3.

[148] Zhu YT, Lowe TC. Observations and issues on mechanisms of grain refinement during ECAP process. Mater Sci Eng A 2000;291:46–53.

[149] Koch CC, Youssef KM, Scattergood RO, Murty KL. Breakthroughs in optimization of mechanical properties of nanostructured metals and alloys. Adv Eng Mater 2005;7:787–94.

[150] Zhu YT, Huang JY, Gubicza J, Ungar T, Wang YM, Ma E, et al. Nanostructures in Ti processed by severe plastic deformation. J Mater Res 2003;18:1908–17.

[151] Zhu YT, Liao XZ. Nanostructured metals - Retaining ductility. Nature Mater 2004;3:351–2.

[152] Zhao YH, Zhu YT, Lavernia EJ. Strategies for Improving Tensile Ductility of Bulk Nanostructured Materials. Adv Eng Mater 2010;12:769–78.

[153] Wang YM, Ma E. Three strategies to achieve uniform tensile deformation in a nanostructured metal. Acta Mater 2004;52:1699–709.

[154] Van Swygenhoven H, Weertman JR. Preface to the viewpoint set on: mechanical properties of fully dense nanocrystalline metals. Scripta Mater 2003;49:625–7.

[155] Andreau O, Gubicza J, Zhang NX, Huang Y, Jenei P, Langdon TG. Effect of short-term annealing on the microstructures and flow properties of an Al-1% Mg alloy processed by high-pressure torsion. Mater Sci Eng A 2014;615:231–9.

[156] Zhu YT, Wu XL, Liao XZ, Narayan J, Kecskes LJ, Mathaudhu SN. Dislocation-twin interactions in nanocrystalline fcc metals. Acta Mater 2011;59:812–21.

[157] Zhao YH, Bingert JE, Liao XZ, Cui BZ, Han K, Sergueeva AV, et al. Simultaneously increasing the ductility and strength of ultra-fine-grained pure copper. Adv Mater. 2006;18:2949-+.

[158] Zhang X, Misra A, Wang H, Nastasi M, Embury JD, Mitchell TE, et al. Nanoscale-twinning-induced strengthening in austenitic stainless steel thin films. Appl Phys Lett 2004;84:1096–8.

[159] Wu XL, Youssef KM, Koch CC, Mathaudhu SN, Kecskes LJ, Zhu YT. Deformation twinning in a nanocrystalline hcp Mg alloy. Scripta Mater 2011;64:213–6.

[160] Zhao YH, Zhu YT, Liao XZ, Horita Z, Langdon TG. Tailoring stacking fault energy for high ductility and high strength in ultrafine grained Cu and its alloy. Appl Phys Lett. 2006;89:121906-.

[161] Ni S, Wang YB, Liao XZ, Li HQ, Figueiredo RB, Ringer SP, et al. Effect of grain size on the competition between twinning and detwinning in nanocrystalline metals. Phys Rev B 2011;84:235401.

[162] Zhao YH, Liao XZ, Zhu YT, Horita Z, Langdon TG. Influence of stacking fault energy on nanostructure formation under high pressure torsion. Mater Sci Eng A 2005;410:188–93.

[163] Zhao YH, Liao XZ, Horita Z, Langdon TG, Zhu YT. Determining the optimal stacking fault energy for achieving high ductility in ultrafine-grained Cu-Zn alloys. Mater Sci Eng A 2008;493:123–9.

[164] Zhao YH, Topping T, Bingert JF, Thornton JJ, Dangelewicz AM, Li Y, et al. High tensile ductility and strength in bulk nanostructured nickel. Adv Mater 2008; 20:3028–33.
[165] Zhao YH, Bingert JF, Zhu YT, Liao XZ, Valiev RZ, Horita Z, et al. Tougher ultrafine grain Cu via high-angle grain boundaries and low dislocation density. Appl Phys Lett. 2008;92:081903-.
[166] Jian WW, Cheng GM, Xu WZ, Yuan H, Tsai MH, Wang QD, et al. Ultrastrong Mg Alloy via Nano-spaced Stacking Faults. Mater Res Lett 2013;1:61–6.
[167] Jian WW, Cheng GM, Xu WZ, Koch CC, Wang QD, Zhu YT, et al. Physics and model of strengthening by parallel stacking faults. Appl Phys Lett 2013;103.
[168] Liddicoat PV, Liao XZ, Zhao YH, Zhu YT, Murashkin MY, Lavernia EJ, et al. Nanostructural hierarchy increases the strength of aluminum alloys. Nature Comm 2010;1:63.
[169] Tellkamp VL, Melmed A, Lavernia EJ. Mechanical behavior and microstructure of a thermally stable bulk nanostructured Al alloy. Metallurgical and Materials Transactions a-Physical Metallurgy and Materials Science 2001;32:2335–43.
[170] Wu XL, Zhu YT, Wei YG, Wei Q. Strong Strain Hardening in Nanocrystalline Nickel. Phys Rev Lett. 2009;103:205504-.
[171] Agnew SR, Horton JA, Lillo TM, Brown DW. Enhanced ductility in strongly textured magnesium produced by equal channel angular processing. Scripta Mater 2004;50:377–81.
[172] Choi HJ, Kim Y, Shin JH, Bae DH. Deformation behavior of magnesium in the grain size spectrum from nano- to micrometer. Mater Sci Eng A 2010;527: 1565–70.
[173] Li JZ, Xu W, Wu XL, Ding H, Xia KN. Effects of grain size on compressive behaviour in ultrafine grained pure Mg processed by equal channel angular pressing at room temperature. Mater Sci Eng A 2011;528:5993–8.
[174] Ma AB, Jiang JH, Saito N, Shigematsu I, Yuan YC, Yang DH, et al. Improving both strength and ductility of a Mg alloy through a large number of ECAP passes. Mater Sci Eng A 2009;513–14:122–7.
[175] Yamashita A, Horita Z, Langdon TG. Improving the mechanical properties of magnesium and a magnesium alloy through severe plastic deformation. Mater Sci Eng A 2001;300:142–7.
[176] Yoshida Y, Arai K, Itoh S, Kamado S, Kojima Y. Realization of high strength and high ductility for AZ61 magnesium alloy by severe warm working. Sci Tech Adv Mater 2005;6:185–94.
[177] Jia D, Ramesh KT, Ma E. Effects of nanocrystalline and ultrafine grain sizes on constitutive behavior and shear bands in iron. Acta Mater 2003;51:3495–509.
[178] Malow TR, Koch CC, Miraglia PQ, Murty KL. Compressive mechanical behavior of nanocrystalline Fe investigated with an automated ball indentation technique. Mater Sci Eng A 1998;252:36–43.
[179] Wei Q, Kecskes L, Jiao T, Hartwig KT, Ramesh KT, Ma E. Adiabatic shear banding in ultrafine-grained Fe processed by severe plastic deformation. Acta Mater 2004;52:1859–69.
[180] Wei Q, Pan ZL, Wu XL, Schuster BE, Kecskes LJ, Valiev RZ. Microstructure and mechanical properties at different length scales and strain rates of nanocrystalline tantalum produced by high-pressure torsion. Acta Mater 2011;59:2423–36.
[181] Zhu YT, Wu XL. Perspective on heterogeneous deformation induced (HDI) hardening and back stress. Mater Res Lett 2019;7:393–8.
[182] Li JG, Zhang Q, Huang RR, Li XY, Gao HJ. Towards understanding the structure-property relationships of heterogeneous-structured materials. Scr Mater 2020; 186:304–11.
[183] Han BQ, Huang JY, Zhu YT, Lavernia EJ. Strain rate dependence of properties of cryomilled bimodal 5083 Al alloys. Acta Mater 2006;54:3015–24.
[184] Han BQ, Lee Z, Witkin D, Nutt S, Lavernia EJ. Deformation behavior of bimodal nanostructured 5083 Al alloys. Metall Mater Trans A. 2005;36a:957-65.
[185] Lu K. Making strong nanomaterials ductile with gradients. Science 2014;345:1455–6.
[186] Chen AY, Liu JB, Wang HT, Lu J, Wang YM. Gradient twinned 304 stainless steels for high strength and high ductility. Mater Sci Eng A 2016;667:179–88.
[187] Wei YJ, Li YQ, Zhu LC, Liu Y, Lei XQ, Wang G, et al. Evading the strength- ductility trade-off dilemma in steel through gradient hierarchical nanotwins. Nature Comm 2014;5:1–8.
[188] Calcagnotto M, Adachi Y, Ponge D, Raabe D. Deformation and fracture mechanisms in fine- and ultrafine-grained ferrite/martensite dual-phase steels and the effect of aging. Acta Mater 2011;59:658–70.
[189] Li ZM, Pradeep KG, Deng Y, Raabe D, Tasan CC. Metastable high-entropy dual-phase alloys overcome the strength-ductility trade-off. Nature 2016;534:227–30.
[190] Park K, Nishiyama M, Nakada N, Tsuchiyama T, Takaki S. Effect of the martensite distribution on the strain hardening and ductile fracture behaviors in dual-phase steel. Mater Sci Eng A 2014;604:135–41.
[191] Llorca J, Needleman A, Suresh S. The Bauschinger Effect in Whisker-Reinforced Metal-Matrix Composites. Scripta Metall Mater 1990;24:1203–8.
[192] Thilly L, Van Petegem S, Renault PO, Lecouturier F, Vidal V, Schmitt B, et al. A new criterion for elasto-plastic transition in nanomaterials: Application to size and composite effects on Cu-Nb nanocomposite wires. Acta Mater 2009;57:3157–69.
[193] Tanaka K, Mori T. Hardening of Crystals by Non-Deforming Particles and Fibres. Acta Metall 1970;18:931–1000.
[194] Nie JF, Chen YY, Chen X, Liu XF, Liu GL, Zhao YH, et al. Stiff, strong and ductile heterostructured aluminum composites reinforced with oriented nanoplatelets. Scr Mater 2020;189:140–4.
[195] Han QH, Asgari A, Hodgson PD, Stanford N. Strain partitioning in dual-phase steels containing tempered martensite. Mater Sci Eng A 2014;611:90–9.
[196] Zhu YT, Liao XZ, Srinivasan SG, Lavernia EJ. Nucleation of deformation twins in nanocrystalline face-centered-cubic metals processed by severe plastic deformation. J Appl Phys. 2005;98:034319-.
[197] Brandes EA, Smithells BGB. Metals Reference Book. Seventh. Edition ed. Oxford: Butterworth-Heinemann Ltd; 1992.
[198] Wang YF, Huang CX, He Q, Guo FJ, Wang MS, Song LY, et al. Heterostructure induced dispersive shear bands in heterostructured Cu. Scr Mater 2019;170: 76–80.
[199] Tasan CC, Diehl M, Yan D, Zambaldi C, Shanthraj P, Roters F, et al. Integrated experimental-simulation analysis of stress and strain partitioning in multiphase alloys. Acta Mater 2014;81:386–400.
[200] Cong ZH, Jia N, Sun X, Ren Y, Almer J, Wang YD. Stress and Strain Partitioning of Ferrite and Martensite during Deformation. Metall Mater Trans A. 2009;40a: 1383-7.
[201] Ryu JH, Kim DI, Kim HS, Bhadeshia HKDH, Suh DW. Strain partitioning and mechanical stability of retained austenite. Scripta Mater 2010;63:297–9.
[202] Feaugas X. On the origin of the tensile flow stress in the stainless steel AISI 316L at 300 K: Back stress and effective stress. Acta Mater 1999;47:3617–32.
[203] Fournier B, Sauzay M, Caes C, Noblecourt M, Mottot M. Analysis of the hysteresis loops of a martensitic steel - Part I: Study of the influence of strain amplitude and temperature under pure fatigue loadings using an enhanced stress partitioning method. Mater Sci Eng A 2006;437:183–96.
[204] Helbert AL, Feaugas X, Clavel M. Effects of microstructural parameters and back stress on damage mechanisms in alpha/beta titanium alloys. Acta Mater 1998; 46:939–51.
[205] Hong SI, Laird C. Cyclic Deformation-Behavior of Cu-16at-Percent Al Single-Crystals. 3. Friction Stress and Back Stress Behavior. Mater Sci Eng A 1990;128: 155–69.
[206] Kato H, Moat R, Mori T, Sasaki K, Withers P. Back Stress Work Hardening Confirmed by Bauschinger Effect in a TRIP Steel Using Bending Tests. ISIJ Int 2014; 54:1715–8.
[207] Kuhlmann-Wilsdorf D, Laird C. Dislocation Behavior in Fatigue. 2. Friction Stress and Back Stress as Inferred from an Analysis of Hysteresis Loops. Mater Sci Eng 1979;37:111–20.
[208] Li JS, Cao Y, Gao B, Li YS, Zhu YT. Superior strength and ductility of 316L stainless steel with heterogeneous lamella structure. J Mater Sci 2018;53:10442–56.
[209] Roters F, Eisenlohr P, Hantcherli L, Tjahjanto DD, Bieler TR, Raabe D. Overview of constitutive laws, kinematics, homogenization and multiscale methods in crystal plasticity finite-element modeling: Theory, experiments, applications. Acta Mater 2010;58:1152–211.
[210] Bayley CJ, Brekelmans WAM, Geers MGD. A comparison of dislocation induced back stress formulations in strain gradient crystal plasticity. Int J Solids Struct 2006;43:7268–86.
[211] Huang Y, Gao H, Nix WD, Hutchinson JW. Mechanism-based strain gradient plasticity – II. Analysis. J Mech Phys Solids 2000;48:99–128.
[212] Nabarro FRN. Sequences of dislocation patterns. Mater Sci Eng A 2001;317:12–6.

[213] Cottrell AH. Dislocations and Plastic Flow in Crystals. London: Oxford University Press; 1953.
[214] Hirth JP, Lothe J. Theory of Dislocations. 2nd ed. Malabar, FL: Krieger Publishing Company; 1992.
[215] Abel A, Muir H. Bauschinger Effect and Discontinuous Yielding. Philos Mag 1972;26:489–1000.
[216] Kishi T, Gokyu I. New Relationship between Pre-Strain and Yield Stress Drop Due to Bauschinger Effect. Metall Trans 1973;4:390–2.
[217] Moan GD, Embury JD. Study of the Bauschinger Effect in Al-Cu Alloys. Acta Metall 1979;27:903–14.
[218] Liu XL, Yuan FP, Zhu YT, Wu XL. Extraordinary Bauschinger effect in gradient structured copper. Scr Mater 2018;150:57–60.
[219] Mughrabi H. Dislocation Wall and Cell Structures and Long-Range Internal-Stresses in Deformed Metal Crystals. Acta Metall 1983;31:1367–79.
[220] Mughrabi H. On the role of strain gradients and long-range internal stresses in the composite model of crystal plasticity. Mater Sci Eng A 2001;317:171–80.
[221] Mughrabi H. The effect of geometrically necessary dislocations on the flow stress of deformed crystals containing a heterogeneous dislocation distribution. Mater Sci Eng A 2001;319:139–43.
[222] Mughrabi H. On the current understanding of strain gradient plasticity. Mater Sci Eng A 2004;387:209–13.
[223] Delobelle P, Oytana C. The Study of the Laws of Behavior at High-Temperature, in Plasticity-Flow, of an Austenitic Stainless-Steel (17–12-Sph). J Nucl Mater 1986;139:204–27.
[224] Risbet M, Feaugas X, Clavel M. Study of the cyclic softening of an under-aged gamma'-precipitated nickel-base superalloy (Waspaloy). J Physique Iv 2001;11:293–301.
[225] Guillemer-Neel C, Feaugas X, Clavel M. Mechanical behavior and damage kinetics in nodular cast iron: part II. Hardening and damage Metall Trans A 2000;31:3075–85.
[226] Morrison DJ, Jia Y, Moosbrugger JC. Cyclic plasticity of nickel at low plastic strain amplitude: hysteresis loop shape analysis. Mater Sci Eng A 2001;314:24–30.
[227] Dickson JI, Boutin J, Handfield L. A comparison of two simple methods for measuring cyclical internal and effective stresses. Mater Sci Eng 1984;64:L7–11.
[228] Calcagnotto M, Ponge D, Demir E, Raabe D. Orientation gradients and geometrically necessary dislocations in ultrafine grained dual-phase steels studied by 2D and 3D EBSD. Mater Sci Eng A 2010;527:2738–46.
[229] Kubin LP, Mortensen A. Geometrically necessary dislocations and strain-gradient plasticity: a few critical issues. Scr Mater 2003;48:119–25.
[230] Wilkinson AJ, Randman D. Determination of elastic strain fields and geometrically necessary dislocation distributions near nanoindents using electron back scatter diffraction. Philos Mag 2010;90:1159–77.
[231] Demir E, Raabe D, Zaafarani N, Zaefferer S. Investigation of the indentation size effect through the measurement of the geometrically necessary dislocations beneath small indents of different depths using EBSD tomography. Acta Mater 2009;57:559–69.
[232] Gao HJ, Huang YG. Geometrically necessary dislocation and size-dependent plasticity. Scr Mater 2003;48:113–8.
[233] Zhang Y, Cheng Z, Lu L, Zhu T. Strain gradient plasticity in gradient structured metals. J Mech Phys Solids 2020;140.
[234] Cheng Z, Bu LF, Zhang Y, Wu HA, Zhu T, Gao HJ, et al. Unraveling the origin of extra strengthening in gradient nanotwinned metals. Proc Natl Acad Sci USA 2022;119:119.
[235] Ozturk T, Mirmesdagh J, Ediz T. Strain Partitioning and Plastic-Flow in Some Metal-Metal Laminates. Mater Sci Eng A 1994;175:125–9.
[236] Wang MM, Tasan CC, Ponge D, Dippel AC, Raabe D. Nanolaminate transformation-induced plasticity-twinning-induced plasticity steel with dynamic strain partitioning and enhanced damage resistance. Acta Mater 2015;85:216–28.
[237] Li JC. High-Angle Tilt Boundary - a Dislocation Core Model. J Appl Phys 1961;32:525–30.
[238] Murr LE. Dislocation Ledge Sources: Dispelling the Myth of Frank-Read Source Importance. Metall Mater Trans A. 2016;47a:5811-26.
[239] Zhu YT, Wu XL, Liao XZ, Narayan J, Mathaudhu SN, Kecskes LJ. Twinning partial multiplication at grain boundary in nanocrystalline fcc metals. Appl Phys Lett. 2009;95:031909 -.
[240] Zhou H, Huang CX, Sha XC, Xiao LR, Ma XL, Hoppel HW, et al. In-situ observation of dislocation dynamics near heterostructured interfaces. Mater Res Lett 2019;7:376–82.
[241] Wang YF, Huang CX, Fang XT, Hoppel HW, Goken M, Zhu YT. Hetero-deformation induced (HDI) hardening does not increase linearly with strain gradient. Scr Mater 2020;174:19–23.
[242] Wang YF, Huang CX, Li YS, Guo FJ, He Q, Wang MS, et al. Dense dispersed shear bands in gradient-structured Ni. Int J Plasticity 2020;124:186–98.
[243] Wu H, Fan GH. An overview of tailoring strain delocalization for strength-ductility synergy. Prog Mater Sci 2020;113.
[244] Wang X, Li YS, Zhang Q, Zhao YH, Zhu YT. Gradient Structured Copper by Rotationally Accelerated Shot Peening. J Mater Sci Tech 2017;33:758–61.
[245] Zhang K, Weertman JR, Eastman JA. Rapid stress-driven grain coarsening in nanocrystalline Cu at ambient and cryogenic temperatures. Appl Phys Lett. 2005;87:061921-.
[246] Brandstetter S, Zhang K, Escuadro A, Weertman JR, Van Swygenhoven H. Grain coarsening during compression of bulk nanocrystalline nickel and copper. Scripta Mater 2008;58:61–4.
[247] Fan GJ, Fu LF, Qiao DC, Choo H, Liaw PK, Browning ND. Grain growth in a bulk nanocrystalline Co alloy during tensile plastic deformation. Scripta Mater 2006;54:2137–41.
[248] Fan GJ, Fu LF, Choo H, Liaw PK, Browning ND. Uniaxial tensile plastic deformation and grain growth of bulk nanocrystalline alloys. Acta Mater 2006;54:4781–92.
[249] Li L, Ungar T, Wang YD, Fan GJ, Yang YL, Jia N, et al. Simultaneous reductions of dislocation and twin densities with grain growth during cold rolling in a nanocrystalline Ni-Fe alloy. Scripta Mater 2009;60:317–20.
[250] Liu YF, Cao Y, Mao QZ, Zhou H, Zhao YH, Jiang W, et al. Critical microstructures and defects in heterostructured materials and their effects on mechanical properties. Acta Mater 2020;189:129–44.
[251] Fang XT, He GZ, Zheng C, Ma XL, Kaoumi D, Li YS, et al. Effect of heterostructure and hetero-deformation induced hardening on the strength and ductility of brass. Acta Mater 2020;186:644–55.
[252] Liu SS, Wang WZ, Chen X, Huang GS, Liu H, Tang AT, et al. Enhanced strength and ductility AZ91 alloy with heterogeneous lamella structure prepared by pre-aging and low-temperature extrusion. Mater Sci Eng A 2021;812.
[253] Slone CE, Miao J, George EP, Mills MJ. Achieving ultra-high strength and ductility in equiatomic CrCoNi with partially recrystallized microstructures. Acta Mater 2019;165:496–507.
[254] Wu SW, Wang G, Wang Q, Jia YD, Yi J, Zhai QJ, et al. Enhancement of strength-ductility trade-off in a high-entropy alloy through a heterogeneous structure. Acta Mater 2019;165:444–58.
[255] Su J, Raabe D, Li ZM. Hierarchical microstructure design to tune the mechanical behavior of an interstitial TRIP-TWIP high-entropy alloy. Acta Mater 2019;163:40–54.
[256] Li WP, Chou TH, Yang T, Chuang WS, Huang JC, Luan JH, et al. Design of ultrastrong but ductile medium-entropy alloy with controlled precipitations and heterogeneous grain structures. Appl Mater Today 2021;23.
[257] Du XH, Li WP, Chang HT, Yang T, Duan GS, Wu BL, et al. Dual heterogeneous structures lead to ultrahigh strength and uniform ductility in a Co-Cr-Ni medium-entropy alloy. Nat Commun 2020;11.
[258] Zhang C, Zhu CY, Cao PH, Wang X, Ye F, Kaufmann K, et al. Aged metastable high-entropy alloys with heterogeneous lamella structure for superior strength-ductility synergy. Acta Mater 2020;199:602–12.
[259] Xie YH, Liang JM, Zhang DL, Luo YF, Zhang Z, Liu Y, et al. Sustaining strength-ductility synergy of CoCrFeNiMn high entropy alloy by a multilevel heterogeneity associated with nanoparticles. Scr Mater 2020;187:390–4.
[260] Li ZK, Fang XT, Wang YF, Jiang P, Wang JJ, Liu CM, et al. Tuning heterostructures with powder metallurgy for high synergistic strengthening and hetero-deformation induced hardening. Mater Sci Eng A 2020;777:139074.
[261] Wu XL, Zhu YT, Lu K. Ductility and strain hardening in gradient and lamellar structured materials. Scr Mater 2020;186:321–5.
[262] Lu K. Stabilizing nanostructures in metals using grain and twin boundary architectures. Nat Rev Mater 2016;1.

[263] Chen G, Qiao JW, Jiao ZM, Zhao D, Zhang TW, Ma SG, et al. Strength-ductility synergy of Al0.1CoCrFeNi high-entropy alloys with gradient hierarchical structures. Scr Mater 2019;167:95–100.
[264] Roumina R, Embury JD, Bouaziz O, Zurob HS. Mechanical behavior of a compositionally graded 300M steel. Mater Sci Eng A 2013;578:140–9.
[265] Lu K, Lu J. Surface nanocrystallization (SNC) of metallic materials-presentation of the concept behind a new approach. J Mater Sci Technol 1999;15:193–7.
[266] Wang G, Ouyang H, Su YS, Guo Q, Xiong DB, Zhuang QD, et al. Heterostructured bulk aluminum with controllable gradient structure: Fabrication strategy and deformation mechanisms. Scr Mater 2021;196.
[267] Li XY, Lu L, Li JG, Zhang X, Gao HJ. Mechanical properties and deformation mechanisms of gradient nanostructured metals and alloys. Nat Rev Mater 2020;5:706–23.
[268] Kou HN, Lu J, Li Y. High-Strength and High-Ductility Nanostructured and Amorphous Metallic Materials. Adv Mater 2014;26:5518–24.
[269] Lin Y, Pan J, Zhou HF, Gao HJ, Li Y. Mechanical properties and optimal grain size distribution profile of gradient grained nickel. Acta Mater 2018;153:279–89.
[270] Liu XW, Sun LG, Zhu LL, Liu JB, Lu K, Lu J. High-order hierarchical nanotwins with superior strength and ductility. Acta Mater 2018;149:397–406.
[271] Kang JY, Kim JG, Park HW, Kim HS. Multiscale architectured materials with composition and grain size gradients manufactured using high-pressure torsion. Sci Rep-Uk 2016;6:26590.
[272] Zeng Z, Li XY, Xu DS, Lu L, Gao HJ, Zhu T. Gradient plasticity in gradient nano-grained metals. Extreme Mech Lett 2016;8:213–9.
[273] Li JJ, Weng GJ, Chen SH, Wu XL. On strain hardening mechanism in gradient nanostructures. Int J Plasticity 2017;88:89–107.
[274] Fang TH, Tao NR, Lu K. Tension-induced softening and hardening in gradient nanograined surface layer in copper. Scripta Mater 2014;77:17–20.
[275] Wu XL, Yang MX, Yuan FP, Chen L, Zhu YT. Combining gradient structure and TRIP effect to produce austenite steel with high strength and ductility. Acta Mater 2016;112:337–46.
[276] Wang YF, Guo FJ, He Q, Song LY, Wang MS, Huang AH, et al. Synergetic deformation-induced deformation-induced extraordinary softening and hardening in gradient copper. Mater Sci Eng A 2019;752:217–22.
[277] Liu YF, Cao Y, Zhou H, Chen XF, Liu Y, Xiao LR, et al. Mechanical Properties and Microstructures of Commercial-Purity Aluminum Processed by Rotational Accelerated Shot Peening Plus Cold Rolling. Adv Eng Mater 2020;22.
[278] Moon JH, Baek SM, Lee SG, Seong Y, Amanov A, Lee S, et al. Effects of residual stress on the mechanical properties of copper processed using ultrasonic-nanocrystalline surface modification. Mater Res Lett 2019;7:97–102.
[279] Chan HL, Ruan HH, Chen AY, Lu J. Optimization of the strain rate to achieve exceptional mechanical properties of 304 stainless steel using high speed ultrasonic surface mechanical attrition treatment. Acta Mater 2010;58:5086–96.
[280] Jamalian M, Field DP. Effect of gradient microstructures on strengthening and toughening of AZ31. Mater Sci Eng A 2020;771.
[281] Li WL, Tao NR, Lu K. Fabrication of a gradient nano-micro-structured surface layer on bulk copper by means of a surface mechanical grinding treatment. Scripta Mater 2008;59:546–9.
[282] Ding J, Li Q, Li J, Xue S, Fan Z, Wang H, et al. Mechanical behavior of structurally gradient nickel alloy. Acta Mater 2018;149:57–67.
[283] Lei YB, Wang ZB, Xu JL, Lu K. Simultaneous enhancement of stress- and strain-controlled fatigue properties in 316L stainless steel with gradient nanostructure. Acta Mater 2019;168:133–42.
[284] Shao CW, Zhang P, Zhu YK, Zhang ZJ, Tian YZ, Zhang ZF. Simultaneous improvement of strength and plasticity: Additional work-hardening from gradient microstructure. Acta Mater 2018;145:413–28.
[285] Shao CW, Zhang P, Wang XG, Wang Q, Zhang ZF. High-cycle fatigue behavior of TWIP steel with graded grains: breaking the rule of mixture. Mater Res Lett 2019;7:26–32.
[286] Cai SL, Wan JC, Hao YJ, Koch CC. Dual gradient microstructure to simultaneously improve strength and electrical conductivity of aluminum wire. Mater Sci Eng A 2020;783.
[287] Yang L, Chen Z, Ma XK, Zhong DL, Zhao XJ, Xiao L, et al. Improvement of strength and ductility in a gradient structured Ni fabricated by severe torsion deformation. Mater Sci Eng A 2021;826.
[288] Yan JW, Ma JW, Wang J, Shen Y. Strength and Ductility with Dual Grain-Size and Texture Gradients in AZ31 Mg Alloy. Metall Mater Trans A. 2018;49a:5333-8.
[289] Mao QZ, Chen X, Li JS, Zhao YH. Nano-Gradient Materials Prepared by Rotary Swaging. Nanomaterials-Basel 2021;11.
[290] Chen X, Liu CM, Wan YC, Jiang SN, Chen ZY, Zhao YH. Grain Refinement Mechanisms in Gradient Nanostructured AZ31B Mg Alloy Prepared via Rotary Swaging. Metall Mater Trans A 2021;52:4053–65.
[291] Guo FJ, Wang YF, Wang MS, He Q, Ran H, Huang CX, et al. Hetero-deformation induced strengthening and toughening of pure iron with inverse and multi-gradient structures. Mater Sci Eng A 2020;782.
[292] Lee HH, Yoon JI, Park HK, Kim HS. Unique microstructure and simultaneous enhancements of strength and ductility in gradient-microstructured Cu sheet produced by single-roll angular-rolling. Acta Mater 2019;166:638–49.
[293] Wang X, Jiang L, Cooper C, Yu KH, Zhang DL, Rupert TJ, et al. Toughening magnesium with gradient twin meshes. Acta Mater 2020;195:468–81.
[294] Moering J, Ma XL, Chen GZ, Miao PF, Li GZ, Qian G, et al. The role of shear strain on texture and microstructural gradients in low carbon steel processed by Surface Mechanical Attrition Treatment. Scripta Mater 2015;108:100–3.
[295] Chen LB, Cao TH, Wei R, Tang K, Xin C, Jiang F, et al. Gradient structure design to strengthen carbon interstitial Fe40Mn40Co10Cr10 high entropy alloys. Materials Science and Engineering a-Structural Materials Properties Microstructure and Processing 2020;772.
[296] Cao RQ, Yu Q, Pan J, Lin Y, Sweet A, Li Y, et al. On the exceptional damage-tolerance of gradient metallic materials. Mater Today 2020;32:94–107.
[297] Long QY, Lu JX, Fang TH. Microstructure and mechanical properties of AISI 316L steel with an inverse gradient nanostructure fabricated by electro-magnetic induction heating. Mater Sci Eng A 2019;751:42–50.
[298] Chen W, You ZS, Tao NR, Jin ZH, Lu L. Mechanically-induced grain coarsening in gradient nano-grained copper. Acta Mater 2017;125:255–64.
[299] Yang MX, Li RG, Jiang P, Yuan FP, Wang YD, Zhu YT, et al. Residual stress provides significant strengthening and ductility in gradient structured materials. Mater Res Lett 2019;7:433–8.
[300] Yang JR, Xu L, Gao HL, Li XF, Pan HJ, Shu BP, et al. Effect of global constraint on the mechanical behavior of gradient materials. Mater Sci Eng A 2021;826.
[301] Yang XC, Ma XL, Moering J, Zhou H, Wang W, Gong YL, et al. Influence of gradient structure volume fraction on the mechanical properties of pure copper. Materials Science and Engineering a-Structural Materials Properties Microstructure and Processing 2015;645:280–5.
[302] Ross CA. Electrodeposited Multilayer Thin-Films. Annual Rev Mater Sci 1994;24:159–88.
[303] Bakonyi I, Peter L. Electrodeposited multilayer films with giant magnetoresistance (GMR): Progress and problems. Prog Mater Sci 2010;55:107–245.
[304] Barnett SA, Shinn M. Plastic and Elastic Properties of Compositionally Modulated Thin-Films. Annual Rev Mater Sci 1994;24:481–511.
[305] Smith DL, Hoffman DW. Thin-Film Deposition: Principles and Practice Phys Today 1996;49:60.
[306] Jankowski AF. Metallic multilayers at the nanoscale. Nanostruct Mater 1995;6:179–90.
[307] Ohring M. Materials Science of Thin Films. 2nd Ed. ed. San Diego: Academic Press; 2002.
[308] Seshan K. Handbook of thin film deposition. 3rd Ed. ed. Norwich, NY: William Andrew; 2012.
[309] Emmerson CM, Shen TH, Evans SD, Allinson H. A combined in situ optical reflectance-electron diffraction study of Co/Cu and Co/Au multilayers grown by molecular beam epitaxy. Appl Phys Lett 1996;68:3740–2.
[310] Westerwaal RJ, Slaman M, Broedersz CP, Borsa DM, Dam B, Griessen R, et al. Optical, structural, and electrical properties of Mg2NiH4 thin films in situ grown by activated reactive evaporation. J Appl Phys 2006;100:063518.
[311] Nizolek T, Beyerlein IJ, Mara NA, Avallone JT, Pollock TM. Tensile behavior and flow stress anisotropy of accumulative roll bonded Cu-Nb nanolaminates. Appl Phys Lett 2016;108:051903.
[312] Mara NA, Beyerlein IJ. Interface-dominant multilayers fabricated by severe plastic deformation: Stability under extreme conditions. Curr Opin Solid St M 2015;19:265–76.
[313] Beyerlein IJ, Wang J. Interface-driven mechanisms in cubic/noncubic nanolaminates at different scales. Mrs Bull 2019;44:31–9.

[314] Pathak S, Velisavljevic N, Baldwin JK, Jain M, Zheng SJ, Mara NA, et al. Strong, Ductile, and Thermally Stable bcc-Mg Nanolaminates. Sci Rep-Uk 2017;7:8264.

[315] Subedi S, Beyerlein IJ, Lesar R, Rollett AD. Strengt of nanoscale metallic multilayers. Scr Mater 2018;145:132–6.

[316] Yang WF, Beyerlein IJ, Jin QQ, Ge HL, Xiong T, Yang LX, et al. Strength and ductility of bulk Cu/Nb nanolaminates exposed to extremely high temperatures. Scr Mater 2019;166:73–7.

[317] Ardeljan M, Knezevic M, Jain M, Pathak S, Kumar A, Li N, et al. Room temperature deformation mechanisms of Mg/Nb nanolayered composites. J Mater Res 2018;33:1311–32.

[318] Saito Y, Utsunomiya H, Tsuji N, Sakai T. Novel ultra-high straining process for bulk materials - Development of the accumulative roll-bonding (ARB) process. Acta Mater 1999;47:579–83.

[319] Lim SCV, Rollett AD. Length scale effects on recrystallization and texture evolution in Cu layers of a roll-bonded Cu-Nb composite. Mater Sci Eng A 2009;520:189–96.

[320] Carpenter JS, Vogel SC, LeDonne JE, Hammon DL, Beyerlein IJ, Mara NA. Bulk texture evolution of Cu-Nb nanolamellar composites during accumulative roll bonding. Acta Mater 2012;60:1576–86.

[321] Wang J, Kang K, Zhang RF, Zheng SJ, Beyerlein IJ, Mara NA. Structure and Property of Interfaces in ARB Cu/Nb Laminated Composites. Jom 2012;64:1208–17.

[322] Ardeljan M, Savage DJ, Kumar A, Beyerlein IJ, Knezevic M. The plasticity of highly oriented nano-layered Zr/Nb composites. Acta Mater 2016;115:189–203.

[323] Savage DJ, Beyerlein IJ, Mara NA, Vogel SC, McCabe RJ, Knezevic M. Microstructure and texture evolution in Mg/Nb layered materials made by accumulative roll bonding. Int J Plasticity 2020;125:1–26.

[324] Zeng LF, Gao R, Fang QF, Wang XP, Xie ZM, Miao S, et al. High strength and thermal stability of bulk Cu/Ta nanolamellar multilayers fabricated by cross accumulative roll bonding. Acta Mater 2016;110:341–51.

[325] Yasuda A, Kikuchi S. Effect of annealing on the strength of Ag/Fe and Ag/Ni super-laminates produced by foil metallurgy. Mater Sci Eng A 2004;387:783–8.

[326] Carpenter JS, Nizolek T, McCabe RJ, Knezevic M, Zheng SJ, Eftink BP, et al. Bulk texture evolution of nanolamellar Zr-Nb composites processed via accumulative roll bonding. Acta Mater 2015;92:97–108.

[327] Leu B, Savage DJ, Wang JX, Alam ME, Mara NA, Kumar MA, et al. Processing of Dilute Mg-Zn-Mn-Ca Alloy/Nb Multilayers by Accumulative Roll Bonding. Adv Eng Mater 2020;22:1900673.

[328] Li Y, Zhao YH, Ortalan V, Liu W, Zhang ZH, Vogt RG, et al. Investigation of aluminum-based nanocomposites with ultra-high strength. Mater Sci Eng, A 2009;527:305–16.

[329] Ye RQ, Han BQ, Lavernia EJ. Simulation of deformation and failure process in bimodal Al alloys. Metall Mater Trans A. 2005;36a:1833-40.

[330] Fan GJ, Choo H, Liaw PK, Lavernia EJ. Plastic deformation and fracture of ultrafine-grained Al-Mg alloys with a bimodal grain size distribution. Acta Mater 2006;54:1759–66.

[331] Pao PS, Jones HN, Feng CR, Witkin DB, Lavernia EJ. Fatigue and fracture in bimodal Al 5083. Ultrafine Grained Materials IV 2006:331–6.

[332] Ovid'ko IA, Sheinerman AG. Plastic deformation and fracture processes in metallic and ceramic nanomaterials with bimodal structures. Rev Adv Mater Sci 2007;16:1–9.

[333] Zhao MC, Hanamura T, Yin FX, Qiu H, Nagai K. Formation of bimodal-sized structure and its tensile properties in a warm-rolled and annealed ultrafine-grained Ferrite/Cementite steel. Metall Mater Trans A 2008;39A:1691–701.

[334] Hoeppel HW, Korn M, Lapovok R, Mughrabi H. Bimodal grain size distributions in UFG materials produced by SPD: Their evolution and effect on mechanical properties. 15th Int Conf on the Strength of Materials (Icsma-15). 2010;240.

[335] Orlov D, Todaka Y, Umemoto M, Tsuji N. Formation of bimodal grain structures in high purity Al by reversal high pressure torsion. Scripta Mater 2011;64:498–501.

[336] Zhang Z, Orlov D, Vajpai SK, Tong B, Ameyama K. Importance of Bimodal Structure Topology in the Control of Mechanical Properties of a Stainless Steel. Adv Eng Mater 2015;17:791–5.

[337] Ye J, Han BQ, Lee Z, Ahn B, Nutt SR, Schoenung JM. A tri-modal aluminum based composite with super-high strength. Scr Mater 2005;53:481–6.

[338] Jiang L, Ma KK, Yang H, Li MJ, Lavernia EJ, Schoenung JM. The Microstructural Design of Trimodal Aluminum Composites. JOM 2014;66:898–908.

[339] Ertorer O, Topping T, Li Y, Moss W, Lavernia EJ. Enhanced tensile strength and high ductility in cryomilled commercially pure titanium. Scr Mater 2009;60:586–9.

[340] Guo DF, Li M, Shi YD, Zhang ZB, Zhang HT, Liu XM, et al. Effect of strain rate on microstructure evolutions and mechanical properties of cryorolled Zr upon annealing. Mater Lett 2012;66:305–7.

[341] Edalati K, Furuta T, Daio T, Kuramoto S, Horita Z. High Strength and High Uniform Ductility in a Severely Deformed Iron Alloy by Lattice Softening and Multimodal-structure Formation. Mater Res Lett 2015;3:197–202.

[342] Sekiguchi T, Ono K, Fujiwara H, Ameyama K. New Microstructure Design for Commercially Pure Titanium with Outstanding Mechanical Properties by Mechanical Milling and Hot Roll Sintering. Mater Trans 2010;51:39–45.

[343] Ota M, Vajpai SK, Imao R, Kurokawa K, Ameyama K. Application of High Pressure Gas Jet Mill Process to Fabricate High Performance Harmonic Structure Designed Pure Titanium. Mater Trans 2015;56:154–9.

[344] Nagata M, Horikawa N, Kawabata M, Ameyama K. Effects of Microstructure on Mechanical Properties of Harmonic Structure Designed Pure Ni. Mater Trans 2019;60:1914–20.

[345] Ota M, Shimojo K, Okada S, Vajpai SK, Ameyama K. Harmonic Structure Design and Mechanical Properties of Pure Ni Compact. J Powder Metall Min 2014;3:1000122.

[346] Vajpai SK, Ota M, Watanabe T, Maeda R, Sekiguchi T, Kusaka T, et al. The Development of High Performance Ti-6Al-4V Alloy via a Unique Microstructural Design with Bimodal Grain Size Distribution. Metall Mater Trans A 2015;46A:903–14.

[347] Khalil NZ, Vajpai SK, Ota M, Ameyama K. Application of Al-Si Semi-Solid Reaction for Fabricating Harmonic Structured Al Based Alloy. Mater Trans 2016;57:1433–9.

[348] Kikuchi S, Imai T, Kubozono H, Nakai Y, Ota M, Ueno A, et al. Effect of harmonic structure design with bimodal grain size distribution on near-threshold fatigue crack propagation in Ti-6Al-4V alloy. Int J Fatigue 2016;92:616–22.

[349] Ota M, Sawai K, Nanya D, Ameyama K. Evolution of Harmonic Structure in Two Phase Stainless Steel by Mechanical Milling Process. J Jpn Inst Metals and Materi 2016;80:379–85.

[350] Rai PK, Shekhar S, Nakatani M, Ota M, Vajpai SK, Ameyama K, et al. Effect of Harmonic Microstructure on the Corrosion Behavior of SUS304L Austenitic Stainless Steel. Metall Mater Trans A. 2016;47a:6259-69.

[351] Sadat T, Dirras G, Tingaud D, Ota M, Chauveau T, Faurie D, et al. Bulk Ni-W alloys with a composite-like microstructure processed by spark plasma sintering: Microstructure and mechanical properties. Mater Des 2016;89:1181–90.

[352] Vajpai SK, Sawangrat C, Yamaguchi O, Ciuca OP, Ameyama K. Effect of bimodal harmonic structure design on the deformation behaviour and mechanical properties of Co-Cr-Mo alloy. Mater Sci Eng C 2016;58:1008–15.

[353] Vajpai SK, Yu H, Ota M, Watanabe I, Dirras G, Ameyama K. Three-Dimensionally Gradient and Periodic Harmonic Structure for High Performance Advanced Structural Materials. Mater Trans 2016;57:1424–32.

[354] Zheng RX, Zhang Z, Nakatani M, Ota M, Chen X, Ma CL, et al. Enhanced ductility in harmonic structure designed SUS316L produced by high energy ball milling and hot isostatic sintering. Mater Sci Eng A 2016;674:212–20.

[355] Tasan CC, Diehl M, Yan D, Bechtold M, Roters F, Schemmann L, et al. An Overview of Dual-Phase Steels: Advances in Microstructure-Oriented Processing and Micromechanically Guided Design. Annual Rev Mater Res 2015;45:391–431.

[356] Yoon JI, Jung J, Lee HH, Kim JY, Kim HS. Relationships Between Stretch-Flangeability and Microstructure-Mechanical Properties in Ultra-High-Strength Dual-Phase Steels. Met Mater Int 2019;25:1161–9.

[357] Tests Confirm Formability of Dual-Phase, High-Strength Steel Sheet. Automot Eng. 1978;86:50-5.

[358] Shen HP, Lei TC, Liu JZ. Microscopic Deformation-Behavior of Martensitic Ferritic Dual-Phase Steels. Mater Sci Tech-Lond 1986;2:28–33.

[359] Peranio N, Li YJ, Roters F, Raabe D. Microstructure and texture evolution in dual-phase steels: Competition between recovery, recrystallization, and phase transformation. Mater Sci Eng A 2010;527:4161–8.

[360] Calcagnotto M, Ponge D, Raabe D. On the Effect of Manganese on Grain Size Stability and Hardenability in Ultrafine-Grained Ferrite/Martensite Dual-Phase Steels. Metall Trans A 2012;43A:37–46.

[361] Calcagnotto M, Ponge D, Raabe D. Microstructure Control during Fabrication of Ultrafine Grained Dual-phase Steel: Characterization and Effect of Intercritical Annealing Parameters. ISIJ Int 2012;52:874–83.

[362] Moat RJ, Zhang SY, Kelleher J, Mark AF, Mori T, Withers PJ. Work hardening induced by martensite during transformation-induced plasticity in plain carbon steel. Acta Mater 2012;60:6931–9.

[363] Li Y, Song RB, Jiang L, Zhao ZY. Deformation response of 1200 MPa grade martensite-ferrite dual-phase steel under high strain rates. Mater Sci Eng A 2019; 750:40–4.

[364] Liu XL, Xue QQ, Wang W, Zhou LL, Jiang P, Ma HS, et al. Back-stress-induced strengthening and strain hardening in dual-phase steel. Materialia 2019;7: 100376.

[365] Park JM, Moon J, Bae JW, Kim DH, Jo YH, Lee S, et al. Role of BCC phase on tensile behavior of dual-phase Al0.5CoCrFeMnNi high-entropy alloy at cryogenic temperature. Mater Sci Eng A 2019;746:443–7.

[366] Jin X, Liang YX, Zhang L, Bi J, Zhou Y, Li BS. Back stress strengthening dual-phase AlCoCr2FeNi2 high entropy alloy with outstanding tensile properties. Mater Sci Eng A 2019;745:137–43.

[367] Mazinani M, Poole WJ. Effect of Martensite Plasticity on the Deformation Behavior of a Low-Carbon Dual-Phase Steel. Metall Mater Trans A 2007;38A:328–39.

[368] Bag A, Ray KK, Dwarakadasa ES. Influence of Martensite Content and Morphology on Tensile and Impact Properties of High-Martensite Dual-Phase Steels. Metall Mater Trans A 1999;30A:1193–202.

[369] Bittence JC. Dual-Phase Steels Promise Higher Strength Plus Formability. Mater Eng 1978;87:39–42.

[370] Colla V, De Sanctis M, Dimatteo A, Lovicu G, Solina A, Valentini R. Strain Hardening Behavior of Dual-Phase Steels. Metall Mater Trans A 2009;40A:2557–67.

[371] Gao B, Lai QQ, Cao Y, Hu R, Xiao LR, Pan ZY, et al. Ultrastrong low-carbon nanosteel produced by heterostructure and interstitial mediated warm rolling. Sci Adv 2020;6.

[372] Zhang XY. Heterostructures: new opportunities for functional materials. Mater Res Lett 2020;8:49–59.

[373] Huang GW, Li XH, Lou L, Hua YX, Zhu GJ, Li M, et al. Engineering bulk, layered, multicomponent nanostructures with high energy density. Small 2018;14: 1800619.

[374] Li XH, Lou L, Song WP, Huang GW, Hou FC, Zhang Q, et al. Novel bimorphological anisotropic bulk nanocomposite materials with high energy products. Adv Mater 2017;29:1606430.

[375] Li XH, Lou L, Song WP, Zhang Q, Huang GW, Hua YX, et al. Controllably manipulating three-dimensional hybrid nanostructures for bulk nanocomposites with large energy products. Nano Lett 2017;17:2985–93.

[376] Biswas K, He JQ, Blum ID, Wu CI, Hogan TP, Seidman DN, et al. High-performance bulk thermoelectrics with all-scale hierarchical architectures. Nature 2012; 489:414–8.

[377] Li F, Lin DB, Chen ZB, Cheng ZX, Wang JL, Li CC, et al. Ultrahigh piezoelectricity in ferroelectric ceramics by design. Nature Mater 2018;17:349–54.

[378] Ming Y, Zhang XY, Liu JP. Fabrication of bulk nanostructured permanent magnets with high energy density: challenges and approaches. Nanoscale 2017;9: 3674–97.

[379] Huang GW, Li XH, Lou L, Hua YX, Zhu GJ, Li M, et al. Engineering Bulk, Layered, Multicomponent Nanostructures with High Energy Density. Small 2018;14.

[380] Li HL, Li XH, Guo DF, Lou L, Li W, Zhang XY. Three-dimensional self-assembly of core/shell-like nanostructures for high-performance nanocomposite permanent magnets. Nano Lett 2016;16:5631–8.

[381] Lou L, Li YQ, Li XH, Li HL, Li W, Hua YX, et al. Directional Magnetization Reversal Enables Ultrahigh Energy Density in Gradient Nanostructures. Adv Mater 2021;33.

[382] Gerold V, Karnthaler HP. On the origin of planar slip in f.c.c alloys. Acta Metall 1989;37:2177–83.

[383] Steffens T, Schwink C, Korner A, Karnthaler HP. Transmission electron microscopy study of the stacking-fault energy and dislocation structure in CuMn alloys. Phil Mag A. 187;56:161-73.

[384] Hong SI, Laird C. Mechanisms of Slip Mode Modification in Fcc Solid-Solutions. Acta Metall Mater 1990;38:1581–94.

[385] Huang JY, Zhu YT, Jiang H, Lowe TC. Microstructures and dislocation configurations in nanostructured Cu processed by repetitive corrugation and straightening. Acta Mater 2001;49:1497–505.

[386] Bay B, Hansen N, Hughes DA, Kuhlmannwilsdorf D. Overview No-96 - Evolution of Fcc Deformation Structures in Polyslip. Acta Metall Mater 1992;40:205–19.

[387] Zhang Y, Zuo TT, Tang Z, Gao MC, Dahmen KA, Liaw PK, et al. Microstructures and properties of high-entropy alloys. Prog Mater Sci 2014;61:1–93.

[388] Gludovatz B, Hohenwarter A, Catoor D, Chang EH, George EP, Ritchie RO. A fracture-resistant high-entropy alloy for cryogenic applications. Science 2014;345: 1153–8.

[389] Yang T, Zhao YL, T'ong Y, Jiao ZB, Wei J, Cai JX, et al. Multicomponent intermetallic nanoparticles and superb mechanical behavior of complex alloys. Science 2018;362:933–7.

[390] Chen XF, Wang Q, Cheng ZY, Zhu ML, Zhou H, Jiang P, et al. Direct observation of chemical short-range order in a medium-entropy alloy. Nature. 2021;592: 712-+.

[391] Britton TB, Wilkinson AJ. Stress fields and geometrically necessary dislocation density distributions near the head of a blocked slip band. Acta Mater 2012;60: 5773–82.

[392] Humphreys FJ, Hatherly M. Recrystallization and Related Annealing Phenomena. Kidlington: Elsevier Science Ltd; 1995.

[393] Huang CX. Private commmunication. 2019.

[394] Death Vo. https://wwwideatovaluecom/inno/nickskillicorn/2021/05/the-innovation-valley-of-death/.

[395] Shi PJ, Zhong Y, Li Y, Ren WL, Zheng TX, Shen Z, et al. Multistage work hardening assisted by multi-type twinning in ultrafine-grained heterostructural eutectic high-entropy alloys. Mater Today 2020;41:62–71.

[396] Tsuji N, Ogata S, Inui H, Tanaka I, Kishida K, Gao S, et al. Strategy for managing both high strength and large ductility in structural materials-sequential nucleation of different deformation modes based on a concept of plaston. Scr Mater 2020;181:35–42.

[397] Wu XL, Zhu YT. Gradient and lamellar heterostructures for superior mechanical properties. Mrs Bull 2021;46:244–9.

[398] Yan FK, Liu GZ, Tao NR, Lu K. Strength and ductility of 316L austenitic stainless steel strengthened by nano-scale twin bundles. Acta Mater 2012;60:1059–71.

[399] Tellkamp VL, Melmed A, Lavernia EJ. Metall MaterTrans A 2001;32:2335.